Physik-Department E21
der Technischen Universität München

Limited view angle tomography for single material objects in non-destructive testing with X-rays

Sven Krimmel

Vollständiger Abdruck der von der Fakultät für Physik der Technischen Universität München zur Erlangung des akademischen Grades eines

Doktors der Naturwissenschaften (Dr. rer. nat.)

genehmigten Dissertation.

Vorsitzender:	Univ.-Prof. Dr. R. Netz
Prüfer der Dissertation:	
	1. Univ.-Prof. Dr. P. Böni
	2. Univ.-Prof. Dr. O. Zimmer

Die Dissertation wurde am 07.06.2006 bei der Technischen Universität München eingereicht und durch die Fakultät für Physik am 12.12.2006 angenommen.

Abbreviations

01	Single material prior knowledge
2PSL	2 pixel slit experiment
β	Rotation angle for CT or skipped angular range for partial circular scan
$\beta_{\max}$	Angular range for scanning
λ	Relaxation parameter
Θ	Tilt angle of rays in cone beam CT or tomosynthesis
BHF	Beam hardening filter
BP	Bat Phantom
CT	Computed tomography
CT PS 9	Siemens Corporate Technology, Division Power and Sensor Solutions 9
d^0_{eukl}	Normalized euklidean distance of reconstructed and original image
d_{Max}	Maximum material thickness which can be inspected
DR	Dynamic range
DT	Discrete Tomography
E	X-ray energy
$E_{\max}$	Maximum energy in polychromatic X-ray spectrum
EMPA	Eidgenössische Materialprüfungs- und Forschungsanstalt in Switzerland
FBP	Filtered back projection reconstruction
FDK	FBP algorithm by Feldkamp, Davis and Kress for 3D cone beam CT
FPI	Flat Panel Image detector
ML-TR	Maximum likelihood reconstruction for transmission tomography
N_D	Number of detector pixels
NDT	Non-destructive testing
N_P	Number of projections
N_{up}	Number of projections per image update
$N_x \times N_y$	Size of reconstructed image
PV	Peel volume as prior knowledge

Continued on next page...

SART	Simultaneous algebraic reconstruction technique
SDD	Source detector distance
SM	Smoothness of object as prior knowledge
SOD	Source object distance
TUM	Technische Universität München
WDS	Weighted distance scheme for resorting of projections
Δx	Nominal pixel resolution at object position
Δx_{D}	Detector pixel size

Contents

1 Introduction

In the life cycle of an industrial product non-destructive testing (NDT) is required to examine prototypes, to control the quality in the production line and to analyze failure of used components. Typical tasks are the detection of defects like cracks or voids and the verification of dimensional specifications. While the surface of an object is accessible for optical inspection we need other methods to look inside. Established industrial techniques rely on ultrasound, heat (thermography) and X-rays. Concerning X-ray radiography with high spatial resolution the state of the art are inspection systems using micro-focus X-ray tubes and flat panel image (FPI) detectors. They are widely used for testing of small mechanical or electronic components. By cone beam projections a high magnification is achieved and the spatial resolution can be as small as 1 μm. In order to obtain full volumetric information we use computed tomography (CT) where a number of projection images are acquired from different view angles and then reconstructed with an appropriate algorithm. Most popular is the approximative algorithm by Feldkamp, Davis and Kress (FDK), which requires projections from a 360° scan. It is a 3D extension of 2D filtered back projection (FBP) and allows a very fast computer implementation.

At Siemens CT PS 9[1] we operate such a CT system and the possibility to zoom into samples attracts a lot of attention. However, 3D micro-focus CT is only suitable for selected inspection tasks. A key problem is the strong absorption of X-rays in metal parts and this usually limits the maximum object size to a few centimeter at a typical tube voltage of 200 kV. In this work we consider the case that the extension of the object is too large and the X-ray signal not detectable from some directions such that the available information is not sufficient for standard reconstruction algorithms. A similar situation is given if the X-ray penetration is possible but the geometric access restricted. In general we speak of limited view angle tomography and the central problem is to look for a suitable reconstruction method which can handle the lack of data. Simulated projection data was essential for our analysis and finally the major challenge was to realize an experiment.

[1]This term stands for Siemens Corporate Technology, Division Power and Sensor Systems 9, and must not be confused with the single term CT which stands for Computed Tomography.

2 Theory

Motivation

Aiming at the reconstruction of limited view angle data we anticipate that there is some information missing which normally would be essential for an exact reconstruction of the object. We point out that this circumstance is independant of a specific reconstruction algorithm and merely related to the sampling process. We will start our discussion with the physical data acquisition and then use mathematical models to understand which configuration is necessary to obtain complete information and how limited view angles result in a lack of data. For a compensation prior knowledge of the object has to be used and for this purpose we have to consider iterative reconstruction algorithms.

2.1 Data acquisition for computed tomography (CT)

2.1.1 Principal configuration for CT in non-destructive testing

For computed tomography (CT) we have to collect projections of an object from different view angles. The recorded data is called sinogram. In non-destructive testing (NDT) the object itself is rotated, e.g. by 360°, which is shown in the representative set-up in Fig. 2.1 a). The object can be additionally moved along the three coordinate axes in the space between the source and the detector. For now we can assume a point source which projects the object to the detector with a magnification given by the ratio of the source detector distance (SDD) to the source object distance (SOD)

$$M = \frac{\mathrm{SDD}}{\mathrm{SOD}} \,. \tag{2.1}$$

As a starting point we can distinguish two basic cases of practical relevance. The first one is what we directly see in the schematic, i.e. 2D fan beam CT with a linear detector. In order to obtain the full 3D information of the object it has to be scanned slice by slice by shifting it along the z-direction. If the rotation and z-movement are continuous we speak of Spiral CT, which is common in medical applications [Kal00]. The other case is

3D cone beam CT using a planar detector. Looking at the schematic we can think of an extension of the beam and the detector to the z-direction. The resulting 3D projection geometry is shown in Fig. 2.1 b). It has the advantages of an isotropic magnification and allows faster scanning of a 3D object.

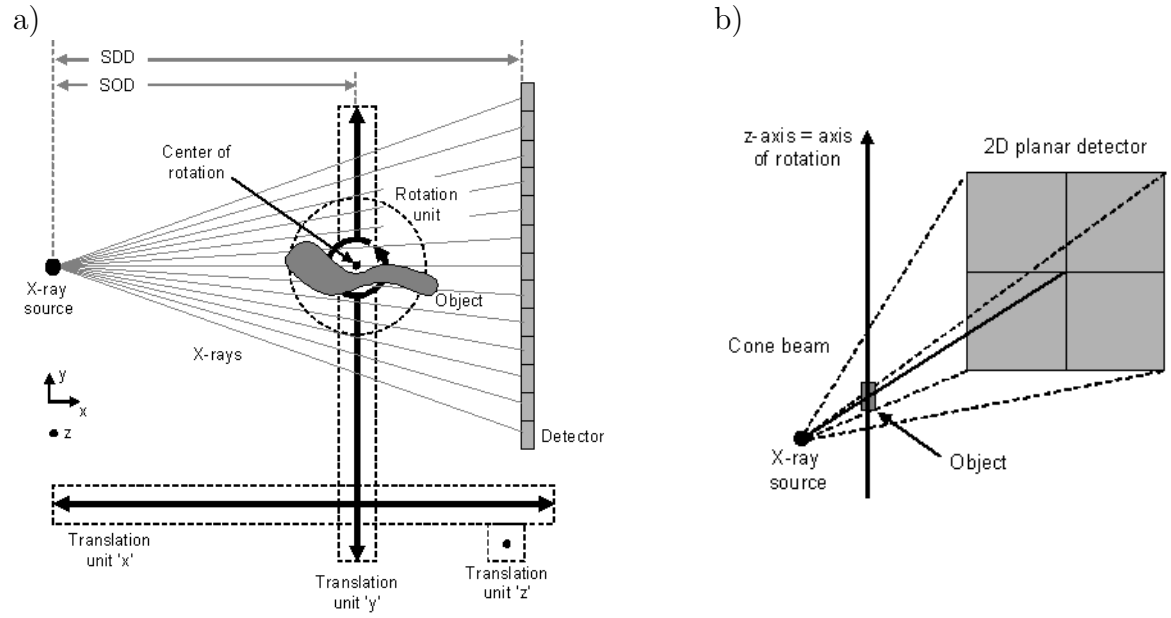

Figure 2.1: *a)* Representative set-up for X-ray CT. *b)* 3D cone beam CT.

The pixel resolution Δx at the object position follows from the detector pixel size Δx_{D} and the magnification

$$\Delta x = \frac{\Delta x_{\mathrm{D}}}{M} \; . \tag{2.2}$$

It is the nominal pixel resolution which can be achieved in a reconstructed cross-section. In practice the resolution can be reduced due to the finite size of the source. If the source spot has a diameter $\varnothing_S$ then all object points are projected to spots of diameter $\varnothing'_S$ at the detector

$$\varnothing'_S \approx \varnothing_S \, (M-1) \; . \tag{2.3}$$

Strictly this equation is exact only for object points within the yz-plane (review Fig. 2.1). For small objects we can ignore this detail and assume that the ideal projection image of the object (projection with point source) is smeared out by the projected source spot (of diameter $\varnothing'_S$). Formally this can be described by a convolution of the ideal projection image with a so called point spread function (PSF) [BS81a]. The maximum useful

magnification is given when the diameter of the source image is equal to the detector pixel size. This defines a limit for the spatial resolution. If the source spot is larger than the detector pixel size we should choose a magnification close to one and the best pixel resolution is given directly by the detector pixel size. The opposite case is a source spot which is very small compared to the detector pixel size. Then a magnification $M >> 1$ is possible and the achievable pixel resolution is equal to the source spot diameter.

2.1.2 Physical background

The measuring process in X-ray imaging relies on the attenuation of the intensity along the rays which intersect the object. It is also possible to use other types of radiation like gamma rays and neutrons. Gamma rays and X-rays are physically of the same nature as visible light (photons) and generated or detected in processes related to the coulomb interaction. X-rays are emitted from X-ray tubes, linear accelerators (LINAC) or synchrotrons and gamma rays emerge from radioacitve nuclei like Co-60. Typical energies are given in Tab. 2.1. The energy spectra are characteristic for each case, e.g. a radionuclide like Co-60 has a monochromatic spectrum while X-ray tubes have a polychromatic spectrum. Neutrons are of a different nature. They are nuclear particles and interact only with other nucleons via the strong interaction. Due to this reason they can be used to obtain a different type of contrast, for more details about imaging with neutrons see [Sil99].

Source	X-ray tubes	Synchrotron	Co-60	LINAC
Typ. Energy	<450 keV	<100 keV	1.3 MeV	10 MeV

Table 2.1: Typical energies of selected X-ray sources in NDT.

In the following we will focus on X-ray tubes because they are favorable for the installation into industrial inspection systems. In an X-ray tube electrons are accelerated by a high voltage and then slowed down in a target by interaction with the coulomb field of the atoms. The result is Bremsstrahlung with a continuous spectrum. Additional atomic transitions give rise to narrow peaks which are characteristic for the target element, e.g. tungsten. An example for a tungsten spectrum is given in Fig. 2.2 a). The maximum energy $E_{\max}$ is directly related to the acceleration voltage U by $E_{\max} = Ue$, where e is the electron charge [Mor95]. Most of the incident electron energy is converted to heat and the tube current has to be limited to avoid a melting of the target. Two types of tubes are commonly used for NDT. Micro-focus tubes have a focal spot size in the micrometer range but allow only small currents. Higher currents are possible with mini-focus tubes where the focal spot is much larger and the target is either fixed or can be rotated to give a better heat flow. Typical voltages are 225 kV for a micro-focus tube and 450 kV for a mini-focus tube.

a) b)

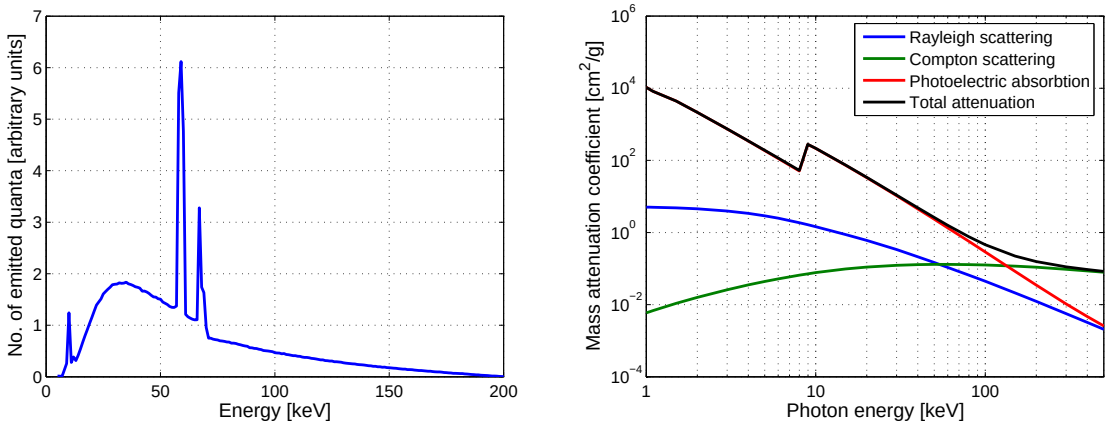

Figure 2.2: *a)* Tungsten spectra at 200 kV [Ank00]. *b)* Energy dependence of mass attenuation coefficient for copper and contribution of different interaction processes [NIST99].

The attenuation of X-rays is described by an exponential law, which is valid for monochromatic X-rays of a defined energy E. The intensity $I(d)$ after passing a homogeneous material of thickness d is given by

$$I(d) = I_0 \exp\Big(-\mu(E)\, d \Big) \,, \tag{2.4}$$

where I_0 is the intensity of the direct beam, i.e. the intensity without attenuation. The energy and material dependence is included in the linear attenuation coefficient $\mu(E)$. In databases we frequently find the mass attenuation coefficient $\mu_\rho(E)$ which is proportional: $\mu(E) = \rho\ \mu_\rho(E)$, where ρ is the material density. It is plotted for copper in Fig. 2.2 b) and we see that the absorption is much stronger for small energies. In general the object has an inhomogeneous material distribution and the exponent of the absorption law has to be replaced by a line integral along the considered ray

$$I_{\text{ray}} = I_0 \exp\left(-\int_{ray} \mu(x,y,z,E)\ ds \right) . \tag{2.5}$$

The line integral is the relevant quantity e.g. for filtered back projection reconstruction and can be obtained from the measured data by computing the logarithmic attenuation

$$L = \ln\left(I_0 / I_{\text{ray}} \right) \ . \tag{2.6}$$

This is only valid for monochromatic X-rays. In the polychromatic case Eqn. 2.5 has to be additionally integrated over the spectrum and an analytical inversion is no longer

possible. Nevertheless, the logarithmic attenuation is usually taken as an approximation and we will see later that this causes artifacts in the reconstructed images.

Coming back to the physical interaction we notice in Fig. 2.2 b) that below 1 MeV three interaction processes contribute to the total attenuation, i.e. photoelectric absorption, Compton scattering and Rayleigh scattering [BS81a]. The desired process is the photoelectric absorption where all energy of an X-ray quantum is transferred to an electron which is knocked out of an inner shell of an atom. The electron is thereafter stopped in the material and its kinetic energy is converted to heat. For Compton scattering the energy is partly transferred to an outer shell electron (inelastic scattering) and the X-ray quantum changes its direction. In the case of Rayleigh scattering no energy is transferred (elastic scattering). The attenuation law given above assumes that scattered X-rays are not detected but in practice they will contribute to an unwanted background signal. We can read from the diagram that the photoeffect is dominant for small energies while Compton scattering is getting more and more important for higher energies. This is not only true for the specific example of copper but similar for all elements. Scattering is a fundamental problem for technical X-ray CT.

The detection of X-rays relies on the same effects. In an X-ray detector the deposited energy is mostly not converted to heat but either to an electrical signal (direct conversion) or to optical light (indirect conversion). Most common is the latter case where a scintillator crystal (e.g. CsI, Gd_2O_2S, $CdWO_4$) is used for the conversion to light and combined with an optical detector, e.g. with a photomultiplier, photodiode, film, X-ray image amplifier or CCD camera. Most sophisticated are Flat Panel Image detectors where a thin film 2D array of aSi photodiodes is used to detect the light from the conversion layer. The decline of the detector signal after turning the incident beam off is called detector lag or afterglow. A small time constant is desired for CT but in practice it can be quite large for Flat Panel Image detectors where charges can be trapped in defects of the scintillator crystal as well as inside the aSi photodiodes.

2.1.3 Beam hardening filter and beam hardening correction

In combination with an X-ray tube we typically use a beam hardening filter (BHF). Such a filter is a thin metal plate which is placed into the beam to increase the mean energy of the spectrum. The effect is shown in Fig. 2.3 a). Due to the characteristics of X-ray absorption the lower energies are suppressed, the mean energy increases (which explains the term beam hardening) and the width of spectrum becomes narrower while at the same time the integral intensity decreases. The plots were computed from an unfiltered 200 kV spectrum [Ank00] and tabulated values for the mass attenuation coefficients [NIST99]. The numeric values for the mean energy and the integral intensity are given in Tab. 2.2. In practice the reduction of the intensity has to be compensated by a higher tube current or a longer integration time. A beam hardening filter of 20 mm copper would require an

increase of the current × time product by a factor of 1000 which is not feasible. Typical copper filter sizes range from 0.5 to 5 mm.

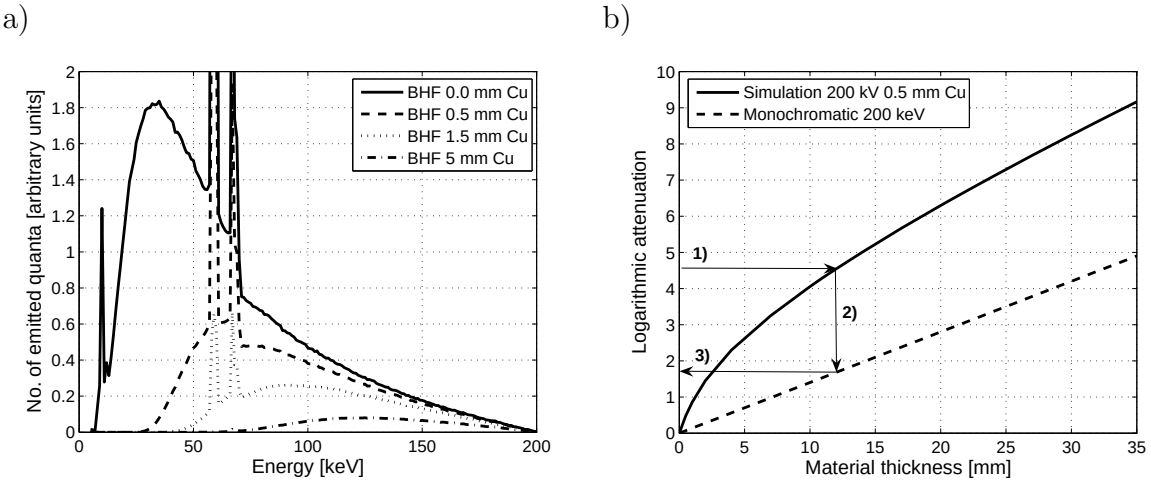

Figure 2.3: Simulations at 200 kV: *a)* Effect of copper beam hardening filter (BHF) on the spectrum. *b)* Logarithmic attenuation in copper and principle of beam hardening correction.

The distortion which is caused by polychromatic X-rays in context with CT can be seen in Fig. 2.3 b) where we plotted the logarithmic attenuation (review Eqn. 2.6) in copper versus the material thickness. In the monochromatic case (200 keV) we have a linear function which expresses the fact that the line integrals for CT reconstruction can be directly obtained from the logarithmic attenuation. However, if we use the logarithmic attenuation to estimate the line integrals in the polychromatic case, they will deviate systematically from the correct monochromatic values. In our example (200 kV with 0.5 mm Cu beam hardening filter) the value for the line integral would be too large (denoted by 1) compared to the correct monochromatic value (denoted by 3). For a single material object a simple correction is possible by linearization [Her79]. This technique requires a calibration curve to map the measured CT projection data to the correct values (denoted by 2). In practice the calibration curve has to be determined by an independant measurement. Typically a step wedge is used to obtain a small number of points which have to be fitted with a suitable function. In this work we will use simulated attenuation data to compute the required functions like we did for the plot. A correction for polychromatic X-rays is commonly refered to as beam hardening correction. This explains from the circumstance that the mean energy of a polychromatic beam increases if it passes through an object. The effect of the correction is to remove this 'hardening' of the beam which is responsible for the non-linear deviations. If a correction is not applicable a thicker beam hardening filter will lower the deviations.

d [mm]	0	0.5	1.5	3	5	10	20
$\bar{E}$ [keV]	61.9	87.5	105	120	131	144	157
$1/I$	1	2.3	5.3	12	26	110	1000

Table 2.2: Table of values for the mean energy $\bar{E}$ and the integral intensity I (normalized) at different copper beam hardening filter thicknesses d (tube voltage fixed at 200 kV).

2.1.4 Dynamic range and maximum object size

The dynamic range (DR) of the acquisition system is the relevant quantity which determines the maximum material thickness which can be inspected. The nominal dynamic range is given by the analogue digital converter (ADC) of the read out electronics of the detector. For a n bit ADC we obtain a grey level (GL) range of $1 \dots 2^n$. In reality the dynamic range will be much smaller and we can define it simply by the ratio of the maximum and the minimum detectable signal, measured in grey level

$$\mathrm{DR} = \frac{\mathrm{MaxGL}}{\mathrm{MinGL}} \, . \tag{2.7}$$

For the specification of the dynamic range we can also refer to an effective number of bits

$$\mathrm{DR} = 2^{n_{\mathrm{eff}}} \qquad \text{or} \qquad n_{\mathrm{eff}} = \log_2(\mathrm{DR}) \, . \tag{2.8}$$

For monochromatic X-rays this number is actually proportional to the maximum material thickness d_{Max}

$$d_{\mathrm{Max}} = \frac{\ln 2}{\mu(E)} \, n_{\mathrm{eff}} \, , \tag{2.9}$$

where the material and energy dependence is included in the linear attenuation coefficient $\mu(E)$. This equation is derived directly from the exponential attenuation law in Eqn. 2.4 by setting $\mathrm{MaxGL} = I_0$ and $\mathrm{MinGL} = I(d_{\mathrm{Max}})$. This is specifically related to CT experiments where the intensity of the direct beam I_0 has to be within the dynamic range because the material thickness at the edge of an object ranges down to zero and this has to be detected properly. We see here that the possible material thickness increases linearly with the number of bits. From the properties of μ it follows that for a fixed dynamic range and a given material, the thickness can be further enlarged if the energy is raised and that it will be larger for lighter materials.

For polychromatic X-rays, d_{Max} cannot be analytically computed but the dependencies are qualitatively the same as for monochromatic X-rays. For a quantitative analysis we simulated the intensity decay in typical metals for a 200 kV spectrum with a 5 mm copper beam hardening filter, Fig. 2.4 a). The direct beam intensity was set to 50000 GL which is a practical value for a 16 bit detector. In a real experiment MinGL will be determinded by a background signal and typical contributions are e.g. noise or scattering. For a certain background level the maximum thickness can be read directly from the plot, e.g. for copper it is 16 mm for 1000 GL and 40 mm for 10 GL. We also see that the penetration is better for lighter materials. In the example d_{Max} is about 5 times larger for aluminum and 10 times smaller for lead compared to copper. For iron it is 25% larger.

a) b)

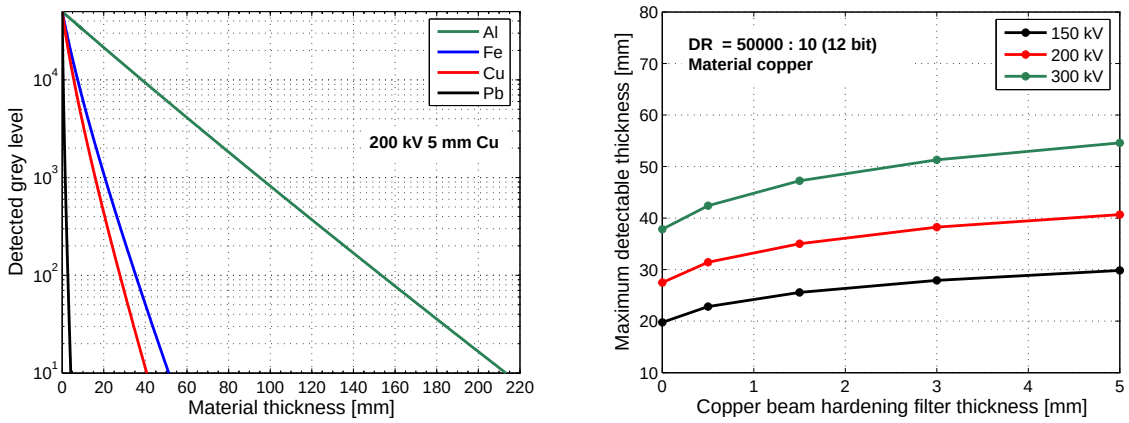

Figure 2.4: Simulation for polychromatic spectra. *a)* Intensity decay in typical metals. *b)* Maximum detectable thickness for copper at different voltages and variable copper beam hardening filter thickness.

Similar to the monochromatic case the maximum material thickness will be larger for higher energies. Looking at the energy spectrum we can either increase the maximum energy with the tube voltage or the mean energy with the beam hardening filter thickness. The result is plotted in Fig. 2.4 b) for a fixed dynamic range of 50000:10 (12 bit) and copper as material. Most important is the impact of the tube voltage but also the beam hardening filter has a significant influence.

2.2 Complete data and limited view angles

Now we will show that the sampling procedure for CT can be mapped to the Fourier space of the object and in this way we can visualize complete and incomplete data. Our presented analysis is based on the most fundamental case of CT which is parallel beam

geometry and is mathematically formulated by the Radon transform. For the mapping to the Fourier space we need the Fourier slice theorem and the sampling theorem. The underlying mathematical concept is the Fourier transform.

2.2.1 Fourier transform and sampling theorem

The Fourier transform and the sampling theorem are commonly known. Here we will only briefly review some important aspects. The Fourier transform defines the frequency decomposition of a function. For a one dimensional object function $f(x)$ we obtain the spatial frequency spectrum $F(\nu)$ by

$$F(\nu) = \int dx \exp(-2\pi i \nu x) f(x) \ . \tag{2.10}$$

Strictly $F(\nu)$ can also have a phase because it is a complex number. The amplitude is then the absolute value $|F(\nu)|$. The Fourier transform is a one-to-one relation between the object space with coordinate x and the Fourier space with coordinate ν. The inversion of the Fourier transform is

$$f(x) = \int d\nu \exp(+2\pi i \nu x) F(\nu) \ . \tag{2.11}$$

In this equation the composition of $f(x)$ as a series of the frequency basis functions $\exp(+2\pi i \nu x)$ is obvious. The extension to higher dimensions is trivial as similar integrations have to be performed in each dimension. The Fourier space is a reciprocal space which means that structures which are close to the origin in object space are far from the origin in frequency space. Basic examples are given in Fig. 2.5. The transformation of a Gaussian with standard deviation σ is a Gaussian with standard deviation $\frac{1}{\sigma}$, for a hat function of size a the resulting sinc function has its first null at $\frac{1}{a}$ and the delta function, which is most localized, gives a constant function, which is most delocalized [Jam95]. A special function is the delta comb which is an infinite sum of delta peaks which are equally spaced by Δx. The transformation gives a delta comb with reciprocal peak spacing $\frac{1}{\Delta x}$ [BS81a].

An important relation in context with Fourier transforms is the convolution theorem. A convolution is typically used to describe a filtering of a function $f(x)$ with a filter $g(x)$

$$f(x) \otimes g(x) = \int dt f(t) \cdot g(x-t) \ . \tag{2.12}$$

The convolution theorem states that a convolution in the object space is equivalent to a multiplication in the Fourier space and vice versa

$$\mathrm{FT}(f \otimes g) = \mathrm{FT}(f) \cdot \mathrm{FT}(g)) \ , \tag{2.13}$$

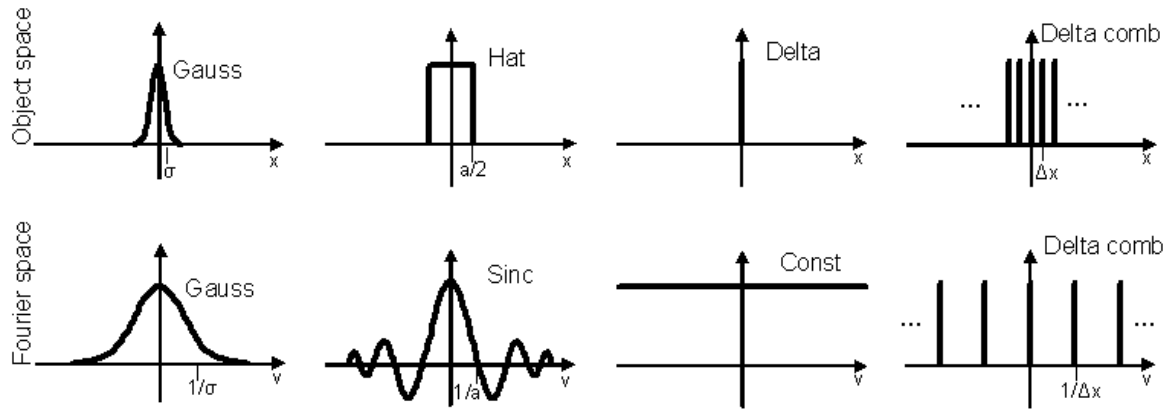

Figure 2.5: Examples for 1D Fourier transforms of typical functions. The original functions are shown above and their Fourier transforms below.

where FT is the Fourier transform. All properties which were discussed here are also valid for a discrete formulation of the Fourier transform (DFT), i.e. if the integrals are replaced by sums. The DFT has some additional properties like e.g. periodicity which we do not discuss here [KS87].

The sampling theorem formulates a limitation for the discrete sampling of a continuous function $f(x)$. The exact reconstruction of the original function is only possible if it is bandlimited, i.e. the maximum object frequency is smaller than the Nyquist frequency. If the sampled points are spaced by Δx the Nyquist frequency is [Jaeh93]

$$\nu_N = \frac{1}{2\Delta x} \,, \tag{2.14}$$

which is half of the sampling frequency $\frac{1}{\Delta x}$. If this condition is violated higher and lower frequency components overlap, which is called aliasing. The situation is illustrated in Fig. 2.6. We can describe the sampling by a multiplication of the object function with a delta comb of peak spacing Δx. In the Fourier space this is a convolution of the object spectrum with a delta comb of peak spacing $\frac{1}{\Delta x}$, i.e. the spectrum is reproduced periodically by the sampling frequency. As the object is defined by a real function the amplitude spectrum is symmetric, which explains the factor 2 in the Nyquist condition above. If the object spectrum exceeds the Nyquist frequency the reproduced spectra overlap and aliasing occurs.

2.2.2 Radon transform and Fourier slice theorem

The most fundamental case of CT is given for 2D parallel beam geometry and the Radon Transform [Rad17] is the mathematical formulation of the corresponding data

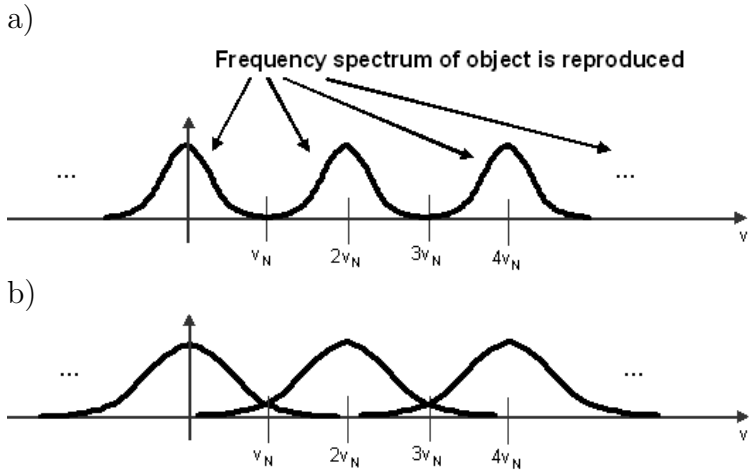

Figure 2.6: Illustration of Nyquist theorem in Fourier space: *a)* If the maximum object frequency is $\leq \nu_N$ then the reproduced spectra are separated and the object can be recovered exactly. *b)* If the maximum object frequency is $> \nu_N$ then the reproduced spectra overlap, which is called aliasing.

acquisition. The configuration is shown in the left part of Fig. 2.7. An object which is defined by a function $f(x, y)$ is projected by parallel rays to a line which represents the detector. We define the orientation of this line by the rotation angle β of the rays relative to the x-axis in the drawing plane and the condition that the detector is perpendicular to the rays. The position on the detection line is described by the coordinate t. Each pair (β, t) defines a specific projection ray which can be parameterized by a function $\text{ray}_{\beta,t}(s)$. The corresponding projection $P(\beta, t)$ is computed by the line integral along this ray [KS87]

$$P(\beta, t) = \int_{-\infty}^{\infty} f\Big(\text{ray}_{\beta,t}(s)\Big)\, ds\ . \tag{2.15}$$

With the Radon transform we have a continuous description of the projection process. Via the 2D Fourier slice theorem (also known as central slice theorem) this process can be mapped to Fourier space [KS87], [BS81b].

> **2D Fourier slice theorem:** The 1D Fourier transform of a projection line gives the values on a line of equal orientation (rotation angle β) through the origin in the 2D Fourier space of the object, see Fig. 2.7.

This theorem is valid independently of a certain reconstruction algorithm. For an extension to 3D parallel beam geometry we consider a projection to a plane instead of a line. In the figure for 2D we have to add a third axis which is perpendicular to the drawing

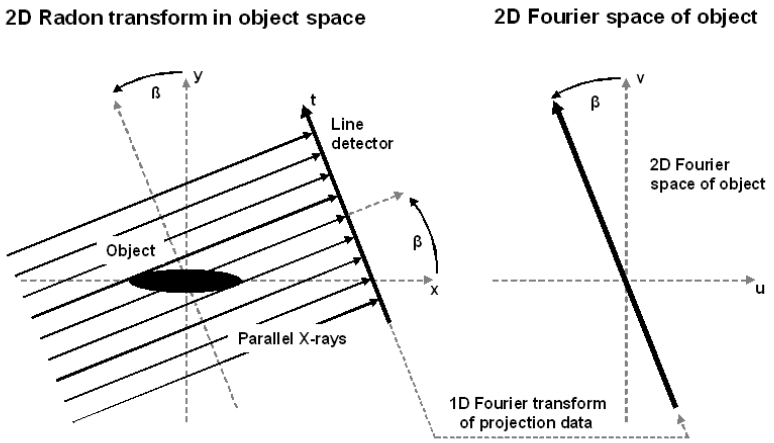

Figure 2.7: Radon transform and illustration of 2D Fourier slice theorem.

plane. The beam of rays and the detector are extended alike. An additional degree of freedom is available now. Beside the rotation of the rays by β within the drawing plane they can be also tilted by an inclination angle Θ relatively to it. For the 3D Fourier slice theorem we have to exchange the rotating line in the 2D theorem by an accordant plane.

> **3D Fourier slice theorem:** The 2D Fourier transform of a projection plane gives the values on a plane of equal orientation (rotation angle β and inclination angle Θ) through the origin in the 3D Fourier space of the object.

The definition of the inclination angle Θ will become clearer in the next two subsections.

2.2.3 Complete sampling in CT

If we look at the 2D Radon transform the complete data of the object is recorded if all points in its Fourier space are collected. This is achieved for a continuous 180° rotation of the line which was considered in the Fourier slice theorem before. However, in an experiment we can only sample discrete sets. First of all the detector is not continuous and the projections which are given by the Radon transform have to be sampled by discrete pixels. The sampling theorem tells us the maximum object frequency which can be recorded or in other words that the pixel spacing has to be small enough to detect some given object features. This is common sense. In order to understand how many projections are necessary we depict the sampling in the 2D Fourier space as it is shown in Fig. 2.8.

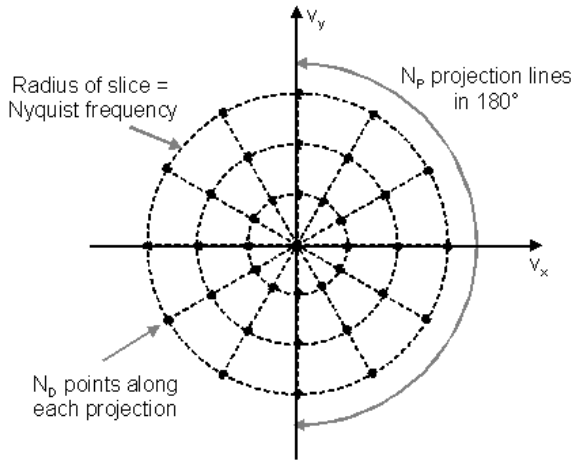

Figure 2.8: Illustration of the sampling in the 2D Fourier space.

It is natural to spread a certain number of $\mathrm{N_P}$ projections equally over the angular range of 180°. The projections correspond to lines in the Fourier space which are given by the Fourier slice theorem. For a finite number of $\mathrm{N_D}$ detector pixels the values on each line are known at $\mathrm{N_D}$ points which is indicated by the black dots in the figure. By the sampling theorem the radius of the slice in the figure is equal to the Nyquist frequency $\nu_N = 1/2\Delta x_\mathrm{D}$ where Δx_D is the detector pixel spacing. Now we can ask for the minimum number of projections to exploit the resolution which is given in radial direction, i.e. the resolution which is obtained by the one dimensional sampling with the detector. This is achieved if the coverage of the Fourier space in angular direction is not worse than it is in radial direction, i.e. the distance of the points on the circumference of the slice should be less or equal to the spacing in radial direction

$$\nu_N \frac{\pi}{\mathrm{N_P}} \leq \frac{2\nu_N}{\mathrm{N_D}} \tag{2.16}$$

and the result for the minimum number of required projections is [Eps03]

$$\mathrm{N_P} = \frac{\pi}{2}\mathrm{N_D}\ . \tag{2.17}$$

In fact this statement is independent of a specific reconstruction algorithm. The extension to 3D parallel beam geometry is trivial if we consider a circular rotation and inclination angle $\Theta = 0$. Then the 3D space can be divided into horizontal slices for each of which the 2D case is valid. A different situation is given if the beam is not parallel. For 2D fan beam geometry (Fig. 2.9 a) we can adopt qualitatively what has been deduced for the 2D parallel beam case. Actually this is plausible because one case can be mapped to the other. The projection rays which are acquired in a fan beam CT

can be resorted directly to parallel rays if the source rotates on a full 360° circle. In this way we obtain a 360° parallel beam CT and all rays are scanned twice. In fact it is sufficient to scan only a range 180° + fan angle [KS87]. We should mention that for theoretical considerations we think of a rotation of the source and the detector instead of the object. For 2D fan beam CT this is a circular source trajectory.

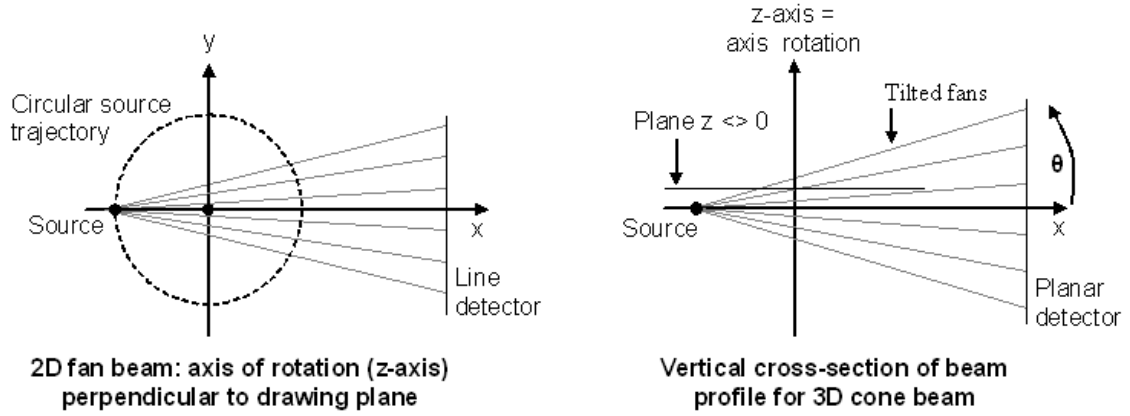

Figure 2.9: *a)* Scanning geometry for 2D fan beam CT and *b)* Extension to 3D cone beam CT.

The extension of a fan beam to a cone beam is shown in Fig. 2.9 b). We can think of a series of fan beams which are tilted out of the 2D plane and the linear detector is exchanged by a planar one. The inclination angle between a tilted fan and the x-axis is denoted by Θ. In the central plane which is defined by $z = 0$ we have the fan beam situation where the axis of rotation is perpendicular to the projection rays and $\Theta = 0$. The other horizontal planes with $z \neq 0$ are intersected by tilted fans for which $\Theta \neq 0$. Due to this reason a circular source trajectory is not sufficient for complete sampling. The generalized theorem which defines the condition for complete sampling in 3D cone beam CT is the Tuy-Smith sufficiency condition [Tuy83]. It states that exact reconstruction is possible if all planes which intersect the object also intersect the source trajectory at least once. An example for a source trajectory which fulfills this condition is a helix.

2.2.4 Sampling with limited view angles

In order to depict how limited view angles cause a lack of data we look again at parallel beam geometry for which the situation becomes visible if we apply the Fourier slice theorem. We can distinguish two fundamental cases where limited view angles occur. One is a 2D partial circular scan and the other is 3D tomosynthesis. The first case is

shown in Fig. 2.10 a). Here we consider the 2D Radon transform but the rotation of the source is not completed leaving out an angular range of 2β in 180°. In the 2D Fourier space this is equivalent to a rotating line leaving out a double wedge with opening angle equal to 2β (Fig. 2.10 b). For an extension to the third dimension the line detector can be replaced by a plane which is perpendicular to the xy-plane. The double wedge of missing points will be extended alike with translational symmetry.

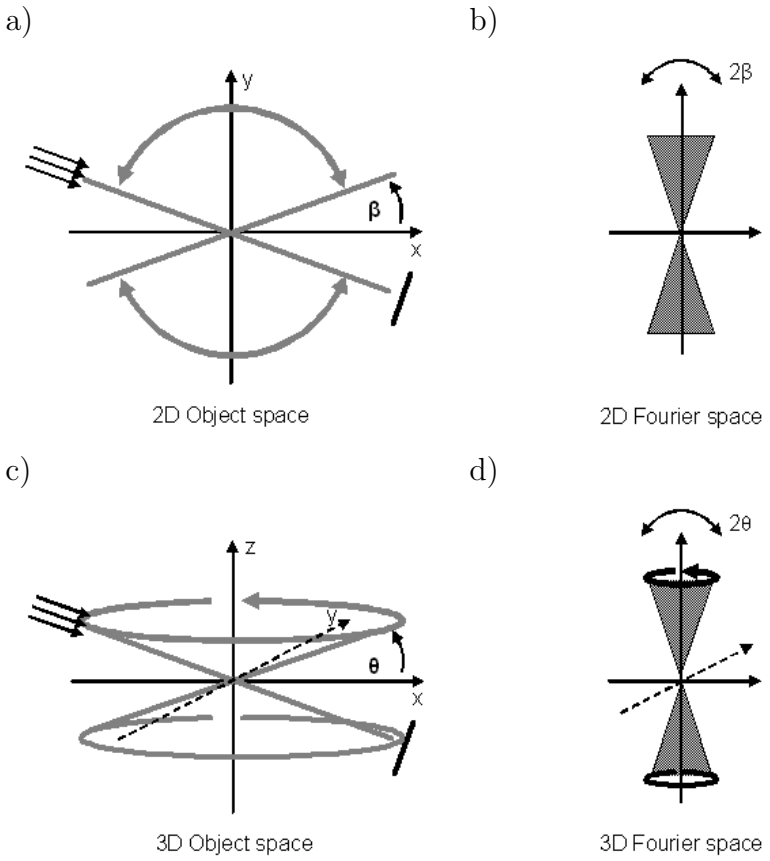

Figure 2.10: Two fundamental cases for limited view angle tomography: *a)* 2D partial circular scan results in *b)* missing double wedge in Fourier space. *c)* 3D tomosynthesis ($\Theta \neq 0$) results in *d)* missing double cone.

We have another situation if we consider an inclination angle Θ between the beam and the xy-plane. For 3D parallel beam tomosynthesis [Hae99] we assume a full 360° rotation but an inclination angle $\Theta \neq 0$. Fig. 2.10 c) shows that the circular source trajectory is above the xy-plane and that the detector follows the source movement at the opposite side. The rotating plane which is defined by the 3D Fourier slice theorem omits a double cone in Fourier space and in analogy to the partial scan the opening angle is equal to

2Θ (Fig. 2.10 d). In both cases the missing points in Fourier space are equivalent to missing information of the object. This is evident because the Fourier transform is a one-to-one relation which connects both spaces. If we compare a 3D partial circular scan to tomosynthesis for $\beta = \Theta$ the lack of data will be larger in the first case due to the fact that the missing wedge will have a larger volume than the missing cone.

In X-ray CT we further have to consider 2D fan beam geometry or 3D cone beam geometry which were discussed before in Fig. 2.9. The partial circular scan can be applied directly to a fan beam if we extend the source trajectory symmetrically to 360°. leaving out an angular range of 4β, review Fig. 2.10 a). It is plausible that a lack of data will occur similarly as for the parallel case. In NDT this configuration can appear if the geometric acces of an object is limited, e.g. an oblong object which is placed very close to an X-ray tube cannot be completely rotated. An equivalent situation is given if the object can be fully rotated but the X-ray penetration is limited from some directions. In general the view angles for which the X-rays are not detectable must not be in a connected angular range, i.e. arbitrary view angles can be missing.

For cone beam CT we have a particular case. We mentioned before that a circular source trajectory is not sufficient because of the inclination of the rays relative to the xy-plane (angle Θ), review Fig. 2.9 b). From a qualitative point of view this is comparable to 3D parallel beam tomosynthesis where we have a fixed inclination angle $\Theta > 0$ (review Fig. 2.10 c) and it is obvious that a lack of data will occur. Beyond this we could also use the tomosynthesis configuration itself together with the cone beam, i.e. let the point source travel on a circle above the xy-plane.

2.3 Reconstruction algorithms for complete sampling

The most common reconstruction algorithm is filtered back projection (FBP) [KS87], which is fast, has a high image quality and is robust against experimental distortions. FBP is derived using continuous Fourier theory and can be considered as the direct inversion of the sampling process. In contrast to FBP the simultaneous algebraic reconstruction technique (SART) [AK84] solves a finite equation system. It is a classical representative for iterative reconstruction. A more special iterative algorithm is maximum likelihood reconstruction for transmission tomography (ML-TR) [Nuy97]. It is a statistical method and originates from emission tomography where the reconstruction of very noisy data is required. The main benefit of iterative algorithms is that prior knowledge of the object can be included, which will be discussed in the next section. For the iterative algorithms we will restrict our analysis to 2D problems but in principal an extension to 3D is possible as well. A practical aspect for the reconstruction of X-ray projections is that all considered algorithms rely on monochromatic data. The distortions which are caused by polychromatic X-rays will be discussed later (chapter 3).

2.3.1 Filtered back projection (FBP)

Filtered back projection algorithms are known for various scanning geometries and it is impossible to give a complete overview here. The most important aspect for this work is that it is a one way process. It directly inverts the sampling process and limited view angles will result in image artifacts. The simplest form of FBP is given for 2D parallel beam geometry. From a mathematical point of view this is the analytical inversion of the Radon transform, which was derived in [Rad17].

A good presentation of the solution is given in [KS87] and can be scetched as follows. The 2D object is defined by a continuous function $f(x, y)$. With the Radon transform (review Fig. 2.7) an infinite number of parallel projections $P(\beta, t)$ are collected in the angular range of 180° degree. As discussed in the previous section the Fourier slice theorem maps the detected values to radial lines in the 2D Fourier space of the object. In fact the values in the Fourier space are then known in polar coordinates. A transformation to cartesian coordinates is performed and a 2D inverse Fourier transform returns the original function $f(x, y)$ exactly. This is evident because all relations are one-to-one.

The resulting inversion formula is

$$f(x,y) = \int_0^\pi Q\Big(t(x,y,\beta),\beta\Big)\, d\beta \tag{2.18}$$

$$Q(t,\beta) = P(t,\beta) \otimes_t h(t)\ . \tag{2.19}$$

Q is the filtered projection, i.e. for fixed β the projection $P(t, \beta)$ is filtered in the t coordinate with a filter h(t). This is discribed by a 1D convolution, which is indicated by the symbol $\otimes_t$. The filter function which follows from the mathematical derivation is called ramp filter (not shown here). Finally the object $f(x, y)$ is obtained by smearing back the filtered projections along the same rays which were used for the projection itself. This can be seen if we look at a given image point (x, y). The ray which travels through this point under a given projection angle β hits the detector at a unique position which can be described by a function $t(x, y, \beta)$ and the corresponding value of the filtered projection is added to the image.

For the practical application it is necessary to transfer the continuous solution to a discrete version, i.e. replace the integrals by sums. We do not show this explicitly here. Regarding the natural beam geometry for X-ray tubes we further have to consider a point source instead of a parallel beam. The solution for 2D fan beam geometry is still straight forward because the fan beam projections can be resorted to parallel projections if a full 360° (or at least 180°+fan angle) turn is performed. In the analytical derivation this is expressed by a coordinate transformation resulting into additional weighting factors in the reconstruction formula [KS87]. These factors can be further extended to the third dimension which leads to the approximative algorithm by Feldkamp, Davis and

Kress (FDK) [FDK84] for 3D cone beam CT. It still relies on a circular source trajectory and from the previous section we know that the sampling of the object is not sufficient in this case. The advantage is that a fast computer implementation is possible. Compared to this an exact solution for a helical source trajectory is much more complex [Kat03].

2.3.2 Simultaneous algebraic reconstruction technique (SART)

The simultaneneous algebraic reconstruction technique was first introduced by [AK84] and is a modification of the algebraic reconstruction technique [Gor70]. We got inspired by the more recent work of K. Müller [Mue98] where a high performing SART solution for 3D cone beam CT is presented. For our investigations we implemented a 2D version of SART and we will focus on this case here.

Projection equation

In contrast to the continuous formulation of the data acquisition with the Radon transform we directly look at the sampled data for SART. A discrete 2D grid defines the image and the pixels are referenced by a single index, e.g. j. The total number of pixels is N and the pixel values are combined to the vector $\mathbf{v} = (v_j)_1^N$. The projection data is defined analogously by $\mathbf{p} = (p_i)_1^M$ where the values p_i are the measured line integrals and the index i runs through all projection rays, i.e. all detector pixels and all projection angles. Notice that the p_i must not be confused with the measured intensities, i.e. for monochromatic X-rays the relation between line integrals and intensities is given by the logarithmic attenuation in Eqn. 2.6. We can now describe the data acquisition by a linear equation system

$$\mathbf{p} = \mathrm{H}\mathbf{v} \,, \tag{2.20}$$

which is called projection equation and H is the projection matrix. The formulation of this equation is not restricted to a specific geometric configuration and now we do not explicitly define the position of the image pixels, the arrangement of the detector pixels and the distribution of the projection angles. All this information is included in the matrix H. Its coefficients h_{ij} are weight factors which describe the contribution of the image pixels to the projection rays, i.e. for a certain projection ray i the contribution of an image pixel j to the line integral p_i is given by h_{ij}. This is visualized in Fig. 2.11 a) for a single projection ray. The relevant image pixels which have non-zero weights are shown shaded. In fact the complete measuring process is hidden behind H. Clearly H can only include a model for the real processes and we refer to H$\mathbf{v}$ as the forward projection of a given image $\mathbf{v}$. A key problem is the definition of an appropriate model (projection model) for the computation of H. We will look at this detail later and continue with the structure of the algorithm first.

a) b)

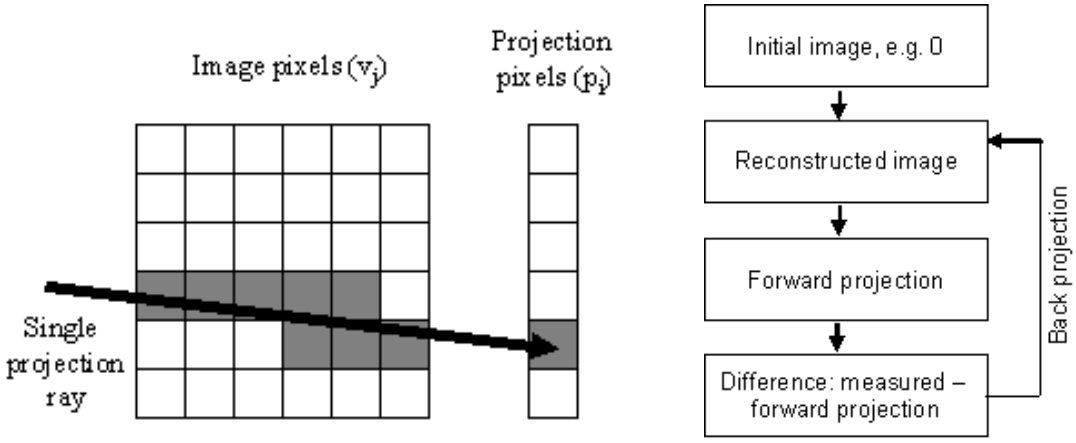

Figure 2.11: *a)* Visualizing the projection equation. *b)* Work flow for iterative solution.

Iterative solution

The reconstruction problem is here to solve the projection equation from above. As H is very large it cannot be inverted and a simple formulation by $\mathbf{v} = \mathrm{H}^{-1}\mathbf{p}$ is not possible. Instead an iterative optimization process is used which is scetched in Fig. 2.11 b). Starting with an initial guess of the result (usually zero) the image $\mathbf{v}$ will be modified to match the forward projection $\mathrm{H}\mathbf{v}$ to the measured projection data $\mathbf{p}$. The modification step is implemented by a back projection of the difference $\mathbf{p} - \mathrm{H}\mathbf{v}$ and the back projection itself is defined by the transposed matrix H^T.

This leads to the basic image update formula

$$v_j = v_j + \lambda \cdot \frac{\sum_{i \in P_m} \frac{\overbrace{\overbrace{p_i - \overbrace{\sum_k h_{ik} v_k}^{\text{Forward}}}^{\text{Difference}}}^{\text{Backward}}}{\sum_k h_{ik}} \cdot h_{ij}}{\sum_{i \in P_m} h_{ij}} \,. \tag{2.21}$$

The parameter λ is called relaxation parameter and controls the reconstruction speed and stability. The equation is normalized correctly by the sums in the denominators and $\lambda = 1$ would be the choice for ideal projection data. With P_m we denote the set of

projection rays which are included into the update step. For SART these are all rays which belong to one projection angle β_m and m is the integer index for the enumeration of the available projection angles. We have to distinguish between iterations and update steps. Within one iteration the update step is repeated for all angles.

Image update options

Considering the selection of the pojection angles we can generalize the SART approach and include more than one angle into one update step. If N_{up} angles are combined then P_m will contain all rays which which belong to these angles:

$$P_m = \{\text{All rays which belong to } N_{up} \text{ projection angles}\} . \tag{2.22}$$

In this case the index m enumerates different sets of each N_{up} projection angles. For $N_{up} = 1$ we obtain the SART solution and if the total number of projection angles is N_P then $N_{up} = N_P$ means that all available projection rays are included. Remark: For ART only single rays are used in one update step and the term simultaneous ART explains from the fact that more than one ray is used.

Another important update option for SART is the arrangement of the projection angles. In the measurement the projections are usually recorded sequentially and in order to improve the convergence we should resort them before starting the reconstruction. The angular distance of consequent projections should be as large as possible. Most effective is the weighted distance scheme (WDS) which is described in [Mue98]: If a certain number of projections has already been chosen before then the next projection is chosen such that:

1. The angular distance to the other projections is maximal.
2. The standard deviation of these distances is minimal.

The second condition ensures that the projections are evenly distributed. For the computation of the conditions the projections are additionally weighted, i.e. those which were selected more recently are given more weight.

Projection model

A central problem in recent research is the projection model which describes how the weights for the projection matrix are computed. Considering the discrete sets of image pixels v_j and projection rays p_i an interpolation will be necessary to adapt to the physical acquisition process. There are two possible ways to look at this problem. One is the

voxel driven projection model with interpolation on the detector and the other is called ray driven with interpolation in the reconstructed image.

The term voxel driven comes from 3D CT and refers to volume pixel. Transferred to the 2D problem voxel driven means that we consider a physical projection ray which starts from a certain image grid point j and travels under a given angle to the detector (Fig. 2.12 a). If the angle is selected from the discrete set of available angles it is unlikely that this ray hits exactly the center of a detector pixel. The contribution to a neighboring pixel i is usually computed by linear interpolation giving the weight

$$h_{ij} = 1 - \frac{d_{ij}}{\Delta x} \,, \tag{2.23}$$

where Δx is the detector pixel spacing and d_{ij} is the distance of the detector pixel i and the intersection point of the considered ray with the detector. This interpolation scheme is actually the same as it is used for FBP reconstruction.

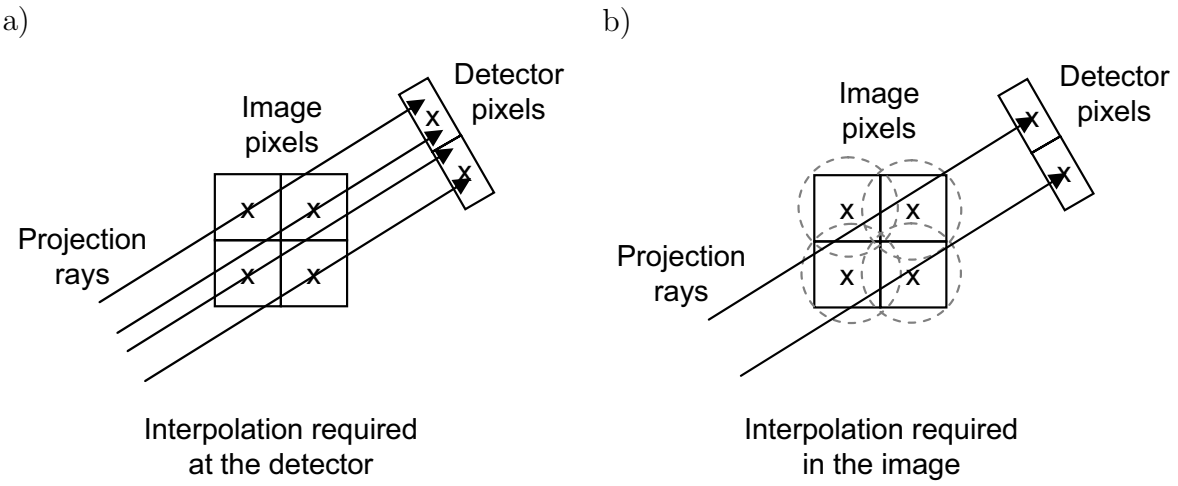

Figure 2.12: *a)* Voxel driven projection model and *b)* Ray driven projection model.

In direct opposition to the voxel driven model the ray driven projection model assumes that the physical rays start at the center of the detector pixels and travel through the image grid (Fig. 2.12 b). Obviously such a ray will not essentially hit the grid points and we need a two dimensional interpolation. Here we followed a method which has also been used in [Mue98]. A two dimensional continuous interpolation kernel (interpolation function) has to be defined and convolved with the discrete image grid, i.e. the kernel is shifted to each grid point and the result is added up. This is indicated by the dashed circles in the figure. In this way the image is transferred to a continuous function and the line integral along the ray can be computed which is quite close to the physical acquisition process.

In order to achieve a fast reconstruction the kernel should have a small spatial extent because then the number of relevant image pixels which contribute to each ray will be small. A problem coming up with interpolation is that aliasing can be introduced and amplified in the iterative process. In the ideal case the frequency spectrum of the filter should be bandlimited according to the Nyquist frequency of the grid. But then the spatial extend would be extremely large which is not feasible. In practice a compromise is necessary, i.e. a small spatial size and at the same time a small size in Fourier space. Fig. 2.13 a) shows the one dimensional profiles of typical interpolation kernels and their Fourier transforms are given in Fig. 2.13 b). The spatial position is given in units of the image grid spacing Δx and the frequency in Fourier space is normalized to the sampling frequency $\frac{1}{\Delta x}$. The worst case is the hat function which is a sinc function in Fourier space where it has an infinite extent. The performance of the bilinear interpolation is mediocre and the Bessel-Kaiser [Lew90] kernel is superior. A further improvement of the aliasing problem is reported by H. Kunze where in addition to the interpolation in the image, the projections are convolved with the filter profile [Kun05]. In our analysis we will refer to this option as Bessel-Kaiser with convolved projections or short as Bessel-Kaiser CP.

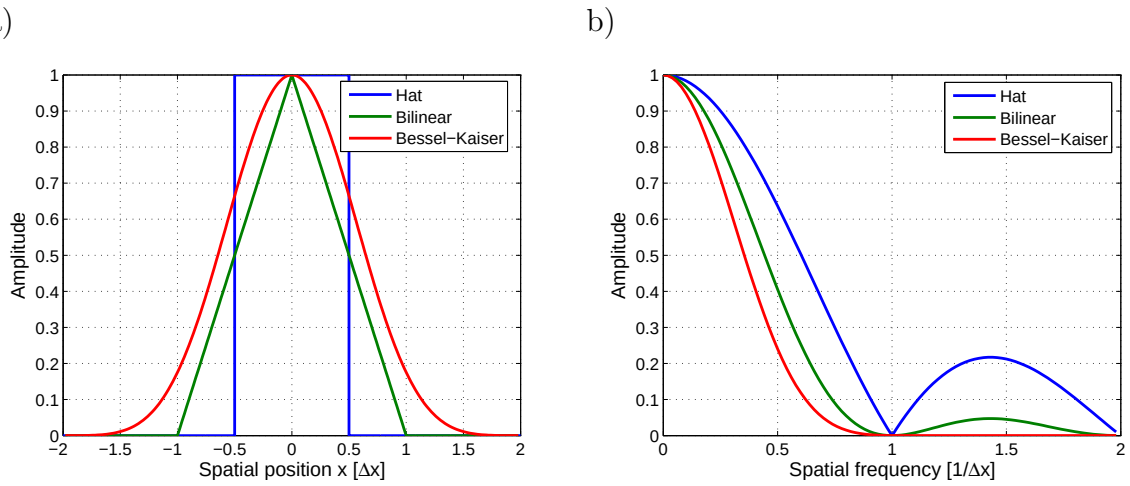

Figure 2.13: *a)* Different interpolation kernels in object space. *b)* Corresponding frequency spectra in Fourier space.

Finally we were interested to see what the ideal case would be. A possible way to do this is to generate the measured CT data with the projection model itself, i.e. define an image $\mathbf{v}_{\text{Original}}$ on the grid and obtain $\mathbf{p}$ by $\mathbf{p} = \mathrm{H}\mathbf{v}_{\text{Original}}$ and then reconstruct $\mathbf{v}$ again form $\mathbf{p}$. Clearly the projection model is ideal in this case, i.e. it is an exact model of the data acquisition process. Aliasing cannot occur because the 'needles' which sample the original image $\mathbf{v}_{\text{Original}}$ are the same as used in the reconstruction. We will refer to this option as internal projection data.

2.3.3 Maximum likelihood reconstruction (ML-TR)

For the implementation of maximum likelihood reconstruction for transmission tomography (ML-TR) which is described in [Nuy97] we used the same structure as for SART. Only a few essentials had to be changed, namely the update formula and with it the image update scheme. Further, this reconstruction directly uses intensity values instead of line integrals. The relation between the measured intensity values, denoted by q_i, and the corresponding line integrals p_i which were considered for SART is given by the exponential absorption law, i.e.

$$q_i = \exp\Big(- p_i \Big) \; . \tag{2.24}$$

Therefore the forward projection has to be extended in the same way:

$$a_i = \exp\Big(- \sum_j h_{ij} v_j \Big) \; , \tag{2.25}$$

where h_{ij} and v_j are the coefficients of the projection matrix and the image pixel values as they were defined for SART. The update formula is derived from the maximum-likelihood estimation method which is a general method to find an optimum set of parameters by taking into account the statistical nature of a measurement [Bar95]. In the case of X-ray CT these parameters are the unknown image pixel values v_j. For a given image the expected intensity of the i-th projection ray is a_i and the probability for measuring an arbitrary value x is given by the Poisson distribution

$$P(x, a_i) = \frac{a_i^x \exp(-a_i)}{x!} \; . \tag{2.26}$$

Considering a complete CT measurement $(q_i)_{i=1}^M$ the total probability for this measurement is described by the likelihood

$$L = \prod_{i=1}^{M} P(q_i, a_i) \; . \tag{2.27}$$

The task is to maximize this expression by a variation of the a_i which implies the variation of the v_j. In other words the maximum likelihood approach will find a solution for the image (with pixel values v_j) such that the given set of measured projection data $(q_i)_{i=1}^M$ has maximum probability.

This leads to the following update formula:

$$v_j = v_j + \lambda \cdot \frac{\overbrace{\sum_{i \in P_m} \overbrace{\left(\overbrace{a_i}^{\text{Forward}} - q_i \right)}^{\text{Difference}} \cdot h_{ij}}^{\text{Backward}}}{\sum_{i \in P_m} h_{ij} \cdot [\sum_k h_{ik}] \cdot a_i} \,. \tag{2.28}$$

In analogy to SART the image is forward projected and a difference is computed which is then back projected. However, the computed difference is an intensity difference. The forward projection is hidden in the term a_i which was defined above. Unlike SART the set of projection rays P_m has to include all available rays for ML-TR, i.e. all rays from all projection angles. In our implementation this corresponds to the generalized image update option $\mathrm{N_{up}} = \mathrm{N_P}$ as it was explained before in context with SART. Considering the projection model we can use the same options as for SART except for 'Bessel-Kaiser CP' because the convolving of projections is only suitable if we look at line integrals.

Beside the correct noise model the ML-TR algorithm has another important quality. If we consider an oblong object we have smaller projection values from some directions and their contribution in the update formula will be reduced compared to the other view angles. This effect is due to the summation in the numerator which is performed over all view angles and enhanced because of the fact that we look at intensity values which decay exponentially with the object size.

2.4 Limited view angle tomography

2.4.1 Including prior knowledge of the object

We have explained before how limited view angles result in missing points in Fourier space, review Fig. 2.10. In order to compensate for this we could think of associating the unknown to the known points. Looking at the projection equation system which was formulated for SART (Eqn. 2.20) this corresponds to adding appropriate equations or to reduce the complexity of the problem.

A practical way to realize this is to include prior knowledge of the object. This can be any kind information which is known before we start the reconstruction. We will see later that a very effective type is the material composition of the object. Further we consider that the object must be smooth, i.e. neighboring values in the reconstructed image should not vary abruptly except for the edges. A type of geometric information could be e.g. the exterior shape of the object.

FBP is not suitable here because it is a one way process, i.e. a direct inversion of the sampling process. Iterative algorithms are required where the prior information can be built into the feed back loop which is shown in Fig 2.14. The feedback is typically given by a forward projection (as defined for SART) which is compared to the measured data in order to verify if the actual reconstruction is good. From this a modification of the reconstructed image is computed and this is where the prior knowledge can be processed.

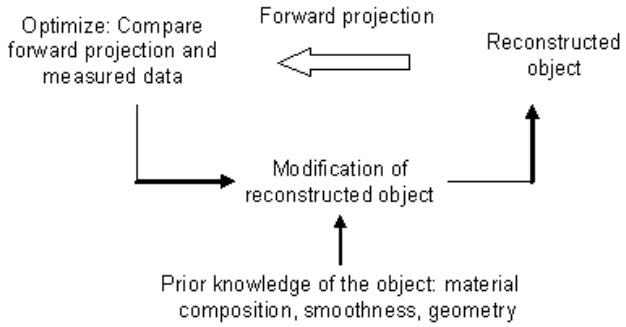

Figure 2.14: Flow chart for including prior knowledge of the object.

In the following we consider objects which only consist of one single material and we will restrict the reconstructed values to '0' for air and '1' for material. This is a special case of discrete tomography [HK99] and is opposed to the continuous scale which has been assumed so far. We will discuss possible extensions for SART and ML-TR which are semi-continuous and then look at the full binary method which is presented by A. Kuba [Kub02]. In this work we will use the term Discrete Tomography (DT) exclusively to refer to his algorithm (see also section 2.4.3).

2.4.2 SART and ML-TR with single material prior knowledge

The single material prior information can be included into SART and ML-TR by repeated segmentations. In the simplest case a fixed threshold could be used for a segmentation of the reconstructed image after each iteration. This is a quite severe impact and it is better to use a dynamic double threshold which allows a partial segmentation which is gradually transfered into a full segmentation. Fig. 2.15 shows how a lower threshold v_{lo} is increased and a higher threshold v_{hi} is decreased after each iteration. For the segmentation all values above v_{hi} are set to '1', those below v_{lo} to '0' and those in between are left unchanged. In this way the segmentation has only a very small impact at first but then as the two thresholds converge as the binarization proceeds.

Typically the pixel absorption for the material is normalized to '1' and the thresholds

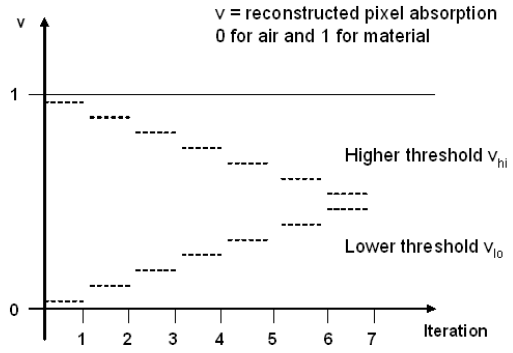

Figure 2.15: Dynamic double threshold for repeated segmentations in SART and ML-TR.

are incremented linearly and symmetrically within the interval $[0, 1]$:

$$v_{\mathrm{lo}}(n) = \frac{n}{N} \cdot \mathrm{DTH} \tag{2.29}$$

$$v_{\mathrm{hi}}(n) = 1 - v_{\mathrm{lo}}(n) \ , \tag{2.30}$$

where n is the iteration number and N the total number of iterations. The final values of the thresholds are defined by the threshold range DTH, e.g. 40% or 50%. A similar approach was used in [Bec02] for ART and introduced as binary steering in [HK99]. Less effective is an interval projection, i.e. fixed thresholds $v_{\mathrm{lo}} = 0$ and $v_{\mathrm{hi}} = 1$ which was used in [Jaen93]. Here we considered an additional option. We left the algorithm running for a certain number of iterations N1 before applying the segmentation and the threshold increment. This was then repeated N2 times giving a total number of N1xN2 iterations.

As additional information we included a Markov random field smoothness prior which was derived in [Man00] for ML-TR. In our implementation we used it in the same way for SART. The following penalty term was added to the corresponding update formulas in Eqn. 2.21 and Eqn. 2.28:

$$\sum_k w_{kj} \cdot \phi(v_k - v_j) \ , \tag{2.31}$$

where v_j and v_k denote image pixel values and where $w_{kj} = 1$ for neighboring pixels and 0 elsewhere. This term enforces that adjacent image pixels have similar values as we would expect for a smooth object. For a selected pixel j the deviations of the neighbouring pixels k are given by $v_k - v_j$. They are weighted with a linear function ϕ and then added up to give a correction for v_j in each update step. A limitation is put to the correction

by defining ϕ as

$$\phi(v) = \left\{ \begin{array}{ll} \frac{b}{a} \cdot v & \text{for } |v| \leq a \\ b & \text{for } |v| > a \end{array} \right\} . \tag{2.32}$$

The function ϕ is sketched in Fig. 2.16. We can interprete the action of the smoothness term similar to a spring force which pulls the value of the selected image pixel j into the direction of its neighbors. As neighbors we typically consider the 4 nearest neighbors but also more neighbors could be chosen. In practice the parameters a and b have to be determined by trial and error to obtain the best result.

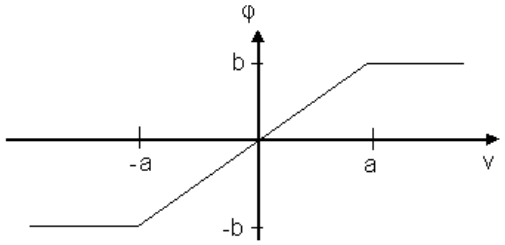

Figure 2.16: Linear weighting function with limitation for smoothness prior.

The complexity of the equation system can be further reduced if we only reconstruct the valid image pixels, i.e. all pixels outside a certain boundary can be set to zero. If the outer surface of the object is known, we can define such a peel volume [Bec02] by an envelope of the surface leaving a gap to it. This gap allows a tolerance for the reconstruction, see Fig. 2.17.

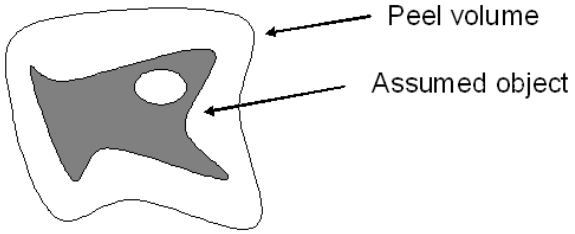

Figure 2.17: Illustratiuon of a peel volume.

2.4.3 Discrete Tomography (DT)

The Discrete Tomography (DT) approach by A. Kuba is the most consequent method to include the single material information. At no time there exist intermediate image values. For the evaluation we had a cooperation with his department at the University of Szeged, Hungary. The algorithm also uses a forward projection as it was described by the projection equation for SART (Eqn. 2.20) but it does not modify the image by a back projection. Instead it randomly changes the image pixel values and keeps a changed value if an improvement was achieved, i.e. the difference between the forward projection and the measured projection data is smaller than it was before. We will see below how this is expressed by an optimization equation which is solved by simulated annealing. The advantage of this formulation is that additional prior knowledge like smoothness can be included on a more general basis, i.e. it must not be adapted to a special update scheme as it was necessary for SART or ML-TR. More details about the algorithm were described in our joint publication [Kri05] and we quote a section of the text which was contributed by the University of Szeged.

Remark: A variation to our previous notation is used here, i.e. the letter X was used instead of $\mathbf{v}$ for the image pixel values and P instead of $\mathbf{p}$ for the projection values.

Begin quotation:

> Discrete tomography is a special kind of tomography that can be applied if the object to be reconstructed consists of a few known homogeneous materials. This information can be included into the reconstruction process giving the possibility to reconstruct such simple objects from a much smaller number of projection values than it is necessary in the case of more complex objects [Kub02].
>
> Reformulating $HX = P$ as an optimization problem we get the following objective function $C(X)$ to be minimized:
>
> $$C(X) = \|HX - P\|^2 + g \cdot F(X) \ . \tag{2.33}$$
>
> The term $g \cdot F(X)$ is an optional penalty term which can control the objective function according to additional prior knowledge about the object to be reconstructed. In our case we have used a special kind of function
>
> $$F(X) = \sum_{i=0}^{J} \sum_{l \in Q_i^m} g_l \cdot |x_i - x_l| \ , \tag{2.34}$$
>
> where Q_i^m is the set of indices of the $m \times m$ adjacent pixels of the ith lattice pixel. The g_l is the corresponding element of the $m \times m$ Gaussian scalar

matrix, that is,

$$g_l = \frac{1}{2\pi\sigma^2} e^{-(\mu^2+\nu^2)/2\sigma^2} \ , \tag{2.35}$$

where σ is the parameter of the 2D Gaussian function and (μ, ν) is the 2D coordinates of the 1D index l. The g_l scalar weights the differences according to the distance of the ith and lth lattice points. Using this regularization term we can reconstruct objects with big homogeneously connected regions.

In discrete tomography we search a binary vector X which can be calculated by a simulated annealing (SA) combinatorial optimization method. SA is a random-search technique that is based on the physical phenomenon of metal cooling. The system of metal particles gradually reaches the minimum energy level where the metal freezes into a crystalline structure. Based on previous works [KGV83], we first implemented the SA algorithm in the following way (Fig. 2.18). The algorithm starts from an arbitrary initial binary image $X^{(0)}$, an initial (high) temperature $T^{(0)}$ and calculates the objective function value $C(X)$. Then a position j is randomly chosen in the reconstructed image X. Let X' be the image that differs from X only by changing the value of X in position j to the other binary value, i.e., $x'_j = 1 - x_j$. This change is accepted by the algorithm, i.e., X is replaced by X' if $C(X') < C(X)$. Even if the objective function does not get smaller, the change is accepted with a probability depending on the difference $\Delta C = C(X') - C(X)$.

Formally, the change is accepted even in that case when

$$\exp(-\Delta C/\kappa T) > z \ , \tag{2.36}$$

where κ, T and z are, respectively, the Boltzmann constant ($11.3805 \times 10^{-23} \times m^2 kg s^{-2} K^{-1}$), current temperature, and a randomly generated number from a uniform distribution in the interval $[0, 1]$. Otherwise, the change is rejected, i.e., X does not change in this iteration step. If a change is rejected then we test the level of *efficiency* of changes in the image in the last iterations. It means that we count the number of rejections in the last N_{iter} iterations. If this number is greater than a given threshold value R_{thr} then the efficiency of changes is too low and the SA optimization algorithm will be terminated.

We calculate the variance of the cost function in the last N_{var} iterations. A so-called *equilibrium state* is said to be attained if the present estimate of the current ΔC variance is greater than the previous variance estimate. If the equilibrium state is achieved, we reduce the current temperature (allowing changes with smaller probabilities when the value of the objective function is greater) and let the algorithm run with a lower temperature value (T is replaced by $h \cdot T$, where h is the so-called *cooling factor*). In our experiments we chose the same value for the parameter as in [Pey94], namely $h = 0.9$.

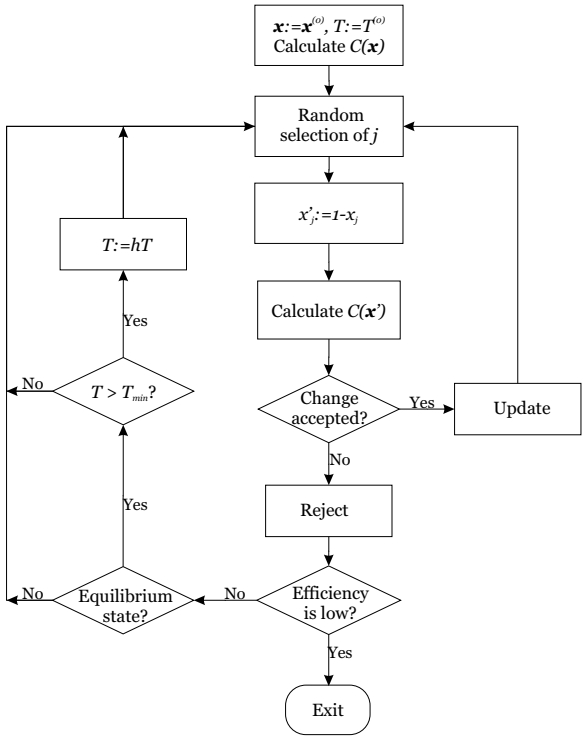

Figure 2.18: Flow-chart of the first SA algorithm.

Finally we implemented the SA as follows. We change all the X vector elements from 0 to 1 or vice-versa in one iteration step. The changes are accepted or rejected similarly like in the previous implementation. When one iteration has been done we reduce the current temperature and start a new iteration step. The algorithm stops when the ratio of the value of the current objective function and the value of the starting objective function fall below a given threshold value ($C(X')/C(X^0) < C_{thr}$) or the current temperature is less then a given temperature ($T < T_{thr}$).

End quotation.

3 Examples of applications where limited view angles occur

Motivation

In this chapter we would like to put the analysis of the limited view angle problem into a practical context. We will discuss three related examples of X-ray CT applications which are of particular interest in non-destructive testing (NDT). In each case we use filtered back projection (FBP) reconstruction and characteristic limited view angle artifacts appear. At the beginning of our work we looked at 3D micro-focus CT and investigated the standard type of FBP for this configuration, i.e. the approximative algorithm by Feldkamp, Davis and Kress (FDK), and we did not know whether the major contribution of the observed artifacts were caused by approximations within the algorithm or by limited view angles. Now we know that the latter is the case. This is obvious from our theoretical considerations in the previous chapter and we suspect that the artifacts are somehow related to the missing points in Fourier space. We will demonstrate this with the help of the discrete Fourier transform at the end of this chapter (Masking of missing points in Fourier space).

Because of the ongoing miniaturization of industrial products 3D micro-focus CT is of particular interest and our first two examples (steel cylinder and ball grid array) are related to this case. Using the steel cylinder we will discuss limited view angles in the standard configuration and for the ball grid array we consider additional geometric restrictions. Apart from this there are also other sources of artifacts in a real experiment and we present an analysis of the most important effects for the steel cylinder. Regarding a solution for limited view angle tomography, we will see in the next chapters that distortions of the data are very critical. For an extensive analysis in this work we selected a 2D problem. This is our third example (Bat Phantom) where limited view angle artifacts are caused by limited X-ray penetration.

3.1 Example 1: 3D micro-focus CT of a steel cylinder

3.1.1 Sample, set-up and classification

Fig. 3.1 a) shows a photo of the steel cylinder. It was originally designed for a joint project (ForμProd) on dimensional measuring in 3D micro-focus CT, dissertation of H. Steinbeiß [Ste05]. For this project the main experimental effort was the optimization of the measurement accuracy yielding μm spatial resolution which is of high industrial interest considering e.g. the inspection of a part of a fuel injection nozzle. Here and for the following examples we tried to classify the type of application considering different aspects:

- Sample category: Small metal components for which full X-ray penetration is possible.
- NDT task: Full 3D inspection with a very high spatial resolution down to 1 μm for dimensional measurement and defect detection.
- Feasibility: Well suited problem for 3D micro-focus CT. However, achieving μm resolution is particularly demanding regarding mechanical stability and calibrations.

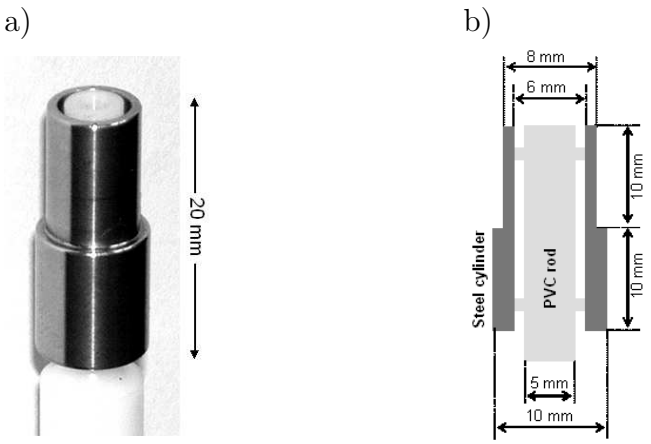

Figure 3.1: Steel cylinder fixed on PVC rod: *a*) Photo and *b*) schematic of vertical cross-section.

Looking at the cross-section of the steel cylinder (Fig. 3.1 b) we see that it is a hollow cylinder and it has a step of wall thickness between the lower and upper part. A PVC rod in the center serves as a holder and there is an air gap between the rod and the cylinder which is fixed at a few points only. Here we use the steel cylinder to point out limited

view angle artifacts which can occur in the standard configuration for 3D micro-focus CT, i.e. a circular source trajectory and FDK reconstruction. Fig. 3.1 b) shows the vertical cross-section of the selected scanning geometry. The cylinder was orientated axially with the axis of rotation and the step of wall thickness was in the central plane. In this configuration the X-ray penetration is not critical, but the half cone angle $\Theta = 8.2°$ for the projection of the object to the detector is quite large. For performing the experiment we used the set-up at Siemens CT PS 9 which is described in chapter 5.

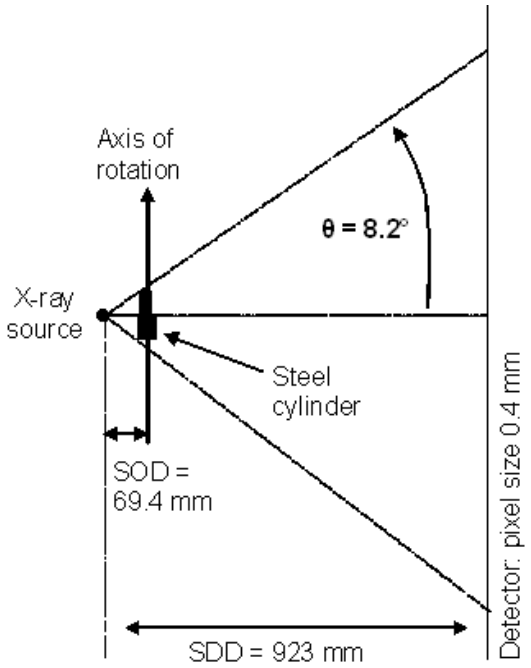

Figure 3.2: Vertical cross-section of 3D scanning geometry.

3.1.2 Artifact analysis

We will now look at the artifacts which were observed in the reconstructed cross-sections of the steel cylinder. In order to identify the artifacts we reconstructed experimental as well as simulated projection data. The advantage of simulated projection data is that the underlying parameters can be selected individually. The following results were presented in our publication [Kri04]. Three major types of artifacts can be observed in the experiment (Fig. 3.3 a). They are caused by limited view angles (denoted by LV), polychromatic X-rays (denoted by beam hardening or BH) and scattering. For our analysis we first matched the simulation (Fig. 3.3 b) to the experiment by using exactly the same geometric configuration (see set-up above), using identical beam parameters

(210 kV polychromatic spectrum, 0.5 mm copper beam hardening filter) and adding a similar amount of noise (0.5% of direct beam intensity). Scattering, however, could not be modelled with our simulation tool (see next chapter). Finally we switched to ideal monochromatic data (Fig. 3.3 c) where only limited view angle artifacts remain.

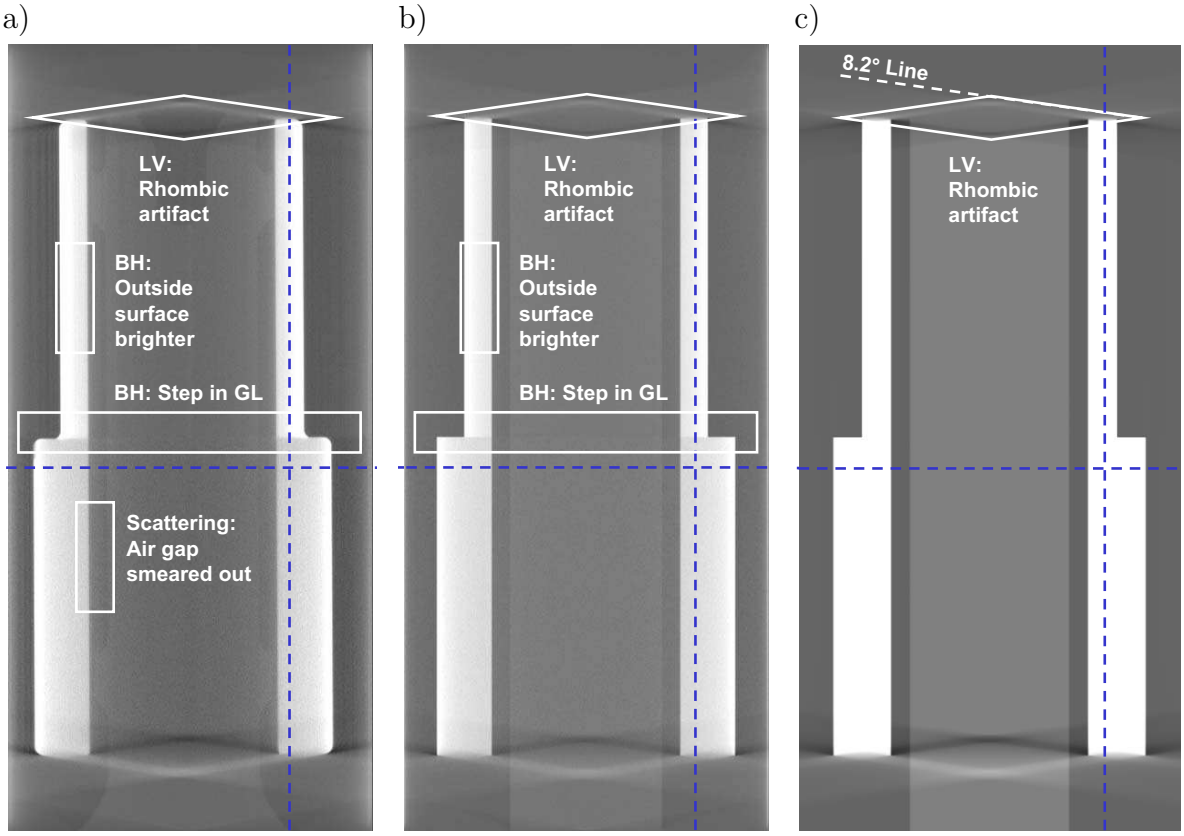

Figure 3.3: Reconstructed cross-sections of steel cylinder (FDK algorithm): *a)* Experimental result, *b)* simulation matched to experiment (except for scattering) and *c)* ideal simulation. The dashed blue lines indicate the positions where we took line profiles (see Fig. 3.4).

Due to scattering the reconstructed image of the experimental data appears more washed out and especially the contrast of the air gap is reduced compared to the matched simulation, where scattering was not included. A more precise analysis of the image distortions is possible if we look at the line profiles in Fig. 3.4, which were taken at the positions indicated by the dashed blue lines in the reconstructed cross-sections. The horizontal line profiles confirm that the air gap is hardly resolved in the experiment (Fig. 3.4 a) while it is clearly visible in the simulation (Fig. 3.4 c). Further the central region is strongly curved in the experiment.

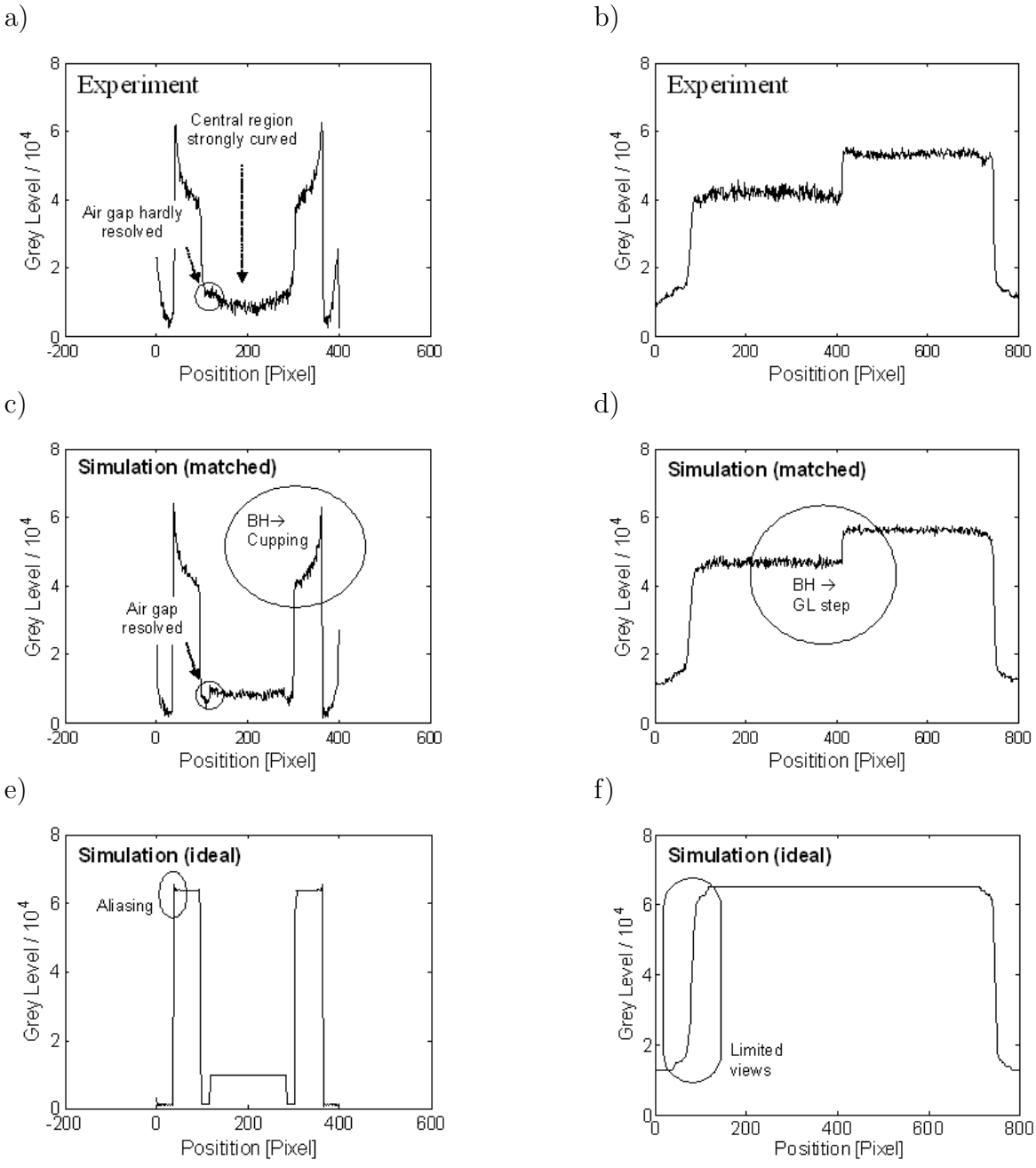

Figure 3.4: Horizontal and vertical line profiles. Experiment: *a)* horizontal and *b)* vertical; matched simulation: *c)* and *d)*; ideal simulation: *e)* and *f)*.

The effect of polychromatic X-rays was modelled correctly in the matched simulation. We observe distortions of the reconstructed grey levels to which we refer as beam hardening artifacts. There is a decline of the grey levels from the outside to the inside cylinder surface, which can be seen in the horizontal line profile (Fig. 3.4 c) and is also called cupping artifact. Further we observe a step of grey levels from the lower to the upper part of the cylinder in the vertical line profile (Fig. 3.4 d), which explains from the cupping and the different wall thicknesses in the lower and upper part of the cylinder. The deeper reason for the beam hardening artifacts is that the line integrals which are required for the reconstruction can only be approximated for polychromatic projection data by the logarithmic attenuation (review section 2.1.3). The term beam hardening reminds us to the non-liner shift of the mean energy of the spectrum to a higher value when the X-rays pass through material.

If we switch to monochromatic X-rays, the beam hardening artifacts vanish. Although the simulated data is now ideal (no distortions) we notice that rhombic shaped artifacts at the top and the bottom of the cylinder are remaining in the reconstructed cross-section (see Fig. 3.3 c). These are typical limited view angle artifacts. In this case they are caused by the sampling with the circular source trajectory and the large half cone angle $\Theta = 8.2°$. The half shape angle of the rhombus is actually roughly equal to Θ. This is indicated in the figure by the 8.2° line (this line is tilted by 8.2° relative to the horizontal orientation). We will observe similar artifacts in the other examples and we anticipate that errors which may be introduced by the FDK algorithm itself can only play a minor role. The line profiles for the ideal simulation are shown in Fig. 3.4 e) and f). In this case the limited view angle artifacts only have an impact on the vertical profile. In the horizontal profile we observe an additional effect. Due to aliasing there are small overshoots at the cylinder edge. Concerning the reconstruction the number of projections (1200) was large enough compared to the number of image pixels in horizontal direction (400), but for the simulation of the projection data the object was not bandlimited (see next chapter).

3.1.3 Potential for limited view angle tomography

Considering e.g. the dimensional measurement the discussed artifacts are not a fundamental draw back. The method which is presented in [Ste05] is quite robust against local deviations of grey levels and in addition to this a beam hardening correction can be applied for single material objects (review section 2.1.3). Of course the limited view angle artifacts are present at the top and the bottom of long objects but this does not affect the accuracy of a measurement in horizontal direction at least in the central region. Above all it is possible to avoid limited view angles by using a helical source trajectory instead of a circular one. The reconstruction of limited view angle data is therefore not essential for this application.

3.2 Example 2: 3D simulation of a ball grid array

3.2.1 Simulation model and classification

In no other field miniaturization is advancing as fast as in electronic industry. This pushes the development of assembling techniques for a high integration of components on printed circuit boards (PCBs). A typical example are ball grid arrays (BGAs) for the connection of micro-chips to PCBs. With an array of tiny solder balls below the two dimensional surface of the chip a very high number of electrical contacts can be realized. The requirements for the fabrication are extremely high and non-destructive inspection with μm resolution is very much desired. 3D micro-focus X-ray CT seems to be predestined for this task but we point out that the problem hits today's limits. A classification can be given as follows:

- Sample category: Electronic components on printed circuit boards. Complex objects with many different materials. Strong absorbing metals, e.g. lead and tin in solder balls are particularly critical for X-ray penetration.
- NDT task: 3D inspection with 1-10 μm spatial resolution for the detection of cracks and voids.
- Feasibility: The inspection with 3D micro-focus CT is today only possible for small components (typ. Ø 10-20 mm). For larger parts and especially for complete PCBs the geometric access and/ or the X-ray penetration are limited which make an X-ray inspection impossible today.

In order to show the limitations we considered a simplified model for a ball grid array, Fig. 3.5 a). An array of 3x3 copper cylinders (instead of solder balls) is mounted between two aluminum carriers (instead of the micro-chip and the PCB). Typical defects are broken joints, i.e. horizontal cracks (parallel to the PCB surface) between the balls and the carrier. They were modelled by gaps of different heights which are given in Fig. 3.5 b). The materials as well as the gap dimensions were chosen to give a much easier inspection problem than we would find it in reality. Further we did not include a real PCB environment but consider a virtual PCB which restricts the geometric access of the BGA (Fig. 3.5 c).

3.2.2 Scanning with limited geometric access

Considering the restricted access which is caused by the virtual PCB there are two consequent scanning geometries: a partial circular scan or tomosynthesis. Examining

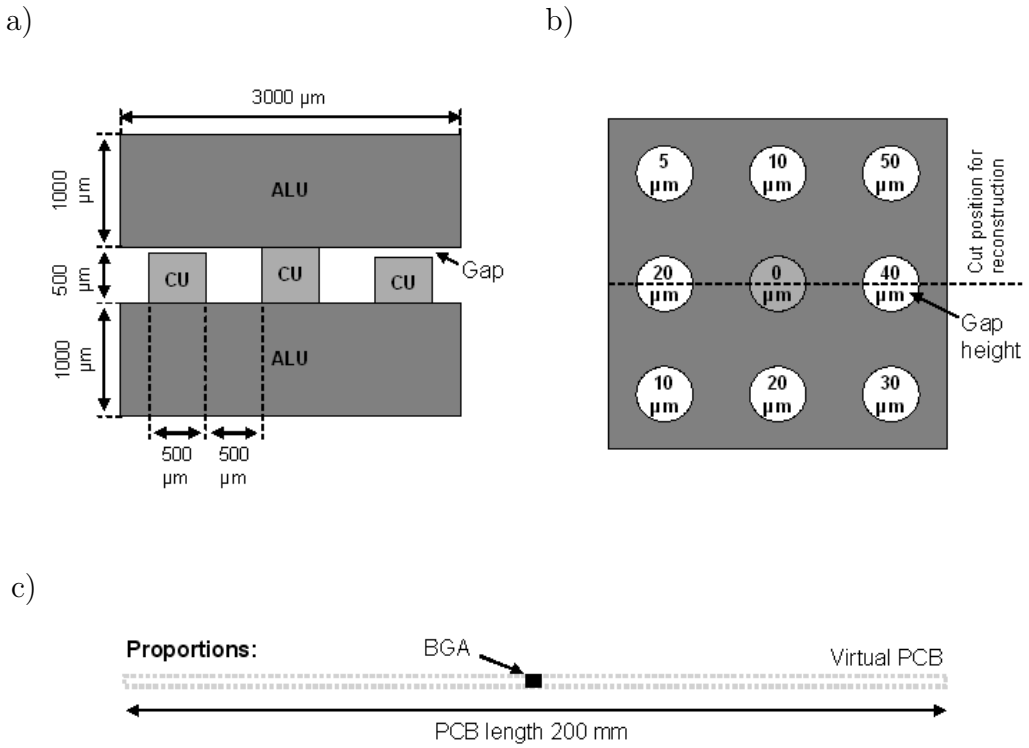

Figure 3.5: Simulation model of a ball grid array (BGA): *a)* Vertical cross-section showing the gaps between the copper cylinders and the upper aluminum carrier. *b)* Horizontal cross-section with corresponding gap heights. *c)* Proportions of the BGA model in the environment of the virtual printed circuit board (PCB).

3D micro-focus CT we simulated cone beam projection data for both cases and reconstructed them with the FDK algorithm. In order to expose only the relevant artifacts we used ideal parameters for the simulation, i.e. monochromatic energy (160 keV) and an infinite dynamic range. In this way we also excluded artifacts due to limited X-ray penetration.

Partial circular scan

For the partial circular scan the set-up was arranged as shown in Fig. 3.6 a). In order to avoid a collision of the virtual PCB with the X-ray source, the partial circular scan skips two angular sections each of 2β range, i.e. 4β in 360°. The drawing plane in this figure is equal to the central plane of the 3D cone beam configuration. It includes the source point and is perpendicular to the axis of rotation (review theory section 2.2.3). If we reconstruct this plane the result of the FDK algorithm is equal to 2D FBP and therefore

would be exact if the angular sections were not skipped. Here we chose $\beta = 20.16°$ (116 of 500 projections were skipped) and we observe huge rhombic artifacts (Fig. 3.6 b). In analogy to all other examples the half shape angle is approximately equal to β (see 20° line). This is remarkable because the value for β is quite large and we conclude that the shape of the artifact is directly related to the angular range which was skipped and obviously a contribution from the reconstruction algorithm can only be minor.

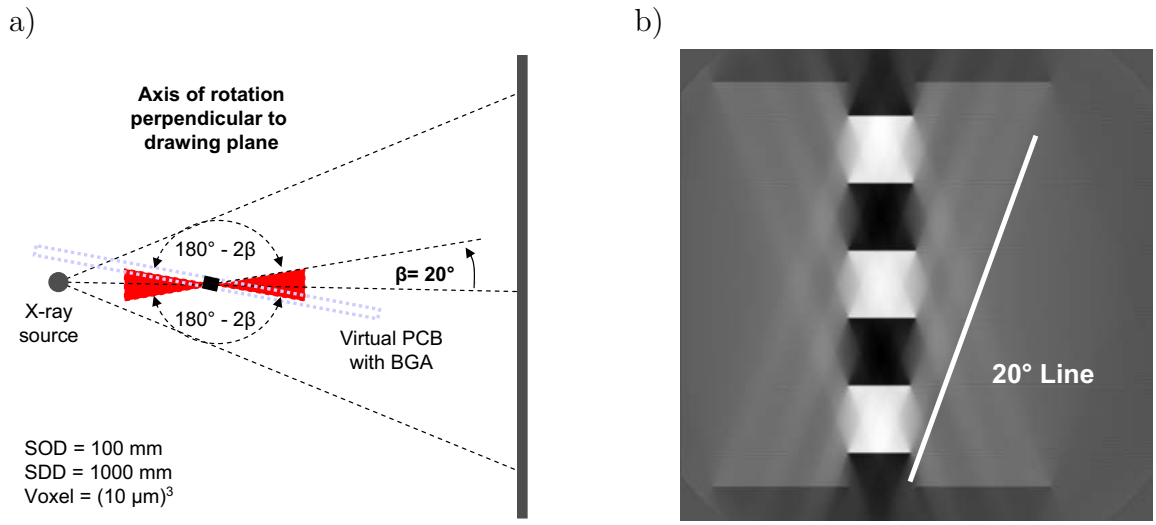

Figure 3.6: Scanning with partial circular scan. *a)* Top view of the central plane in the 3D scanning geometry. *b)* Reconstruction of central plane (FDK algorithm).

Tomosynthesis

In contrast to the partial circular scan the virtual PCB is orientated parallel to the central plane for tomosynthesis. Fig. 3.7 a) shows that the virtual PCB is actually elevated above the central plane such that it cannot hit the X-ray tube. The tomosynthesis angle Θ has the same impact as the half cone angle in the example of the steel cylinder. In Fig. 3.7 b) we see the reconstructed vertical cross-section at the position which was indicated before in Fig. 3.5 b). The gap heights from left to right were 20, 0 and 40 μm and even for small tomosynthesis angles (here $\Theta = 6°$) they are not resolvable due to limited view angle artifacts. Just as for the partial circular scan or the example of the steel cylinder these artifacts have a rhombic shape and the half shape angle is roughly equal to Θ (see 6° line). They are independent of the magnification and the pixel resolution. We chose a voxel size of 10 μm for which the gaps would be easily resolvable if no artifacts would occur. The source detector and source object distance, SDD=1000 mm and SOD=100 mm, are related to typical micro-focus CT set-ups.

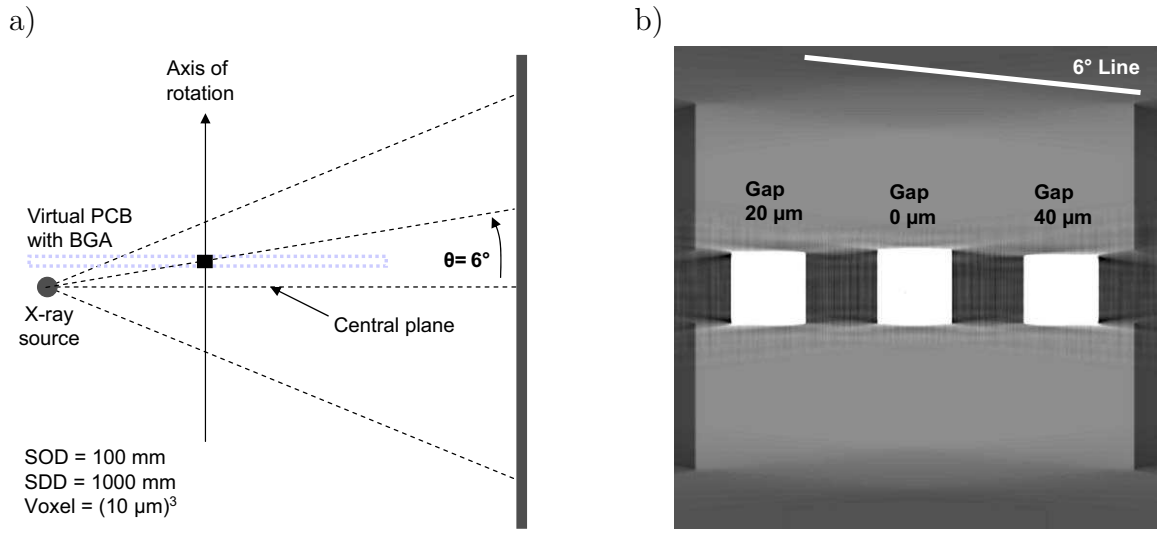

Figure 3.7: Tomosynthesis of BGA model. *a)* Vertical cross-section of scanning geometry. *b)* Reconstructed vertical cross-section (FDK algorithm).

3.2.3 Potential for limited view angle tomography

For both scanning geometries the limited view angle artifacts are formed in such a way that they cover especially cracks which are parallel to the PCB surface. This stems from the fact that we cannot take projections from this direction. However, some information is existing from the available views and the defects may be recovered if prior knowledge of the object could be additionally included into a suitable reconstruction algorithm. The requirements for such an algorithm would be extremely high because we look at a multi material system with complex geometry for which a very high spatial resolution is desired. At this stage this was not possible.

3.3 Example 3: 2D CT of the Bat Phantom

3.3.1 Phantom definition and classification

The Bat Phantom (Fig. 3.8 a) is the sample which was specially designed and studied in detail for this work. It represents large and strongly absorbing metal objects for which the X-ray signal is not detectable from some view angles. To be more specific we consider single material objects which have an oblong cross-section if they are aligned in an optimal way for CT. A relevant industrial object is e.g. a gas turbine blade. 3D non-destructive testing (NDT) of gas turbine blades with an X-ray CT set-up which can be installed into a production line would be a favorable task and this was a strong

motivation for our work. We tried to classify the problem as follows:

- Sample category: Large and strongly absorbing metal objects which have an oblong cross-section and consist of only one single material, e.g. turbine blades.
- NDT task, Stage 1: Verification of the internal geometric structure with 100-200 μm accuracy. Stage 2: Detection of subsurface defects and cracks in the range of 10-100 μm.
- Feasibility: To be investigated in this work.

The size of our phantom (70x16 mm) was chosen to be critical for typical CT systems which use X-ray tubes. It is made of copper, which has similar absorption properties for X-rays as inconel (the base material of turbine blades) and is easier to machine. The smallest phantom feature is a Ø 0.5 mm drilling hole. For our investigations we further used a simulation model which has exactly the same cross-sectional dimensions as the real phantom (Fig. 3.8 b). A design drawing is shown in the appendix in Fig A.1.

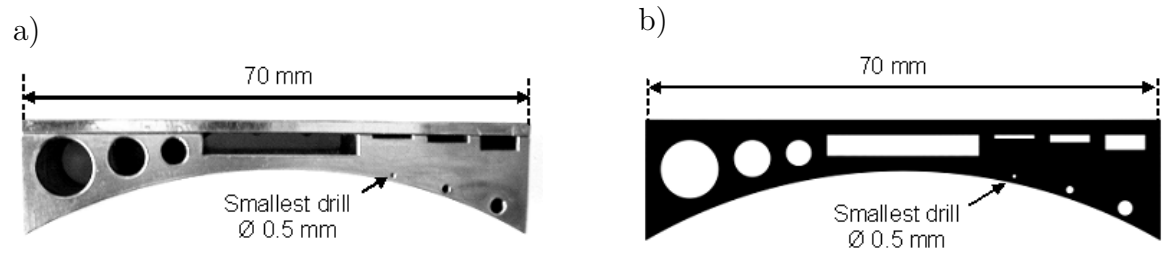

Figure 3.8: *a)* Photo and *b)* simulation model of Bat Phantom. The phantom is made of copper and the dimensions were identical in both cases.

3.3.2 Scanning with limited X-ray penetration

Our main results will be presented in the following chapters. Here we would like to put the problem briefly into context with the previous examples. For simplification we considered a 2D CT configuration and assumed a full rotation of the object. Due to the oblong shape and the strong absorption of the Bat Phantom the detection of the X-ray signal was not possible for a small range of view angles as indicated in Fig. 3.9 a). This situation is comparable to a partial circular scan, which was discussed for the BGA example, and the 2D FBP reconstruction of simulated data shows similar rhombic shaped artifacts (Fig. 3.9 b). For the simulation we used 160 keV monochromatic X-rays and a reduced dynamic range of 350:1 (see next chapter).

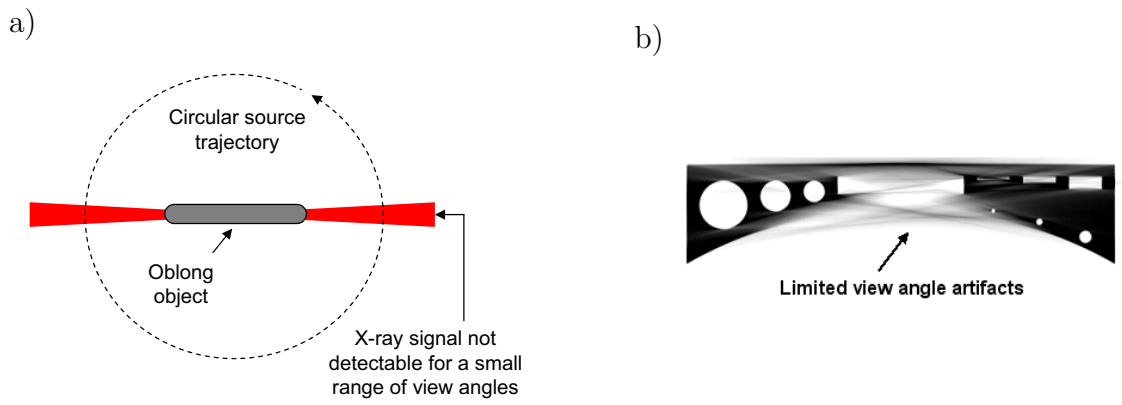

Figure 3.9: *a)* 2D scanning scheme for Bat Phantom. *b)* 2D FBP reconstruction of simulated data with reduced dynamic range.

3.3.3 Potential for limited view angle tomography

Aiming at a solution of the problem we will investigate the performance of iterative algorithms which include prior knowledge of the object. Taking into account the experimental conditions and the available reconstruction algorithms we focussed on the following case:

2D limited view angle tomography of oblong single material objects using a moderate size for the reconstructed image in the order of 10^4 pixels[1].

With the help of simulated projection data we will demonstrate the principal possibilities in chapter 4 and the experimental issues are analyzed in chapter 5.

3.4 Masking of missing points in Fourier space

Before we close this chapter we would like to explain in more detail that the observed rhombic shaped artifacts are caused by incomplete sampling and do not depend on a certain reconstruction algorithm. We know from theory (chapter 2.2.4) that limited view angles result in missing points in Fourier space. If we assume 3D parallel beam geometry we can distinguish between a missing double cone for tomosynthesis and a missing double wedge for the partial circular scan. Although parallel beam geometry is not what we usually have in an experiment we consider these two fundamental cases as adequate for a qualitative analysis.

[1]For comparison: In 3D micro-focus CT the number of volume pixels can easily be larger than 10^9.

Using the 3D discrete Fourier transform (DFT) we can show that the artifacts in the object space are directly related to the missing points in the Fourier space. The specialty of this transform is that the considered spaces are discrete and that it is a one to one relation. If we define an arbitrary object we can transform it and easily manipulate the points in the discrete Fourier space. The result of the manipulation can be seen in object space after applying the inverse transform. For our purpose the manipulation is to set all points to zero which correspond to the missing points, i.e. all points which are defined by a mask which is given by a double cone or a double wedge. In this way we imitate the real process without using a specific reconstruction. An illustration is given in Fig. 3.10.

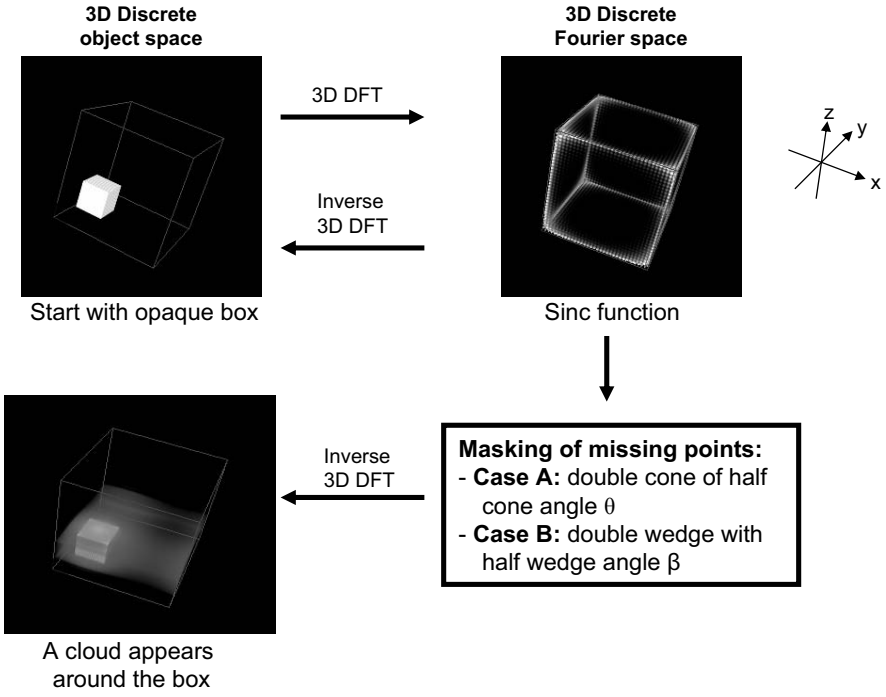

Figure 3.10: Process of masking the missing points for an opaque box.

For an object we defined an opaque box which is transformed to a sinc function. The number of discrete points was 128^3. The fact that the sinc function is spread to the corners of the cubic space is related to the specific definition of the discrete coordinate system which is commonly used for the discrete Fourier transform [Jaeh93]. The discrete masks were defined accordingly which is not shown explicitly here. Instead we visualize the masks in Fig. 3.11 as the they would appear in the continuous 3D Fourier space. Another important aspect is that the edges of the masks were smoothed by an error function (integral of Gaussian function) to avoid unwanted oscillations.

We chose the same orientation for the wedge and the cone. As we applied the inverse transform without masking we got back the original object but after the masking a cloud

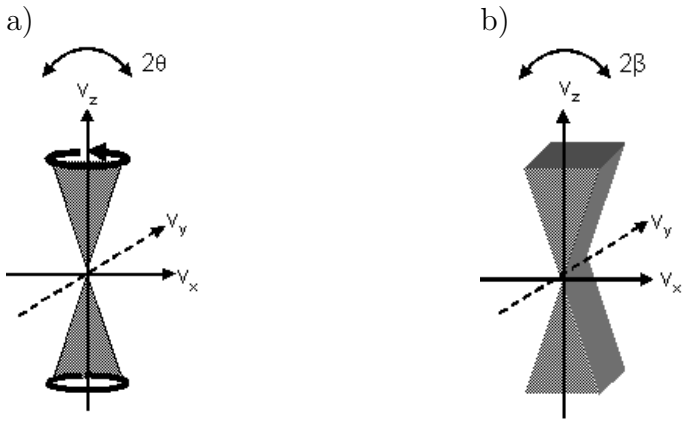

Figure 3.11: Shape and orientation of the considered masks: *a)* double cone with half cone angle Θ and *b)* double wedge with half wedge angle β. Visualization in continuous 3D Fourier space.

appeared (see Fig. 3.10). The resulting vertical cross-sections at the center of the box are shown in Fig. 3.12.

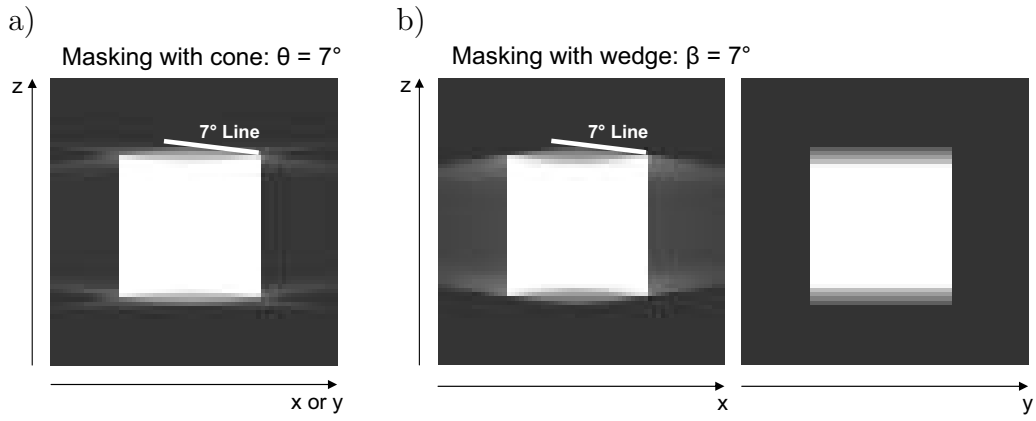

Figure 3.12: Vertical cross-sections after masking with *a)* cone and *b)* wedge.

Rhombic shaped artifacts are visible in both cases, i.e. for the cone and wedge mask. This is very impressive because it reflects our experimental observations and as before the half shape angles are approximately equal to the half cone angle Θ and the half wedge angle β respectively. Both angles were 7° which is indicated by the 7° lines in the figure. This confirms our assumption that the artifacts are directly related to the missing points. Further, the symmetry of the masks seems to imply the symmetry of the artifacts. For the cone mask (rotational symmetry) both vertical cross-sections (x-z and y-z) are identical but for the wedge they are different. The y-z cross-section for the

wedge mask shows a rectangular shaped artifact in accordance with the alignment of the leading edge of the wedge which was parallel to the y-axis (translational symmetry). This illustrates that the tomosynthesis configuration has an advantage compared to the partial circular scan if $\Theta = \beta$.

4 Simulation results for the Bat Phantom

Motivation

In the previous chapter we examined basic cases where limited view angles occur and showed that the associated artifacts in filtered back projection (FBP) reconstruction have a characteristic rhombic shape. Above all we defined a suitable problem for our further analysis, i.e. the 2D CT of the Bat Phantom with limited X-ray penetration for a small range of view angles (see Fig. 3.8 and Fig. 3.9). Now we investigate how a solution can be achieved with iterative reconstruction algorithms if prior knowledge of the object is included. Using simulated projection data we evaluate the performance of different algorithms for various parameters.

The parameter which controls the amount of lacking data is the dynamic range. At first we will use an infinite dynamic range for which the complete data can be sampled. If no additional distortions occur (ideal monochromatic data) FBP is exact and the image quality and reconstruction time are unbeatable compared to iterative algorithms. Aiming at sophisticated applications we wanted to know if an iterative algorithm could at all achieve a similar quality in a reasonable time. For this purpose we look at a high resolution reconstruction with SART (without prior information) which is the most developed type of iterative reconstruction. In contrast to this ML-TR has a lower performance but shows special properties.

The next step will be to reduce the dynamic range such that limited view angle artifacts occur in FBP. In this case we choose a smaller image size for a prove of principle. Looking at SART, ML-TR and DT we show that the artifacts can be avoided if the single material and smoothness prior information is included into the reconstruction. We evaluate the effect of different types of prior knowledge representatively for SART. In order to prepare our experiments which are presented in the next chapter we analyze how distortions like e.g. noise or polychromatic X-rays affect the result.

4.1 Simulation of X-ray projection data

For the simulation of the projection data we used a program which has been originally developed for medical CT. It can model an arbitrary scanning geometry and uses regular geometric shapes to define the phantom. Fig. 4.1 shows a simple 2D example where the object is composed of an ellipsoid (shape G1, material M1) and a cuboid (shape G2, material M2). The projection is performed via needle rays which start at a point source and end at points on a line which defines the detector. In addition to the object the simulation can optionally include a beam hardening filter and a scintillator for detection. Further it can use an arbitrary energy spectrum and add quantum noise to the result. The influence of a focal spot and a finite pixel size were neglected. An important aspect is that the phantom is defined by exact boarders, i.e. the shape edges are sharp and as a consequence the object is not bandlimited.

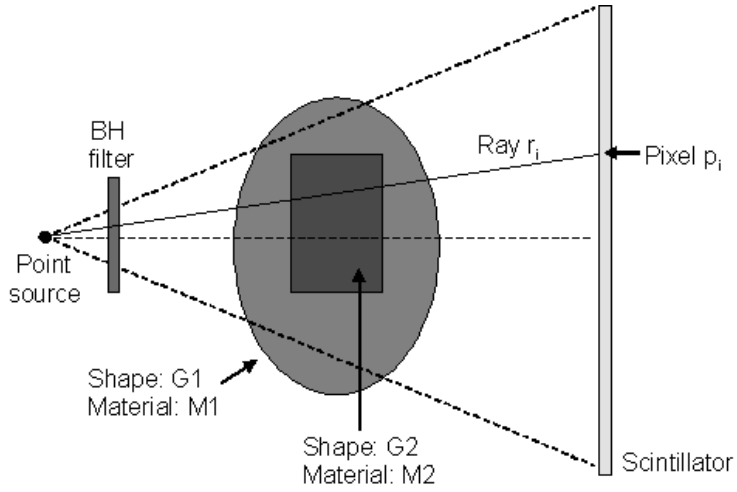

Figure 4.1: Simulation process

The projections are computed by using the exponential absorption law for X-rays (review Eqn. 2.4) and tabulated values for the absorption coefficient $\mu(E)$. In order to obtain the detected intensity for a specific ray (ray r_i in the figure) the attenuation for each shape which intersects the ray, the attenuation in the beam hardening filter and the absorption in the scintillator is computed for each energy and integrated over the spectrum. For the attenuation in the ray path the total attenuation is used, i.e. scattered rays are assumed not to be detected and for the detection process photoelectric absorption is considered. Strictly these approximations are only valid for lower energies (medical applications). In non-destructive testing we typically have higher energies and scattering can play an important role in experiments which will be discussed in the next chapter.

An important note is that the computation is performed in floating point arithmetic,

i.e. the dynamic range is infinite at first and can be reduced in order to model an experiment. The reduction was performed by setting the values below a certain threshold to this minimum value. This is a simple model for a saturation at the limit of the dynamic range in a real system. Further we scaled all projections to a given direct beam intensity. The following list summarizes the options which were used for our analysis:

- Spectra: 200 kV polychromatic [Ank00], 160 keV monochromatic
- Beam hardening filter: 0, 0.5 or 5 mm Cu
- Detector types: Ideal (100% absorption), 0.6 mm CsI or 6 mm $CdWO_4$ scintillator
- Quantum noise: 0%, 2% or 10% relative to the direct beam intensity
- Direct beam grey level: $I_0 = 50000$
- Dynamic range: infinite or reduced to 350:1 (8.5 bit)

We will use the term ideal projection data for monochromatic X-rays, an ideal detector and no noise (scattering is not included anyway). However, the dynamic range can be reduced in this case. This might be a bit confusing at first, but we want to express that the data itself is not distorted by physical factors and consider the dynamic range independently. A beam hardening filter is only relevant for polychromatic X-rays. For the detection of polychromatic X-rays we used a 0.6 mm CsI scintillator like in our experimental set-up at Siemens (see chapter 5).

4.2 Infinite dynamic range

4.2.1 High resolution reconstruction with FBP and SART

Now we look at the reconstruction of ideal projection data with infinite dynamic range. The simulation was performed for a monochromatic energy of 160 keV. Fig. 4.2 compares the results for a high resolution FBP and SART reconstruction of 640×180 image pixels. Limited view angle artifacts are not an issue here. It is remarkable that SART achieves a similar image quality as FBP. This was possible by a fine tuning of the reconstruction parameters for SART which is discussed in the next subsection ($\lambda = 0.1$, 'Bessel-Kaiser CP', 'WDS', 30 iterations).

For the presentation of the reconstructed images we have zoomed into the display range, i.e. we selected a range of $\pm 10\%$ relative to the material value and assigned it to the full grey scale between black and white, i.e. if the image is normalized and air corresponds to a value of 0 and material to 1 then all values below 0.9 are white and those above 1.1

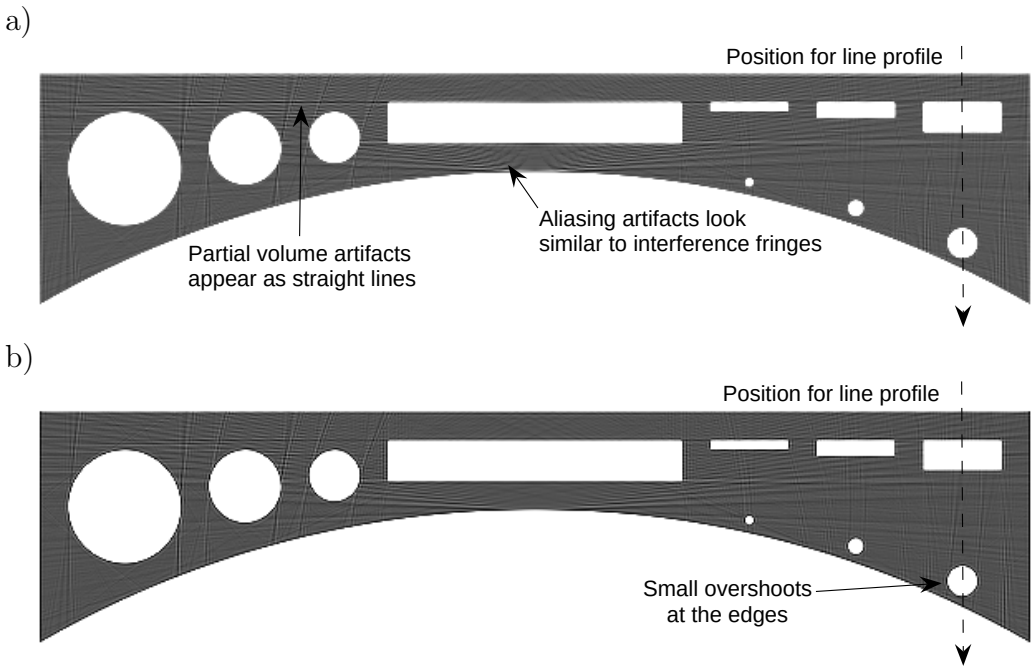

Figure 4.2: *a)* FBP and *b)* SART reconstruction of ideal data with infinite dynamic range. The display ranges for visualization were zoomed in the same way for both cases.

are black in the image. Therefore aliasing and partial volume artifacts become visible. They appear in both cases and emerge from the discrete sampling of the object. In our simulation aliasing is particulary relevant because the object is not band limited (review sampling theorem in chapter 2.2). We want to point out that these artifacts can only be reduced but never completely avoided by a higher number of detector pixels (here 660) and projections (here 1250). To exclude any other effects we used parallel beam geometry. For details about the configuration see next subsection.

Regarding our implementation, the reconstruction times were about 120 min for SART using 30 iterations and 1 min for FBP on a 2 GHz computer. This corresponds to a factor of 4 in time per iteration in comparison to FBP and we expect that further improvement is possible. Considering that FBP uses only one back projection and that each SART iteration needs a forward and a back projection we can estimate a lower limit of 2 per iteration for this factor. Moreover the number of iterations itself may be reduced but the optimization of the reconstruction time is a different field of research and here we wanted to give an impression of what can be achieved for the image quality.

A more precise view of the amount of artifacts is obtained from the line profiles in Fig. 4.3 a) for FBP and b) for SART. The selected profiles were taken at the positions which were indicated by the dashed lines in the images. In each plot the profile of the original object is given as a reference. The agreement of the reconstructed shape

is excellent and further the absolute pixel values were reconstructed correctly. For a better interpretation we normalized all plots by the material absorption. As observed before the aliasing artifacts appear as small oscillations. They are a little bit larger for SART for which additional overshoots occur at the edges. This is hardly visible in the image but can be clearly resolved here. In general aliasing can be critical in iterative reconstruction and a higher number of iterations does not necessarily improve the result (see next subsection).

a) b)

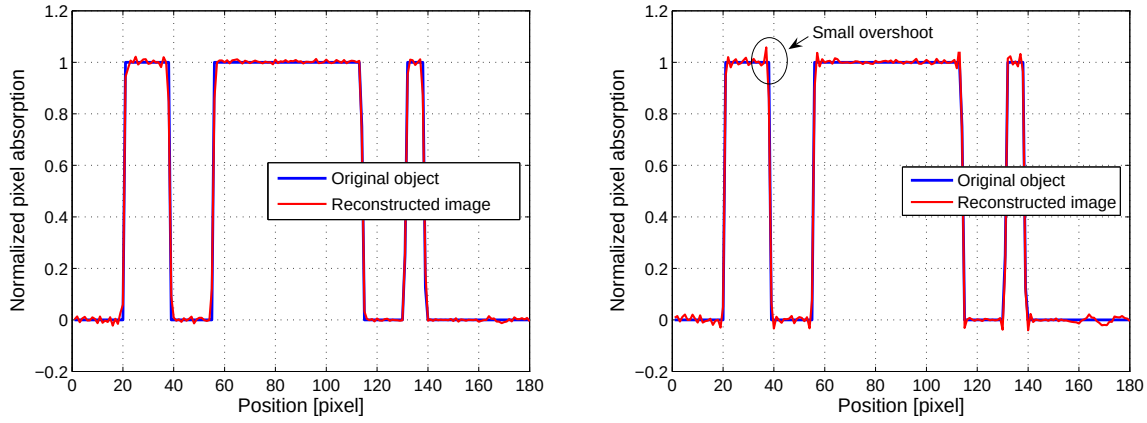

Figure 4.3: Line profiles for *a)* FBP and *b)* SART reconstruction of the Bat Phantom. They are compared to the profiles of the original object.

4.2.2 Reconstruction options for FBP and SART

In the following we will explain the parameter settings for the previous reconstructions. We will briefly look at FBP and then focus on the options for SART. The considered optimization task was to achieve an image quality of SART which is comparable to FBP. We go to details here because we consider SART as a good example to point out basic implications in iterative reconstruction.

Measuring the image quality

In order to measure the image quality we need an appropriate quantity. For this purpose we computed the euklidean distance from the reconstructed image $(v_j)_1^N$ to the original image $(v_j^0)_1^N$:

$$d_{\text{eukl}} = \sqrt{\sum_{j=1}^{N} (v_j - v_j^0)^2} \,, \tag{4.1}$$

where N is the number of image pixels. This should not be confused with a spatial distance. We look at the values of the image pixels and not at their position. The value v_j of an individual pixel j specifies the attenuation of an X-ray which passes by. It is the contribution of this pixel to the line integral

$$v_j = \mu_j \Delta x \ , \tag{4.2}$$

where μ_j is the linear absorption coefficient and Δx the object pixel size. Thus the computed distance is a distance of attenuation values and we can normalize it by the attenuation of one material pixel:

$$d^0_{\text{eukl}} = \frac{d_{\text{eukl}}}{\mu_{\text{Material}} \Delta x} \ . \tag{4.3}$$

The resulting normalized distance d^0_{eukl} is equivalent to a number of material pixels which sum up to the same attenuation. Therefore one might think of comparing d^0_{eukl} to the total number of image pixels but this is not useful because of a non-linear behavior. Strictly d^0_{eukl} should only be used to compare images of the same size (number of image pixels) and type (binary or continuous). To get a feeling for this quantity we can look once more at the reconstructed images (Fig. 4.2) and the line profiles (Fig. 4.3). In this case d^0_{eukl} directly measures the amount of aliasing artifacts. The values were 6.6 for FBP and 7.1 for SART.

Geometric configuration

In addition to parallel beam geometry which was used for the presented examples we will now also look at fan beam geometry. Tab. 4.1 summarizes the geometric parameters

Beam geometry		Parallel beam	Fan beam
SDD	(Source detector distance)	$10^6 + 100$ mm	1000 mm
SOD	(Source object distance)	10^6 mm	200 mm
M	(Magnification)	≈ 1	5
Δx_{D}	(Detector pixel size)	0.12 mm	0.6 mm
Δx	(Nominal pixel resolution)	0.12 mm	0.12 mm
N_{D}	(Number of detector pixels)	660	660
$\text{N}_{\text{x}} \times \text{N}_{\text{y}}$	(Size of reconstructed image)	640×180	640×180
β_{max}	(Angular range for scanning)	180°	360°
N_{P}	(Number of projections)	1250	1250

Table 4.1: Geometric parameters for the simulation.

which were assumed for the simulation of the projection data. For a principal explanation of CT configurations we refer to the theory chapter (review sections 2.1.1 and 2.2.3). Here we approximated the parallel beam geometry by a point source at a very large distance form the detector which was sufficiently accurate. For the fan beam we chose a typical experimental value of SDD=1000 mm and adapted the detector pixel size Δx_{D} and the magnification M in order to obtain the same nominal pixel resolution Δx at the object position as in the parallel case. Therefore the number of detector pixels $\mathrm{N_D}$ for scanning the Bat Phantom and the image grid for its reconstruction were identical for both cases. The size of the reconstructed images was 640×180 pixels.

Basic reconstruction parameters

At first we want to verify how many projections are needed. Strictly speaking, this is not a reconstruction parameter but a matter of sampling and we presume that it is equal or at least very similar for SART and FBP. Therefore we can confine this investigation to FBP which has the advantage that there are no further options which interact. In Fig. 4.4 a) we plotted the normalized distance versus the number of projections $\mathrm{N_P}$. The reconstruction quality improves for larger $\mathrm{N_P}$ at first, but then reaches a limit at an optimum number of projections $\mathrm{N_{P0}}$. It does not further improve for $\mathrm{N_P} \geq \mathrm{N_{P0}}$. This behavior is similar for parallel and fan beam geometry. The maximum image quality which can be achieved in each case is about the same, however, for parallel beam geometry less projections are required.

a) b)

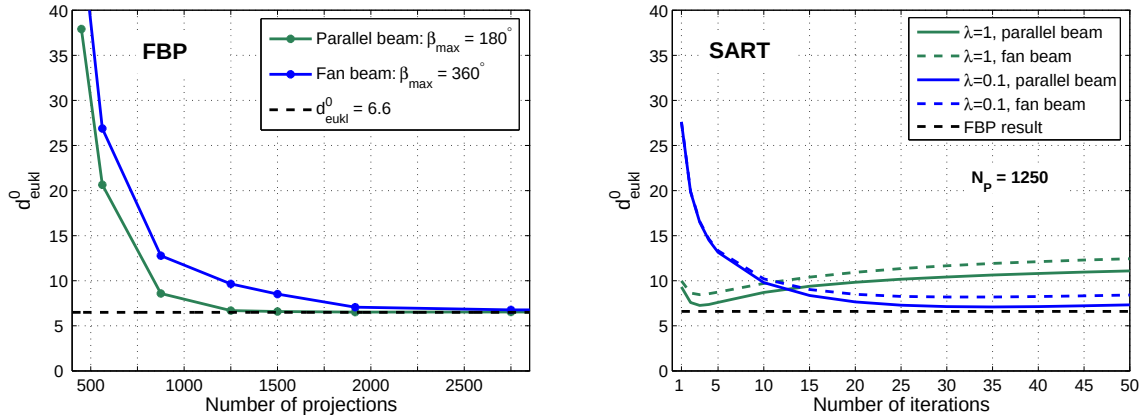

Figure 4.4: Dependence of reconstruction quality on basic parameters. *a)* FBP: Variation of the number of projections and the projection geometry. *b)* SART: Variation of the number of iterations, the relaxation parameter λ and the projection geometry.

Tab. 4.2 collects the values which were estimated from the plot. For parallel beam geometry we scanned an angular range of 180° and the optimum number of projections was $N_{P0} \approx 1000$. Dividing it by the number of detector pixels $N_D = 660$ we obtain approximately a factor of $\frac{\pi}{2}$ which is expected from theory (review chapter 2.2.3). This factor was about two times larger for the fan beam where a full 360° scan was performed. The explanation for this circumstance is that the angular increment at the optimum should be the same for both beam geometries. Regarding the image quality the minimum value for d^0_{eukl}, which was achieved at the optimum, was 6.6 for parallel and 6.8 for fan beam geometry (recall that this value is related to aliasing, which occurs because the object is not bandlimited in our simulation).

Geometry	$\beta_{\max}$	N_{P0}	$\frac{N_{P0}}{N_D}$	$d^0_{\text{eukl}}(N_{P0})$
Parallel beam	180°	1000 ... 1250	1.5 ... 2	6.6
Fan beam	360°	1700 ... 2500	3 ... 4	6.8

Table 4.2: Optimum number of projections N_{P0} and comparison to the number of detector pixels N_D for FBP in the considered example.

After the optimum number of projections has been found we can focus on the reconstruction options for SART. Now we will vary the two most fundamental parameters which are the number of iterations and the relaxation parameter λ. The impact of the other options will be described later and here we set them to optimum values ('Bessel-Kaiser CP' and 'WDS'). In Fig. 4.2 b) the reconstruction quality is plotted versus the number of iterations. It shows the importance of the relaxation parameter λ and the independence of the beam geometry. Actually the plots for parallel and fan beam geometry were separated by a small difference because we used a fixed number of projections $N_P = 1250$ which is large enough for parallel beam geometry but a little bit below the optimum for fan beam geometry.

We compared two values for the relaxation parameter: $\lambda = 1$ and $\lambda = 0.1$. Considering the normalization of the update formula (review Eqn. 2.21) $\lambda = 1$ should be ideal but we observe an oscillation in the plot. Although the image quality approximately reaches the FBP level after only three iterations it decreases again for a larger number of iterations. This kind of instability can be reduced with a smaller relaxation parameter but then the convergence slows down as well. In the example of $\lambda = 0.1$ we need 30 iterations to achieve FBP quality but the stability increases significantly. This setting was used for the presented images above (review Fig. 4.2 b). It was a compromise where we preferred stability before speed.

Resorting of projections and projection model

The interpretation of the oscillation which was observed in Fig. 4.2 b) for $\lambda = 1$ is that aliasing artifacts can be induced and magnified by the iterative process. We will see that the amount of distortion strongly depends on the choice of the projection model and as this is a field of recent research we can expect future improvements. Ideally the forward projection, which is used in the reconstruction and computed by the projection matrix H, would be an exact model of the physical projection process. We can imitate this ideal case by 'internal projection data' (review section 2.3.2), i.e. by sampling the Bat Phantom to the image grid and using the forward projection itself to generate the set of 'measured' projection data which is to be reconstructed.

Fig. 4.5 a) shows the result for the relaxation parameter $\lambda = 1$ and parallel beam geometry. The convergence is excellent and without oscillations. In other words we can say that aliasing does not occur because the 'needles' (projection rays) which were used for generating the 'measured' projection data are identical to those used in the reconstruction. We should add that the result for FBP did not improve because in this case a single back projection is used which cannot benefit from the matched forward process.

a) b)

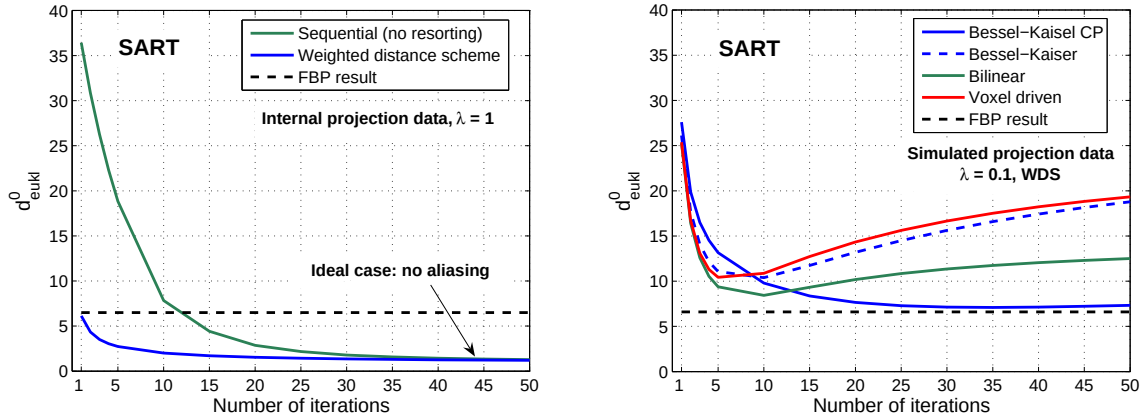

Figure 4.5: SART: *a)* Imitation of the ideal case with 'internal projection data' and effect of resorting the projections with the weighted distance scheme (WDS). *b)* Comparison of different projection models for the reconstruction of simulated projection data.

An important option to speed up the convergence is to resort the order of the projections before the reconstruction. In the plot (still looking at Fig. 4.5 a) we compare the sequential order to the weighted distance scheme (WDS) where the projection angles are distributed in such a way that they have the largest possible angular distance to each other (review section 2.3.2). In both cases the image quality converges to the same value

but the WDS is much faster. Tab. 4.3 shows selected values from the plot. The achieved normalized euklidean distance is $d^0_{\text{eukl}} \approx 1$ after 50 iterations, which is very impressive. From the point where the convergence slows down we estimate that a good choice for the number of iterations is between 10 and 30 if the WDS is used.

$N_{\text{Iteration}}$	3	5	10	20	30	40	50
d^0_{eukl} (WDS)	3.51	2.73	2.01	1.54	1.36	1.26	1.20
d^0_{eukl} (Sequential)	22.3	18.8	7.84	2.87	1.77	1.44	1.28

Table 4.3: SART reconstruction quality for internal projection data.

Although the internal projection data is of no practical relevance it gives us the clue to the best achievable performance in iterative reconstruction. It is a special quality of this work that we did not constrain our investigations to the ideal model. Instead we looked at the more realistic case where the projection data is generated externally by our simulation program, or even obtained from a real experiment. Therefore we needed to accept imperfections and as discussed before a smaller value for λ was helpful to achieve a stable convergence. Fig. 4.5 b) shows the performance of different projection models for simulated projection data ($\lambda = 0.1$, WDS and parallel beam geometry). The Bessel-Kaiser interpolation kernel with convolved projections (Bessel-Kaiser CP) is best. This implies that we talk about a ray driven projection model with interpolation in the reconstructed image. If we turn off the optional convolution of the projection data we observe again a strong oscillation. In this case the performance was only similar to the voxel driven model which uses a linear interpolation at the detector. Coming back to the ray driven model the bilinear interpolation was mediocre.

4.2.3 Distinction of ML-TR

The maximum likelihood transmission (ML-TR) reconstruction algorithm stands out for its special properties. It was derived using a correct noise model and directly reconstructs from intensity values (SART reconstructs from line integrals). Most important for our work is that it pays less weight to small projection values and as a consequence the central region in the Bat Phantom is reconstructed very slowly. This is shown in Fig. 4.6 a) after 1000 iterations and in Fig. 4.6 b) we see that even 15000 iterations are not sufficient for a complete reconstruction. It is a massive effect and in order to save reconstruction time we had to reduce the pixel resolution compared to our SART example from before. The size of the images was only 240×70 and the number of projections 360, resulting in a reconstruction time of about 1 h per 1000 iterations.

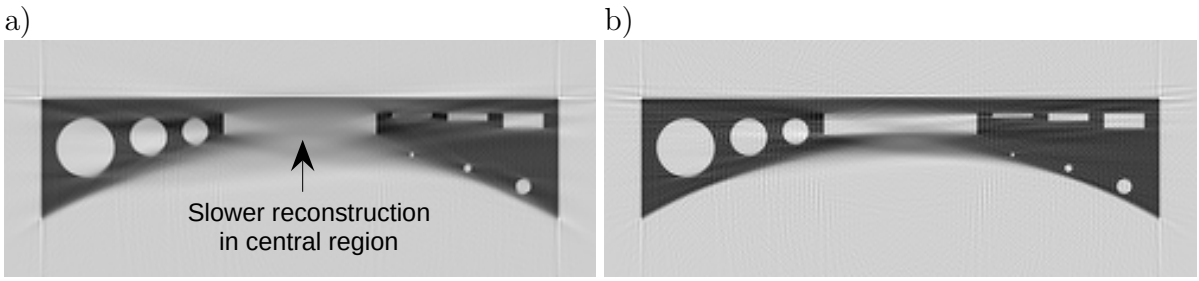

Figure 4.6: ML-TR reconstruction of the Bat Phantom with moderate spatial resolution: *a)* 1000 iterations and *b)* 15000 iterations

The extent of the observed effect is closely related to the object properties. For the Bat Phantom the absorption is quite strong and the transmission intensities become particularly small in the directions which are critical due to the oblong shape. Therefore in the reconstruction the weight of these view angles is drastically reduced. This is similar to the limited view angle problem where the information from these view angles is not available at all. If ML-TR is used in the latter case the missing information is given less weight and we will see the benefit later.

Considering the reconstruction options of ML-TR we can mostly transfer the dependencies on the different parameters from SART. However, two options change. The first is the image update scheme or to be more precise the number of projections which are processed in each update step (N_{up}): For ML-TR the image is not updated until all projections have been processed while for SART an image update is performed after each projection. Secondly for ML-TR the 'Bessel-Kaiser CP' option for the projection model is not suitable (review theory section 2.3.3) and we chose the bilinear model instead. Fig. 4.7 a) shows the convergence plot for $\lambda = 1$ (and weighted distance scheme). If the number of projections which are processed in each update step is reduced from N_{up}=360 (all projections) to N_{up}=25 the convergence can be improved significantly. However,

the achieved minimum euklidean distance d^0_{eukl} (review Eqn. 4.3 for definition) is worse compared to the corresponding FBP result. Due to the high number of iterations and the bilinear interpolation aliasing is particulary strong.

a) b)

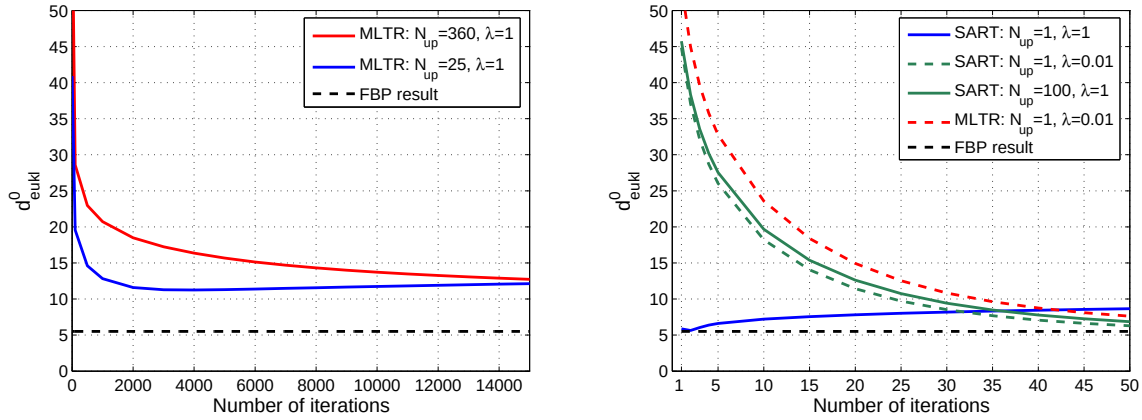

Figure 4.7: Convergence for *a)* ML-TR and *b)* SART using different image update schemes (N_{up} = number of projections which are processed in each update step).

A problem coming up with reducing N_{up} too much is that at the same time ML-TR will loose its special properties. With N_{up}=25 we found a reasonable setting for our experiments in the following sections. If $N_{up} = 1$ is used instead, all the properties are lost and the result is similar to SART. This is shown in Fig. 4.7 b) for the plots with relaxation parameter $\lambda = 0.01$ where FBP quality is achieved after 50 iterations. In contrast to ML-TR, for SART a larger N_{up} is merely equal to a reduction of λ (compare plots for N_{up}=1, $\lambda = 1$; N_{up}=1, $\lambda = 0.01$ and N_{up}=100, $\lambda = 1$). This emphasizes once more that ML-TR is unique in its properties.

4.3 Reduced dynamic range

In the following the dynamic range (DR) of the simulated projection data was reduced to a ratio of DR=350:1 which corresponds to 8.5 bit (review section 2.1.4 for definition). This value was estimated from early experiments. For a solution of the reconstruction problem we investigate the effect of prior knowledge of the object which is included into SART, ML-TR and DT. An important aspect is that the X-ray signal is not correct at the limit of the dynamic range and such values have to be skipped in the reconstruction. In this sense the situation is equivalent to a limited geometric access. We distinguish between the following prior options (review theory section 2.4):

- **Option '01':** Single material prior information. For a single material object like the Bat Phantom only two values are possible for the reconstructed pixels, i.e. '0' for air and '1' for material where we assume a normalization to the material absorption. While this information is intrinsically included in DT it has to be imposed on SART and ML-TR by repeated segmentations. In the latter case it is important that the strength of the segmentation is small at the beginning and is only slowly increased with the number of iterations, otherwise the shape of the object can be distorted or even break up.

- **Option 'SM':** Smoothness penalty term. The information that the object is smooth, i.e. mostly homogeneous, can be included in a general form into the optimization equation for DT while for SART and ML-TR a more specific term is adapted to the reconstruction formula. In all cases the smoothness information is given some weight which has to be tuned carefully. If it is too strong small object features and edges are smeared out.

- **Option 'PV':** Peel volume. In this case we reconstruct only those image pixels which are within a tight envelope of the original object. Here we only test this option for SART. In practice such an envelope could be obtained e.g. by an optical measurement.

4.3.1 Limited view angle tomography for ideal data

We start our analysis and reconstruct ideal projection data as we have used it in the previous section (160 keV monochromatic, no noise, no scattering). Concerning the image resolution we had to make a compromise. Due to a high computational effort it was not feasible to strive for a high resolution. For a prove of principle we selected a fan beam configuration with a small magnification yielding an image size of 240×70 pixels. The parameters are given in Tab 4.4 and they correspond to an existing micro-focus CT set-up.

Beam geometry		Fan beam
SDD	(Source detector distance)	1000 mm
SOD	(Source object distance)	800 mm
M	(Magnification)	1.25
Δx_{D}	(Detector pixel size)	0.4 mm
Δx	(Nominal pixel resolution)	0.32 mm
$\mathrm{N_D}$	(Number of detector pixels)	250
$\mathrm{N_x} \times \mathrm{N_y}$	(Size of reconstructed image)	240×70
$\beta_{\max}$	(Angular range for scanning)	360°
$\mathrm{N_P}$	(Number of projections)	360

Table 4.4: Geometric configuration for limited view angle tomography.

Fig. 4.8 shows the results for FBP, SART, ML-TR and DT. We clearly see that the limited view angle artifacts which are visible in FBP do not appear for the iterative algorithms where we included the single material (01) and the smoothness information (SM). This demonstrates that a solution of the given problem is principally possible. The best result was obtained for SART because we could set up on and profit from the optimizations which were achieved for the infinite dynamic range. From this point of view it was not a surprise that ML-TR stands back a little bit. So far its distinct properties do not seem to be a particular advantage.

The presented DT result is even a bit worse than ML-TR. Some shape deformations can be seen, i.e. the second circle from the left is reconstructed octagonal and the large rectangular gap in the center is too narrow. We suspect that the aliasing in the simulated data may be the cause of trouble and assume that further optimizations are possible. In fact DT is a very recent approach and we think that it has a lot of potential because it is most fundamental and allows the inclusion of any kind of prior information in a general form. In contrast to this, for SART and ML-TR the inclusion of prior knowledge is a bit clumsy and for them further extensions are questionable.

Like in the previous section we can measure the reconstruction quality by the normalized euklidean distance d^0_{eukl} (review Eqn. 4.3 for definition) and the computed numbers are given in the figure. As mentioned before the behavior of d^0_{eukl} is non-linear and strictly we should not compare the values for continuous and binary images. Nevertheless, we found that d^0_{eukl} is suitable to describe the overall impression very well. The time values in the figure are the reconstruction times on 2 GHz computers. Due to the small size of the images the relevant coefficients of the projection matrix could be fully stored into the RAM which led to a significant acceleration.

Some experience is required to tune the reconstruction parameters for SART and ML-TR. The impact of the segmentation is quite phenomenological and we proceeded by trial

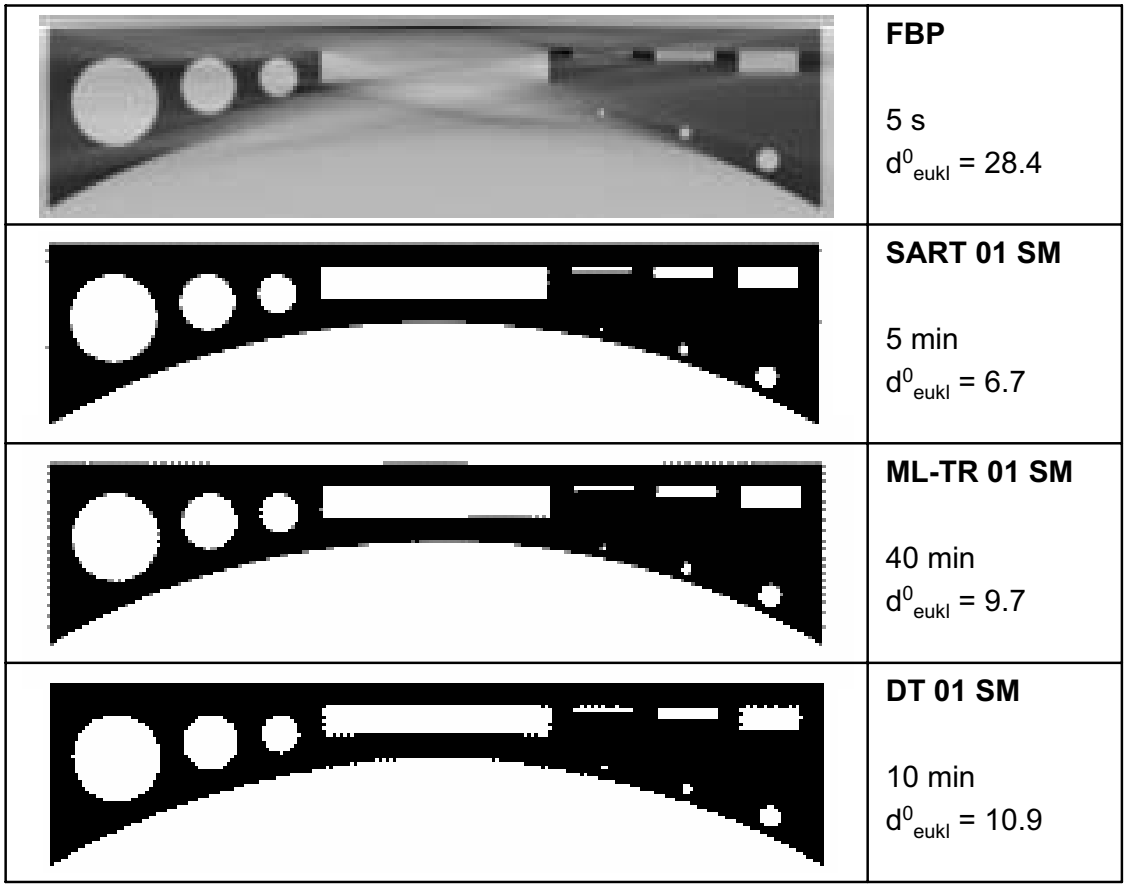

Figure 4.8: FBP and iterative reconstruction with prior knowledge for ideal data (160 keV monochromatic, no noise, no scattering) with a reduced dynamic range of 350:1 (8.5 bit).

and error. A list of the chosen values is given in Tab. 4.5. In contrast to our previous investigations where we focussed merely on the image quality we tried to minimize the number of iterations as much as possible. For SART this was more or less straight forward. With respect to the other settings the selected λ is quite high and therefore the convergence is fast which justifies a small value for N_1. The situation is different for ML-TR which converges extremely slowly without segmentation (review Fig. 4.7 a). Nevertheless with a reduced value for N_{up} we could choose relatively small values for N_1 and N_2 but point out that the handling was particularly tricky. Considering DT the optimization was done at the University of Szeged and we cannot discuss details here. It is an interesting fact that the result for DT can slightly change if the reconstruction is repeated. This is due to the statistical nature of the simulated annealing optimization method. For all algorithms the weight of the smoothness information was set as strong

as possible such that the object details are not smeared out. As mentioned in the introduction to this section we skipped all values at the detection limit and we will see more details about this in the next subsection.

	SART	ML-TR
Relaxation parameter λ	0.1	1
Projection model	bilinear	bilinear
Projection resorting	WDS	WDS
Projections per image update N_{up}	1	25
Iterations before segmentation N_1	3	5
Number of repetitions N_2	20	100
Total number of iterations $N_1 \cdot N_2$	60	500
Threshold range DTH	40%	40%

Table 4.5: Reconstruction options for SART and ML-TR with segmentation.

4.3.2 Different types of prior knowledge

The effect of different types of prior knowledge was studied representatively for SART. We do not show all the images but give a concise summary of the results with the help of the normalized distance d^0_{eukl} (review Eqn. 4.3 for definition). The obtained values are given in Tab. 4.6 and the reconstruction options were the same as before except for the cases without prior knowledge where simply 5 iterations were used. First of all we see what was discussed in the previous section: for an infinite dynamic range SART ($d^0_{\text{eukl}} = 6.5$) and FBP ($d^0_{\text{eukl}} = 5.5$) are comparable. In fact this is also true for the reduced dynamic range if no prior knowledge is applied (27.4 and 28.4).

Dynamic range	Infinite	Reduced 350:1				
Prior information	No	No	01	01 SM	01 PV	01 SM PV
FBP	5.5	28.4	-	-	-	-
SART	6.5	27.9	9	6.7	10.4	6.6

Table 4.6: Values of d^0_{eukl} for different types of prior knowledge.

This explicitly proves that prior knowledge of the object is the key to compensate for the lack of data in limited view angle tomography. We found that the single material information ('01') is most important yielding $d^0_{\text{eukl}} = 9$. Further a significant improvement is achieved by the smoothness prior ('SM') giving a result of 6.7 which appears to be as good as for the reconstruction of data with infinite dynamic range. However, one has to

be careful with this interpretation because the errors in the binary image are distributed over much less pixels than in the continuous image.

We were a bit surprised that the peel volume ('PV') did not improve the result. It was defined by an envelope of the exterior shape of the object leaving a gap of only one pixel. A possible interpretation is that this may be a bit too 'aggressive' compared to the gradually increasing segmentation. This was similar for ML-TR (not shown) but for DT the result may be different what could not be verified at this stage. We point out that the process of the image formation is not comprehensible in detail.

4.3.3 Sensitivity to distortions

So far everything seemed to work well. Beside a few image errors a solution of the given problem was possible for ideal data. Now we want to show the effect of different distortions as they can occur in a real experiment. We will switch on noise or alternatively polychromatic X-rays. In addition to this we check what happens if the projection values at the detection limit are not skipped in the reconstruction. Fig. 4.9 shows the results for SART and ML-TR. While SART has been superior for the ideal data this is not any longer the case here. It responds very sensitively to all kinds of distortions. In contrast to this ML-TR appears to be more robust against errors at the detection limit (option: Mono 160 keV, no skipping) and noise (option: Mono 160 keV, Noise 10%). This reflects its distinct properties, i.e. paying less weight to small projection values and using a correct noise model. For polychromatic X-rays (option: Poly 200kV 0.5 mm Cu) severe shape deformations occur in both cases.

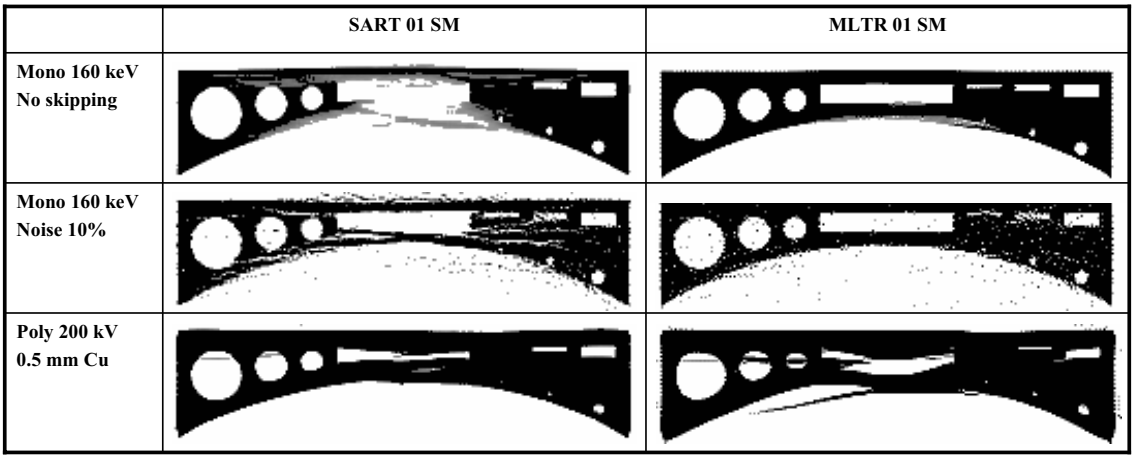

Figure 4.9: Sensitivity to distortions for limited view angle tomography with SART and ML-TR.

The situation at the detection limit can be explained as follows. In the simulation we set

the corresponding values to a constant which is a suitable model for an experiment where a saturation occurs (review section 4.1). As a consequence these values do not represent a correct X-ray absorption signal and this circumstance is a strong systematic distortion. The effect on the reconstructed object is drastic. Therefore these values have to be skipped in the reconstruction, i.e. the related projection rays are not included into the projection equation. This is principally necessary for all algorithms. For experimental data the situation can be even worse because the dynamic range does not simply end at a certain threshold. Typically there is a gradual saturation due to which non-linear distortions occur in a larger range before the total limit of detection is reached. If we consider that SART seems to be extremely sensitive to this type of distortion we can expect difficulties in the experiment which we do not expect for ML-TR.

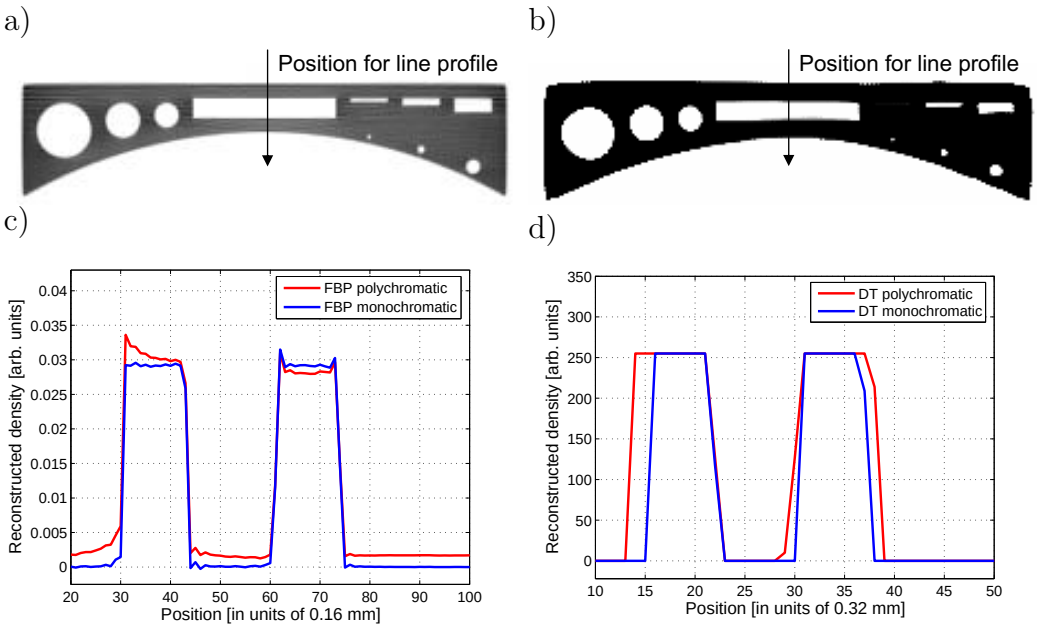

Figure 4.10: Comparing *a)* FBP and *b)* DT reconstruction for polychromatic X-rays (200 kV 1.5 mm Cu). *c)* and *d)* Corresponding vertical line profiles at the image center. They are compared to ideal monochromatic data.

In general systematic distortions are particularly critical if a single material prior is used. There are merely two possible grey values in the reconstruction and the deviations in the projection data can only be mapped to shape deformations of the object while for FBP they can be additionally mapped to a continuous grey scale. A nice illustration was given in our publication [Kri05] by comparing DT and FBP for an infinite dynamic range and polychromatic X-rays. Picking up the results, the shape was not at all affected in FBP (Fig. 4.10 a and c) while it clearly was for DT (Fig. 4.10 b and d). In this example the same voltage was used as above (200 kV) but the beam hardening filter was 1.5 mm copper instead of 0.5 mm. Therefore the spectrum was much narrower (review theory

section 2.3) and the shape deformations not as large as before. The beam hardening artifacts which are visible for FBP are similar to those discussed in chapter 3.1. Note that in this example a higher resolution has been used for FBP, which explains the different scaling on the abscissa.

Finally we give a summary of our observations by looking at the euklidean distance d^0_{eukl} (review Eqn. 4.3 for definition). The numerical values in Tab. 4.7 help us to compare all algorithms for a varying amount of distortions. Because we come from a practical field we chose FBP as a reference to indicate the amount of distortion. The dynamic range was infinite for FBP and reduced as usual for all other algorithms. Once more we see that SART is seriously affected if the values at the detection limit are not skipped or if strong noise occurs. From this point of view ML-TR seems to be more suitable for a real experiment but we should be aware that its performance is not overwhelming either. For DT we did not perform all parameter variations but overall we had the impression that it was comparable to ML-TR. Considering weak distortions a moderate noise level of 2% may be tolerable in all cases, however, polychromatic X-rays are always critical. Therefore a correction for polychromatic X-rays (beam hardening correction) will be obligatory in experiments with X-ray tubes. We may further conclude that any other kind of systematic distortion e.g. scattering has to be avoided as well. This will be the main concern in the next chapter.

	Reference FBP Infinite DR	LV reconstruction DR 350:1		
		SART 01 SM	ML-TR 01 SM	DT 01 SM
Ideal data	5.5	6.7	9.7	10.9
No skipping	5.5	26.7	11.7	-
2% Noise	15.2	7.8	10.7	11.3
5% Noise	23	9.6	11.5	12.2
10% Noise	30.3	25.4	17.8	-
Poly 200 kV 0.5 Cu	24.7	34.5	49.9	-
Poly 200 kV 1.5 Cu	18.0	25.3	39.3	32.2
Poly 200 kV 5.0 Cu	10.4	16.3	23.7	-

Table 4.7: Achieved values of d^0_{eukl} for different types of distortions and algorithms.

5 Experimental results

Motivation

In this chapter we continue with the investigation of the Bat Phantom regarding a reduced dynamic range. Our guideline was to apply the iterative reconstruction algorithms for limited view angle tomography which were analyzed in our simulations to experimental data. This was not straight forward. With respect to acquisition time and spatial resolution 3D micro-focus X-ray CT is most desirable but we will see that the data quality is not good enough. We start to give an overview of the performance of selected CT systems by using standard filtered back projection (FBP) reconstruction. We will see that the dimensions of the Bat Phantom were chosen appropriately to hit the limit of the dynamic range and we get a first clue that scattering affects particularly 3D set-ups. Due to the high relevance of 3D micro-focus CT we performed a detailed analysis of this circumstance at Siemens CT PS 9 and we show that a confinement of the beam profile is necessary to suppress scattering. In addition to this a beam hardening correction is required for which we manufactured an appropriate step wedge. We will show that a solution of the given problem is possible with a particular 2D CT set-up at the EMPA[1].

5.1 Looking for suitable CT set-ups

5.1.1 Description of considered set-ups

Table 5.1 shows a selection of available set-ups for non-destructive testing. The inspection of very large objects is only possible at high energy facilities, e.g. the 10 MeV linear accelerator at the BAM or the 1.3 MeV Co-60 source at the BAM or TUM. Massive shielding is required in such facilities and the spatial resolution is quite low (> 0.5 mm). For the integration into industrial fabrication processes compact and less expensive set-ups are required and therefore X-ray tubes are a better choice as radiation source. We will now have a closer look at the 225 kV set-up at Siemens CT PS 9 and the 450 kV set-up at the EMPA. A particular case is neutron CT. At the TUM the research reactor

[1]Eidgenössische Materialprüfungs- und Forschungsanstalt, Dübendorf, Switzerland

FRM II provides for the neutron radiation and although this is large scale facility we decided to include it here because of the distinct properties of neutrons and a peculiar detector concept.

Set-up	Radiation	Dimension of facility	Beam geometry	Detector	Typical application
Siemens CT PS 9, Munich	225 kV X-ray tube (micro-focus)	Laboratory	3D cone beam	2D planar FPI detector Scintillator: 600 µm CsI	High resolution: 1 - 50 µm Small objects: 5 - 50 mm E.g. tip of injection nozzles
EMPA, Dübendorf, Switzerland	450 kV X-ray tube (mini-focus)	Laboratory	2D fan beam	1D angular PM detector Scintillator: 6 mm CdWO4	Lower resolution: 0.1 - 0.5 mm Larger objects: 5 - 50 cm E.g. cylinder heads
TUM FRM-II ANTARES, Garching	Thermal neutrons or 300 kV X-ray tube	Large scale	3D parallel beam	2D planar Mirror camera Scintillator: LiF_2 or Gd_2O_2S	Lower resolution: 0.1 - 0.5 mm Larger objects: 5 - 50 cm Different contrast for neutrons E.g. oil in combustion engines
BAM, Berlin **(Not discussed)**	Co-60 source: 1.3 MeV X-rays or Linear accelerator: 10 MeV X-rays	Large scale	3D cone or parallel beam	2D planar FPI detector	Low resolution: > 0.5 mm Large objects: > 50 cm possible
TUM RCM, Garching **(Not discussed)**	Co-60 source: 1.3 MeV X-rays	Large scale	2D fan beam	1D angular PM detector	Low resolution: 1 mm Large objects: > 50 cm possible Special application: Inspection of barrels with nuclear waste

Table 5.1: Examples for available CT set-ups in non-destructive testing (FPI detector: Flat Panel Image detector, PM detector: photomultiplier detector).

3D micro-focus CT at Siemens CT PS 9

Fig. 5.1 shows the set-up for 3D micro-focus CT at Siemens CT PS 9. It is designed for high resolution 3D cone beam CT of small parts. The object is usually magnified by a large factor and the spatial resolution, which is limited by the focal spot size of the 225 kV micro-focus X-ray tube (typ. Ø 1-100 μm), can be very high. At the same time the tube power is relatively low (typ. < 100 W) and the acquisition time for one projection (typ. 1-10 s) is rather large. But the total time for a full 3D scan is reasonable due to the fact that a 2D planar detector is used which acquires a very high number of projection lines at once. Flat Panel Image (FPI) detectors are the state of the art. They

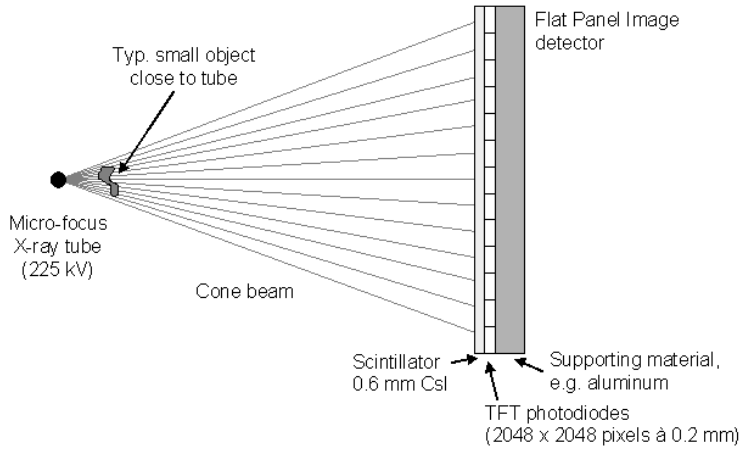

Figure 5.1: Set-up for 3D micro-focus CT at Siemens CT PS 9. It is designed for the inspection of small objects with very high spatial resolution.

have a very high spatial resolution (in our case 2048 x 2048 pixels of 0.2 mm pixel size) and good noise properties.

A fundamental problem of FPI detectors is that X-ray scattering can arise inside the detector and affect the data quality if high energies are used to investigate strong absorbing objects, e.g. the Bat Phantom at 200 kV. This particular effect is studied in more detail in [Zsc03]. For our detector, at 200 kV only about 10% of the incident X-rays are absorbed in the 0.6 mm CsI scintillator while 90% are transmitted and can be backscattered at inner layers, e.g. supporting materials like aluminum.

EMPA set-up for 2D CT

Today the only way to achieve a high data quality is to reduce scattering by beam collimation. The 450 kV 2D CT set-up at the EMPA realizes this in the most consequent way (see Fig. 5.2). The detector is composed of 125 separated detector channels which form an angular line detector, i.e. the channels are spaced equiangular on an arc. A slit collimator (tungsten) selects a fan beam and a pin hole collimator selects a narrow bunch of rays for each detector channel. In this way scattering accumulates only within one bunch of rays, i.e. from an almost 0D beam profile. Rays which are e.g. scattered at an angle at a certain object point will not be detected. In addition to this 6 mm thick $CdWO_4$ scintillator cells are used which almost completely absorb the incident X-rays such that back scattering from the detector housing is mostly suppressed. The cells are optically isolated from each other and read out with photomultipliers via optical fibres.

The main disadvantages of the EMPA set-up are long scanning times, a lower spatial resolution and photomultiplier instabilities. When it comes to scanning time it is a

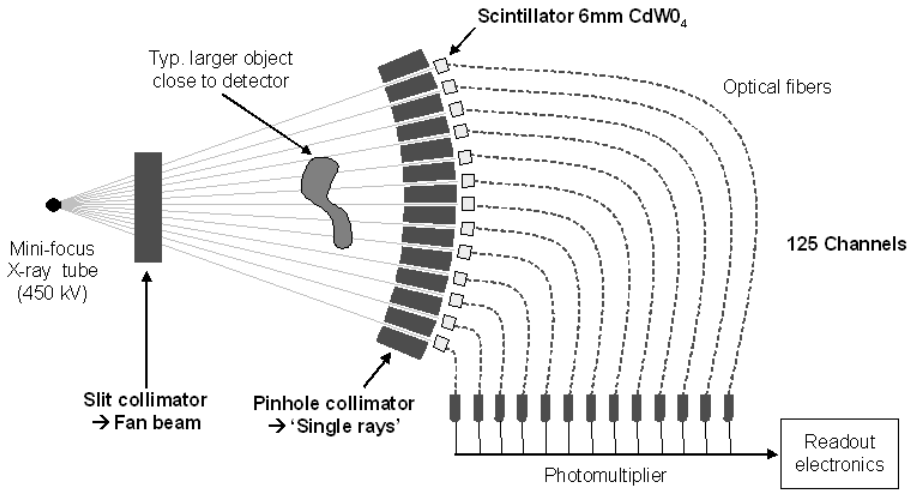

Figure 5.2: Set-up for 2D CT at EMPA. A special collimator reduces scattering very effectively and larger objects can be inspected. The spatial resolution is low and the scanning time is large.

general disadvantage of line detector set-ups that a 3D object has to be scanned slice by slice. Although a high power mini-focus tube (here 1 kW) is used and the acquisition time for one projection is quite small (here 25-100 μs) the scanning time for a 3D scan will be much larger compared to 3D micro-focus CT. As the focal spot of the mini-focus tube is large (here Ø 2.5 mm) the investigated objects are scanned without (or with small) magnification and the spatial resolution is limited by the detector pixel size (review theory section Eqn. 2.1.1). At the EMPA the pixel spacing is also large (2.1 mm) and therefore sub-positions have to be scanned. In our experiments we used 9 sub-positions and achieved 0.234 mm resolution.

A very interesting feature of the detector is that the pinhole size can be adapted adequately. It is clear that the inspection time increases significantly with increasing spatial resolution. Another specialty is that two scanning modes are available for CT. As usual a rotational mode can be used where the object is rotated by 360° and fan beam projections are recorded. The other option is a translational mode where the object is shifted parallel to the detector. In this way each detector channel records a parallel beam projection at an angle which is defined by the position of the corresponding projection ray in the fan. After one translation the object is rotated by the fan angle and the process is repeated until all parallel beam projections within 180° are collected. The advantage of the translational mode is that objects can be inspected which are larger than the

detector.

ANTARES set-up at FRM-II

Another detector concept which is worth to look at is found in neutron imaging. Fig. 5.3 shows the ANTARES set-up at the FRM-II where a mirror camera is used which is suitable for 3D CT with X-rays and neutrons at the same time. The incident radiation is converted in a scintillator to visible light which is then reflected by a mirror and recorded with a high performance optical CCD camera. This configuration is required because transmitted neutrons can damage any electronic device. For X-ray CT the benefit could be that backscattering may be avoided assuming that the scintillator would be really free hanging, the mirror would not contribute to scattering and the converted light would not be scattered either. Although this is not the case here it may be an interesting option for future improvements.

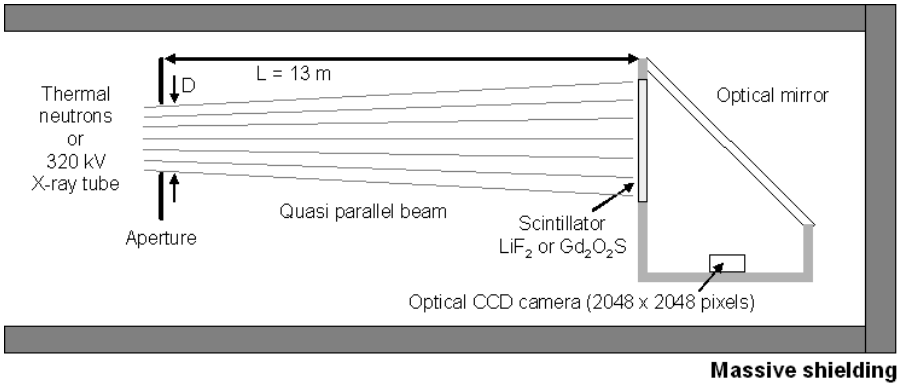

Figure 5.3: Set-up for 3D neutron and X-ray CT at ANTARES. The peculiarity is a mirror camera for detection which is commonly used in neutron physics.

The spatial resolution of the mirror camera is as high as for Flat Panel Image detectors and the noise properties of the CCD camera which can be cooled down to about -50 °C are even better. But a fundamental disadvantage is that the light is only collected from a small view angle and therefore the detection efficiency is much smaller compared to FPI detectors which collect the light from nearly a half sphere with solid angle 2π. As a consequence large integration times are required to obtain a low signal to noise ratio. In neutron imaging the spatial resolution is usually qualified by the ratio $\frac{L}{D}$, where L is the distance from the aperture in the figure to the detector and D is the diameter of the aperture. At ANTARES typical values for $\frac{L}{D}$ are 400 and 800 but also larger values like e.g. 2000 can be achieved if a particularly small aperture is used.

5.1.2 CT results for Bat Phantom with FBP

In Fig. 5.4 we show the CT results of the Bat Phantom for the set-ups which were described in the previous section. All cross-sections were reconstructed with 2D FBP, each with the appropriate beam geometry which were fan beam with linear detector, fan beam with angular detector and parallel beam geometry. For the 3D micro-focus CT set-up at Siemens CT PS 9 the central plane was considered (review theory section 2.2.3) and the result at 200 kV has been quite poor. We see that the image is strongly shaded and smeared out which indicates that massive scattering is present in 3D micro-focus CT.

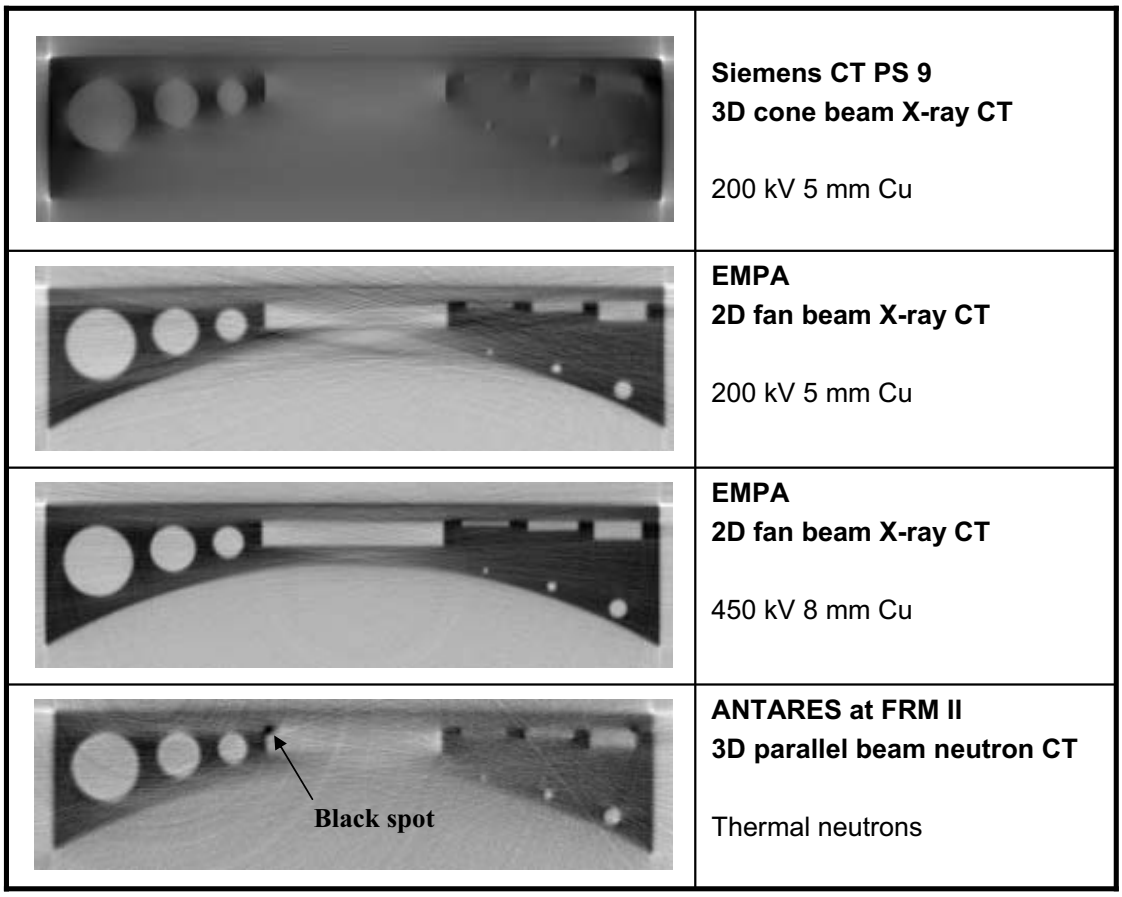

Figure 5.4: CT results of Bat Phantom for selected set-ups. The reconstruction was performed with 2D FBP.

In contrast to this the EMPA result is much clearer at the same voltage (200 kV). This confirms that scattering is effectively reduced by the special collimator at the EMPA. The data quality is very good and the limited view angle artifact in the object center

appears to be even a bit smaller compared to our simulations (review Fig. 4.8). Therefore the dynamic range must be better than in the simulation, i.e. better than 8.5 bit. At 450 kV there are almost no artifacts left and this shows the limit for the inspection of larger objects with X-ray tubes today. The beam hardening filters were chosen quite thick to exploit the penetration possibilities.

The ANTARES result for thermal neutrons is of intermediate quality. A moderate limited view angle artifact is visible and the whole image appears a bit washed out. The situation is as follows: Thermal neutrons penetrate the material quite well but scattering limits the dynamic range similar to 3D micro-focus CT. Remarkable is the black spot in the top left corner of the central rectangular gap, it is glue[2] which is invisible in X-ray CT. Metals are typically weak absorbers for neutrons while plastics are strong absorbers. This is just vice versa compared to X-rays and the black spot illustrates that neutrons can be used to obtain complementary information compared to X-rays [Sul05]. Remark: The X-ray CT configuration at ANTARES was not ready to use at the time of our measurements.

In order to simplify the comparison between the different experiments we chose reconstruction parameters which provided the same (or at least similar) reconstruction conditions (No. of projections and No. of image pixels) and spatial resolution. The selected parameters are listed in Tab. 5.2. For the micro-focus CT the spatial resolution was by far not at its limit while at the EMPA we could not achieve much more. Although the nominal pixel resolution at ANTARES was similar to the other set-ups the actual resolution is a bit worse in practice because the neutron detection process is not as localized as for X-rays.

Experiment	Radiation	Beam geometry	N_P N_x *x* N_y	SDD SOD M	ΔX_D Δx	$Ø_S$ $Ø_S$'	t_A t_{CT}
Siemens CT PS 9	X-Rays 200 kV 5 Cu 70 W	3D cone	360 310 *x* 90	923 mm 270 mm 3.42	0.40 mm 0.23 mm (binned)	0.04 mm 0.10 mm	5 s 30 min (3D CT)
EMPA	X-Rays 200 kV 5 Cu 1000 W 450 kV 8 Cu 1000 W	2D fan	360 310 *x* 90	945 mm 837 mm 1.13	0.23 mm 0.20 mm	2.50 mm 0.32 mm	50 ms 3 min (2D CT)
ANTARES at FRM II	Thermal neutrons	3D parallel (L/D 2000)	360 340 *x* 90	13 m 12.4 m 1.05	0.20 mm 0.19 mm	6.50 mm 0.32 mm	100 s 10 h (3D CT)

Np = number of projections; $Nx \times Ny$ = size of reconstructed image; SDD = source detector distance; SOD = source object distance; M = SDD/SOD = magnification; Δx_D: detector pixel size; Δx: nominal pixel resolution at object position; $Ø_S$ = focal spot diameter; $Ø'_S = (M-1) * Ø_S$ = projection of focal spot to the detector; t_A = total acquisition time for one projection including averaging; t_{CT} : scanning time for full CT (distinguish 2D and 3D CT).

Table 5.2: Scanning parameters for the selected experiments.

[2]The phantom is composed of two parts which are glued together, see appendix Fig. A.1.

5.1.3 Step wedge measurement: dynamic range and data quality

Now we want to have a closer look at the experimental conditions from above and estimate the dynamic range in each case. For this purpose we used a specially designed step wedge which was made of the same material as the Bat Phantom (copper), see Fig. 5.5 a). There is a coarse grading at the front side (0 mm to 70 mm in steps of 10 mm) and a fine grading in perpendicular direction at its backside (0, 0.5, 1, 2, 4 and 7 mm). In this way the step wedge provides a fine grading over the full range of material thickness which can be inspected with X-ray tubes. The resulting size of the step cross-sections is 20×20 mm.

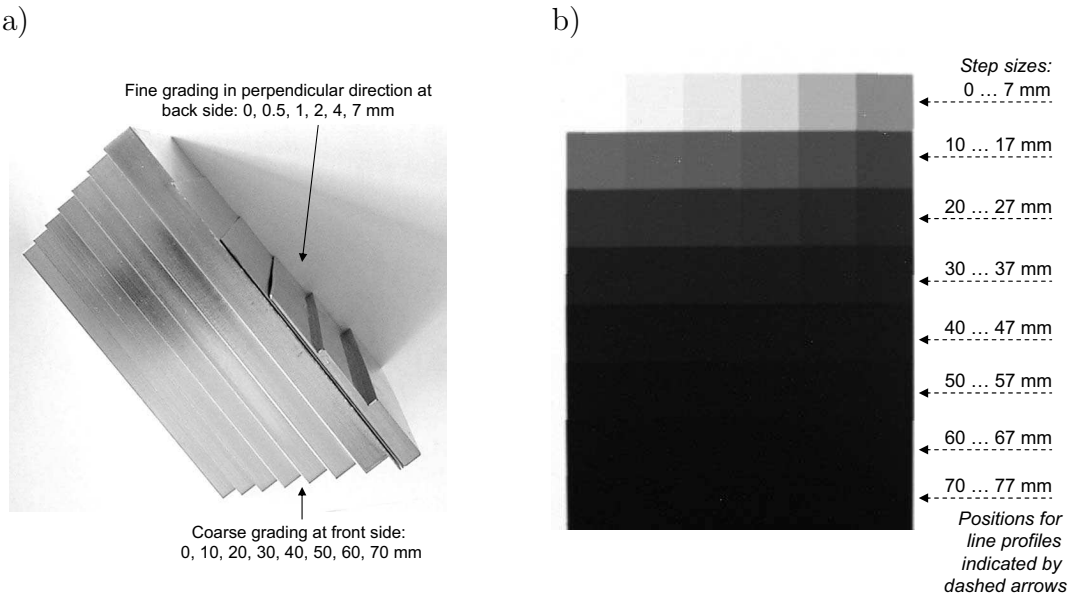

Figure 5.5: *a)* Photo of copper step wedge. *b)* Radiography of step wedge at ANTARES with thermal neutrons.

Fig. 5.5 b) shows an example of a radiography of the step wedge. We chose the result for thermal neutrons because in this case many steps can be resolved by eye. To get more detailed information we took line profiles across the fine grading as indicated by the dashed arrows. Fig. 5.6 a) shows the profiles for the 3D micro-focus CT set-up at Siemens CT PS 9 (200 kV 1.5 mm Cu) and Fig. 5.6 b) the result for the 2D CT set-up at the EMPA (200 kV 5 mm Cu). The open beam grey level was scaled to be 50000 in both cases but notice that the displayed grey level range is different. For comparison the same color code is used, e.g. the green profile corresponds to the step thicknesses from 20-27 mm in both plots.

We directly see that the dynamic range is much larger at the EMPA, i.e. the measured grey levels range down to 50 or less (bright blue curve 30-37 mm), compared to 3D micro-

a) b)

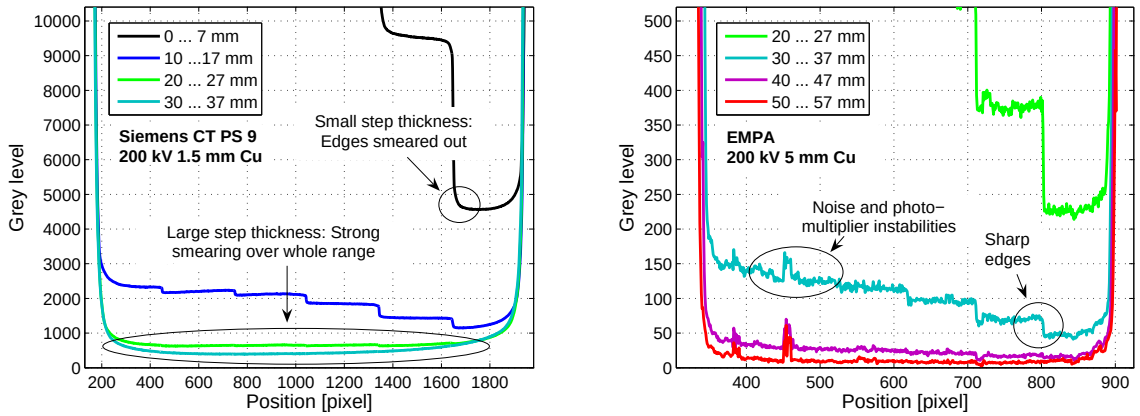

Figure 5.6: Line profiles across the fine grading of the step wedge for *a)* 3D micro-focus CT and *b)* 2D CT at EMPA.

focus CT where the minimum usable grey level is about MinGL=1000 (dark blue curve 10-17 mm). The corresponding values for the dynamic range are DR=1000:1 (10 bit) and 50:1 (5.5 bit), and the maximum material thicknesses which can be inspected is approximately d_{Max}=37 mm and 17 mm respectively. Tab. 5.3 summarizes the results for the different experiments.

Experiment	Beam	Geometry	d_{Max}	MinGL	DR
CT PS 9	200 kV 1.5 Cu	3D cone	17 mm	1000	50:1 (5.5 bit)
EMPA	200 kV 5 Cu	2D fan	37 mm	50	1000:1 (10 bit)
	450 kV 8 Cu		50 mm	250	200:1 (7.5 bit)
ANTARES	300 kV 1 Cu	3D parallel	15 mm	5500	10:1 (3.5 bit)
	Thermal neutrons		35 mm		

Table 5.3: Estimation of dynamic range from step wedge measurements (made of copper).

The explanation for the large background signal in 3D micro-focus CT is scattering. If we have a closer look at Fig. 5.6 a) we see that the profiles for the 3D micro-focus CT set-up are non-linearly distorted, i.e. the scattering background is not a constant. For small step thicknesses we observe an edge smearing (black curve 0-7 mm) which is typical for back scattering inside the Flat Panel Image detector [Zsc03]. For larger step thicknesses this effect extends over the whole step wedge (e.g. green curve 20-27 mm). In general the background will depend on the shape and type of the investigated object.

At the EMPA noise and photomultiplier fluctuations are significant close to the detection limit (Fig. 5.6 b) but scattering is very effectively suppressed by the collimation of the beam to an almost 0D beam profile. However, for 450 kV the performance was not as good as for 200 kV (Tab. 5.3). The higher the energy the more critical scattering becomes (review theory Fig. 2.2 b). At ANTARES, where 3D parallel beam geometry is used, the background was even larger compared to 3D micro-focus CT. We conclude that scattering is particulary strong in 3D CT set-ups where it can accumulate from all rays in a 2D beam profile. This will become clear in the following subsection.

5.1.4 More details about scattering in 3D micro-focus CT

The previous results indicated that scattering is quite strong in 3D micro-focus CT. Because of the high relevance of this configuration for industrial applications, we spent some effort to understand the problem in more detail. The distortions pop out clearly if we take line profiles across an edge of a lead plate. Fig. 5.7 a) shows the configuration for this measurement and Fig. 5.7 b) illustrates the position of the profile in a radiographic projection. It is important that the lead plate is large, strongly absorbing (thickness 5 mm) and machined precisely. Further it has to be aligned carefully, i.e. parallel to the detector surface and with the edge exactly at the center of the detector (central ray of cone beam).

a) b)

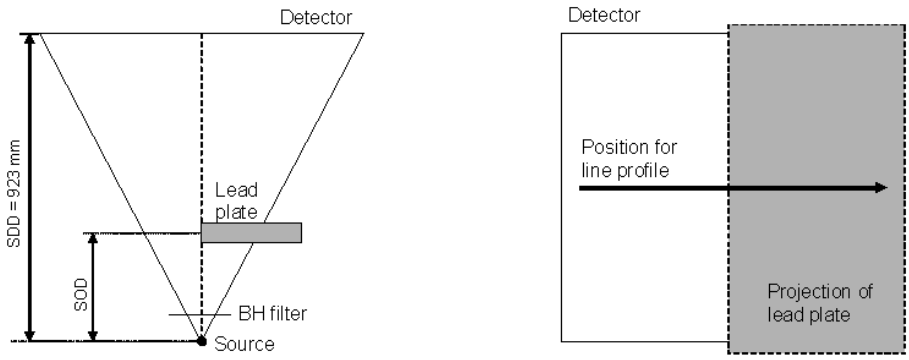

Figure 5.7: *a)* Configuration for lead edge measurement at Siemens CT PS 9. *b)* Position of line profile in radiographic projection.

The obtained function is the system response to an ideal step function and is called edge transfer function. Fig. 5.8 a) shows the result at 200 kV for different beam hardening filter thicknesses (copper filter) and a typical source object distance of SOD = 100 mm.

Due to scattering the edge is strongly smeared out over a wide range resulting in an 'S' shaped curve. This effect is massive and it is responsible for a large non-linear background signal which reduces the dynamic range of the system. We point out that this background is not a constant as the signal declines behind an object with increasing distance to its borders. It increases very much with the beam hardening filter thickness, e.g. for a 6.0 mm Cu beam hardening filter it is as high as 20% of the full signal with tails extending over 400 pixels (80 mm) on each side of the edge. If we look at the zoomed plot in Fig. 5.8 b) we see that the slope in the center is also smeared out, but only in a short range $< \pm 4$ pixel (0.8 mm) which is determined by the projection of the focal spot of the X-ray tube via the edge to the detector. This is expected and limits the spatial resolution as described in theory section 2.1.1.

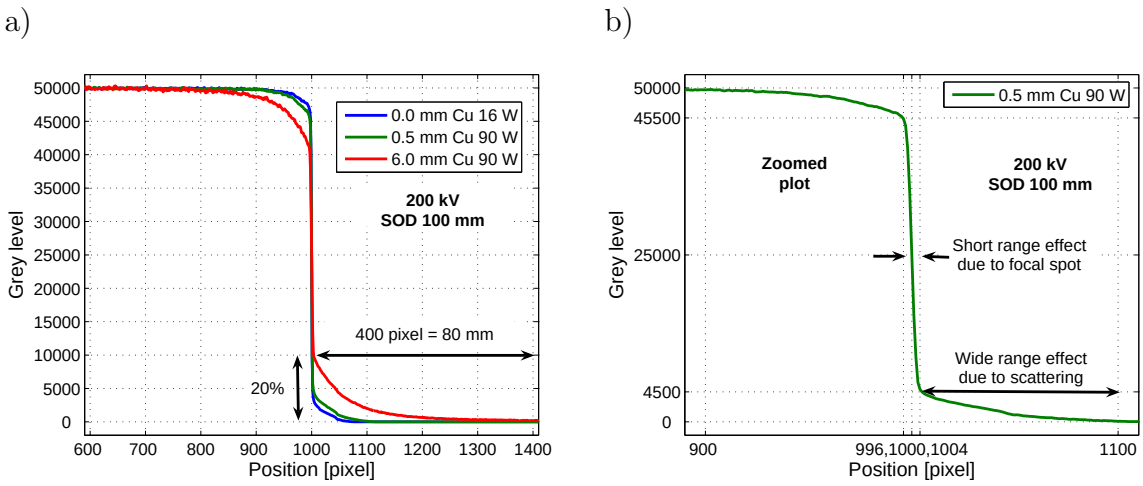

Figure 5.8: Edge transfer function measured with lead edge in the 3D micro-focus CT set-up: *a)* Full scale plot: Scattering causes a widely extended background which reduces the dynamic range. *b)* Zoomed plot: The finite extension of the focal spot affects the slope in a short range about the center which defines the spatial resolution.

In order to identify the different sources of scattering we performed a number parameter variations which we cannot show in detail here. One contribution is back scattering inside the Flat Panel Image detector [Zsc03] and as we have seen in the plot before, there must be a strong contribution of the beam hardening filter as well. The effect of the beam hardening filter is twofold:

- A thicker beam hardening filter increases the mean energy of the X-ray spectrum and therefore the probability for scattering increases in the detector and the filter.
- If a primary X-ray passes through a thicker beam hardening filter it passes through more material where it can be potentially scattered.

From this point of view we should use a low tube voltage and a thin beam hardening filter. However, for the inspection of strong absorbing metal objects like the Bat Phantom we need high energies, i.e. a high tube voltage and a thick beam hardening filter, in order to enhance the penetration possibilities (review theory section 2.1.4). Fig. 5.9 shows the 3D micro-focus CT results for the Bat Phantom at 200 kV using a 0.5 and 5 mm copper filter. Both images appear to be very similar and apparently the plus of penetration which is expected for the 5 mm filter is cancelled out by the increased background due to scattering. The actual background level for the CT experiment can be estimated by taking the minimum grey value (MinGL) of the recorded projection data (sinogram), see Tab. 5.4. This is possible because the Bat Phantom totally absorbs the X-rays in some directions. We point out that in any case the scattering background is huge (also for thin beam hardening filters) and that the system performance is very limited for the inspection of strongly absorbing objects like the Bat Phantom.

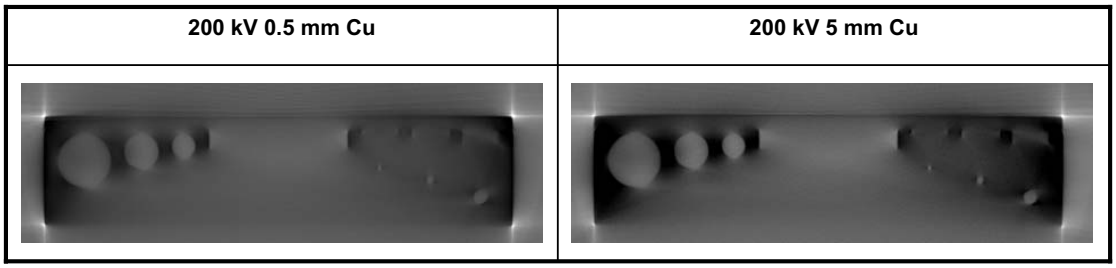

Figure 5.9: 3D micro-focus CT of Bat Phantom at 200 kV for different beam hardening filter thicknesses: The expected plus of penetration for the 5 mm filter is cancelled out by the increased background due to scattering.

Experiment	MinGL	DR
200 kV 0.5 mm Cu	1150	50:1 (5.5 bit)
200 kV 5 mm Cu	4150	10:1 (3.5 bit)

Table 5.4: Minimum grey level (MinGL) in the projection data of the CT experiment and resulting dynamic range (DR) for a direct beam of 50000.

In addition to the detector and the beam hardening filter there is a contribution from the X-ray tube as well, e.g. the emission window of the tube acts in the same way as a beam hardening filter. The different effects are illustrated in Fig. 5.10 a). The scattering of the beam hardening filter (or tube window) is projected via the edge to the detector (indicated by ray 1) in the same way like the focal spot of the X-ray tube, i.e. the illuminated spot of the filter is projected with magnification M-1 (review theory Eqn. 2.3). Therefore if we move the edge close to the tube (small SOD, large M), the

edge smearing is dominated by the scattering from the beam hardening filter (or tube window). If the edge is fixed directly to the detector (SOD=SDD, M=1), we observe only the detector effect (ray 2). The result for a measurement without beam hardening filter (0.0 mm CU) is shown in Fig. 5.10 b). It reveals the contribution of the tube window (or other tube components) and the detector. Remark: The detector contribution depends strongly on the energy and therefore would be much larger with beam hardening filter. An other effect is scattering from the investigated object, which is not relevant for the lead edge measurement, but can play a role in CT [Kas05].

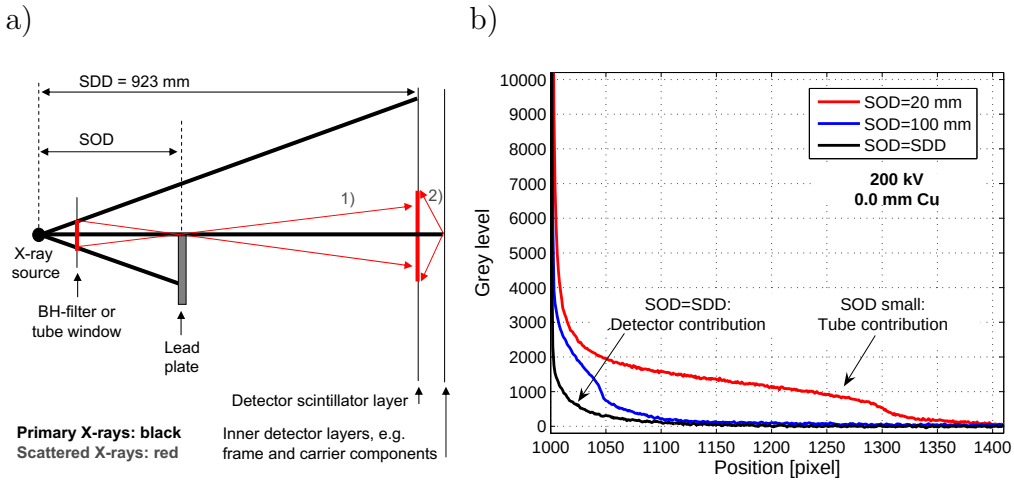

Figure 5.10: *a)* Possible sources of scattering in the lead edge experiment: beam hardening filter (or tube window) and Flat Panel Image detector. *b)* Edge transfer function (zoomed plot) for different positions of the lead edge, measured without beam hardening filter: This reveals the contribution of the detector and the tube window.

The formation of the observed 'S'-shaped curve in the lead edge experiment can be described qualitatively in the following way: In theory section 2.1.1 we mentioned that the effect of the focal spot on the image (here: edge transfer function, ETF), can be computed by a convolution of a point spread function (PSF) with the ideal image (here: ideal step function $\mathrm{ETF}_{\mathrm{Ideal}}$). We can extend this model by adding the scattering contribution, i.e. a point scatter function (PScF):

$$\mathrm{ETF} = \mathrm{ETF}_{\mathrm{Ideal}} \otimes \Big(\mathrm{PSF} + \mathrm{PScF} \Big) \,. \tag{5.1}$$

In this model the PSF and the PScF are the system response to a primary projection ray (needle ray or delta pulse). This is of course not a correct model for scattering but we might take it as a first order approximation and if we further assume basic rectangular functions for the PSF and PScF, the resulting edge transfer function in Fig. 5.11 a) rudimentarily reflects the experimental result (Fig. 5.8 b). This model further explains

the effect of beam collimation: If the dimension of the beam profile in Fig. 5.11 b) is reduced, the spatial extent of the point scatter function is reduced alike and the convolution sums up less values. If the 2D PScF has a size of N×N pixels, the reduction of the scattering background will be a factor of N per dimension. This confirms that scattering is particularly strong in 3D CT set-ups and we conclude that beam collimation is the only way to achieve a high data quality[3].

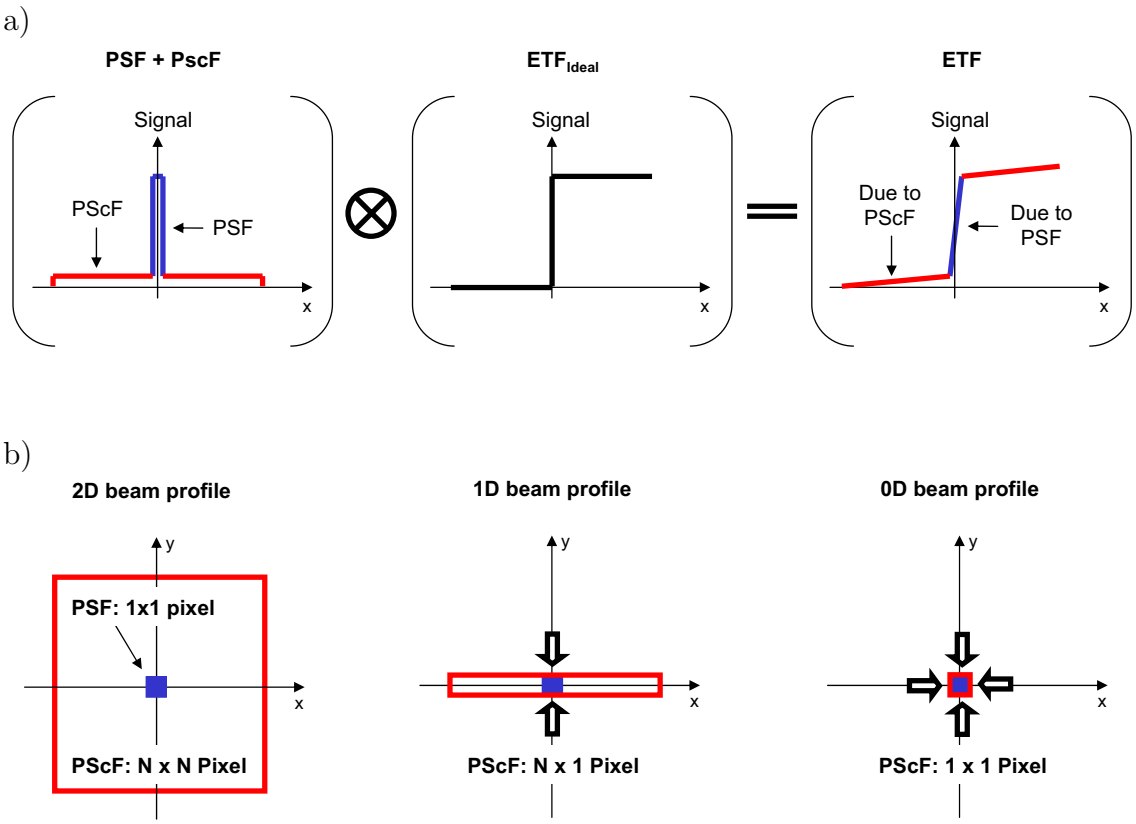

Figure 5.11: *a)* Qualitative model for the formation of the 'S'-shaped edge transferfunction (ETF): An ideal step function (ETF_{Ideal}) is convolved with a point spread function (PSF) and a point scatter function (PScF). *b)* Illustration of the effect of beam collimation: The number of values of the PScF which are summed up in the convolution is reduced by a factor of N per dimension to which the beam is confined. The scattering background will decline alike.

[3] A scattering correction which includes all effects is questionable from today's point of view. A recent work which attempts a correction for scattering of the object is [Kas05].

5.2 Attempts for limited view angle tomography in 3D micro-focus CT

In the previous section we found that scattering is the primary distortion in 3D micro-focus CT and obviously this is a serious problem if we want to apply iterative reconstruction algorithms which include prior knowledge of the object. In order to reduce scattering we have to confine the cone beam at least to a fan beam. Although in this case the special advantages of the 3D micro focus CT set-up (fast 3D scanning with isotropic magnification) are lost, our experiments are valuable to point out the essential requirements for limited view angle tomography.

5.2.1 Beam confinement: 2 pixel-slit experiment

For the following experiment we confined the cone beam in the 3D micro-focus CT set-up to a fan beam. This was achieved by means of a lead slit as shown in Fig. 5.12 a). The projection of the slit to the detector had a width of only 2 pixels (pixel size 0.2 mm), see Fig. 5.12 b). For this reason we will refer to the experiment as '2 pixel-slit experiment' or short '2PSL'. The slit itself was assembled from two precisely machined lead edges which were separated by two exact spacers. The manual alignment took some effort but after some iterations it was sufficient. Another lead collimator in front of the X-ray tube was necessary to avoid scattering from the environment.

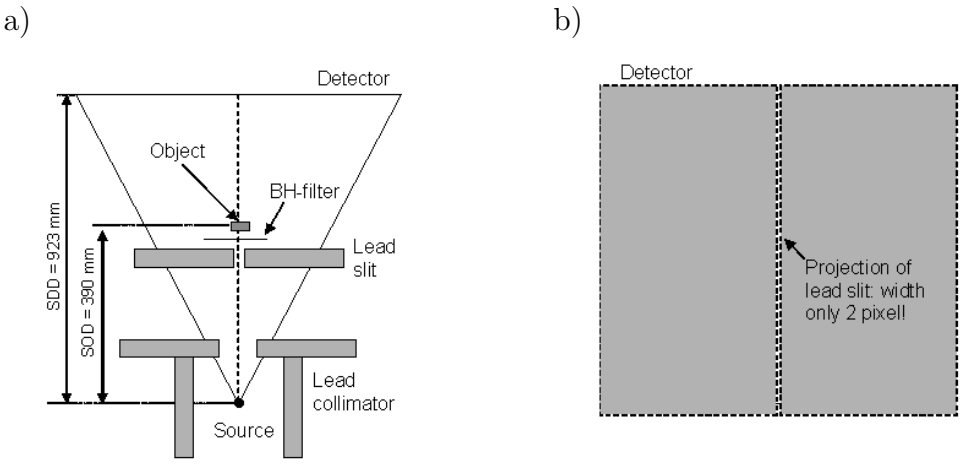

Figure 5.12: Set-up for 2 pixel-slit experiment. *a)* Arrangement of the components and *b)* projection of the slit to the detector.

With this set-up we repeated the lead edge measurement which was described in section 5.1.4. The lead edge was aligned perpendicular to the slit and the profile taken in

direction of the slit. Fig. 5.13 shows the obtained edge transfer function ('2PSL: lead edge') and compares it to the case without beam collimation ('3DCT: lead edge'). The beam parameters were identical in both cases (200 kV 0.5 mm Cu). This plot proves very impressively that scattering can be significantly reduced by beam confinement. As a result the grey levels can be very small here (zoomed plot with grey level range -50 to 550).

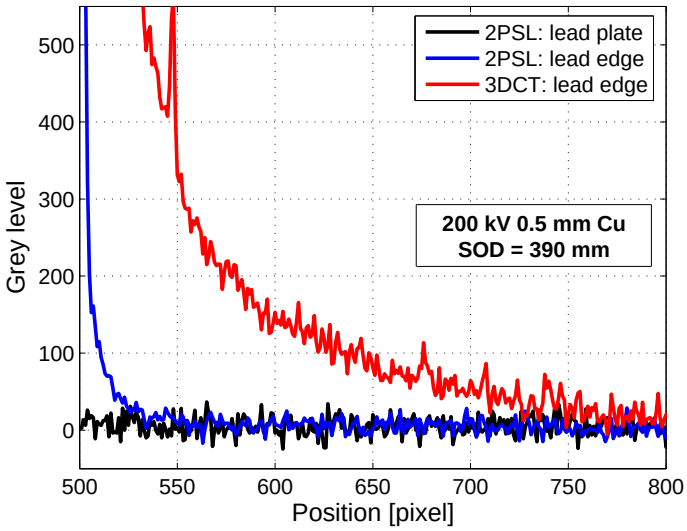

Figure 5.13: Edge transfer function for the 2 pixel-slit experiment (2PSL) compared to the 3D set-up.

We had to take special care for this measurement. Apart from scattering the Flat Panel Image detector exhibits another critical distortion. It is detector lag, i.e. the effect that the X-ray signal declines very slowly after turning the X-ray beam off. This will be described in more detail later (section 5.2.3). Here it is important to notice that we had to use a special scanning scheme to avoid lag, i.e. we turned the X-ray beam off for about 30 min before we took the dark image for the offset calibration, then we acquired the open beam image for the gain correction and then the object image. Finally the offset-/gain correction was performed without clipping of negative values and for comparison we scaled all signals according to a direct beam of 50000 grey levels.

The remaining lag and the amount of noise were determined by the same scanning scheme but covering the slit completely with the lead plate (denoted in the figure by '2PSL: lead plate'). The mean value along the slit gives a lag of 5 grey levels (after 30min) and the standard deviation a noise of 12 grey levels (acquisition time 20 s). These are excellent values. However, for a CT experiment it is not possible to achieve the same performance. The described scanning scheme requires an enormous effort, which is not feasible for each projection in a CT.

5.2.2 Application of iterative reconstruction with prior knowledge

At this point it is evident that the better we can collimate the beam the better the dynamic range and the data quality will be. For the 2 pixel-slit experiment (2PSL) we expect a significant improvement for the CT of the Bat Phantom compared to the 3D configuration. This is confirmed if we look at the FBP reconstructions in Fig. 5.14. In the figure we additionally show the attempt for a 'naive' scattering correction for 3D CT. The 'naive' correction was simply subtracting the minimum value in the sinogram (set of projection data) before the reconstruction which would be accurate for a constant background but is only a very rough approximation here. In all cases a beam hardening correction was performed (see details below).

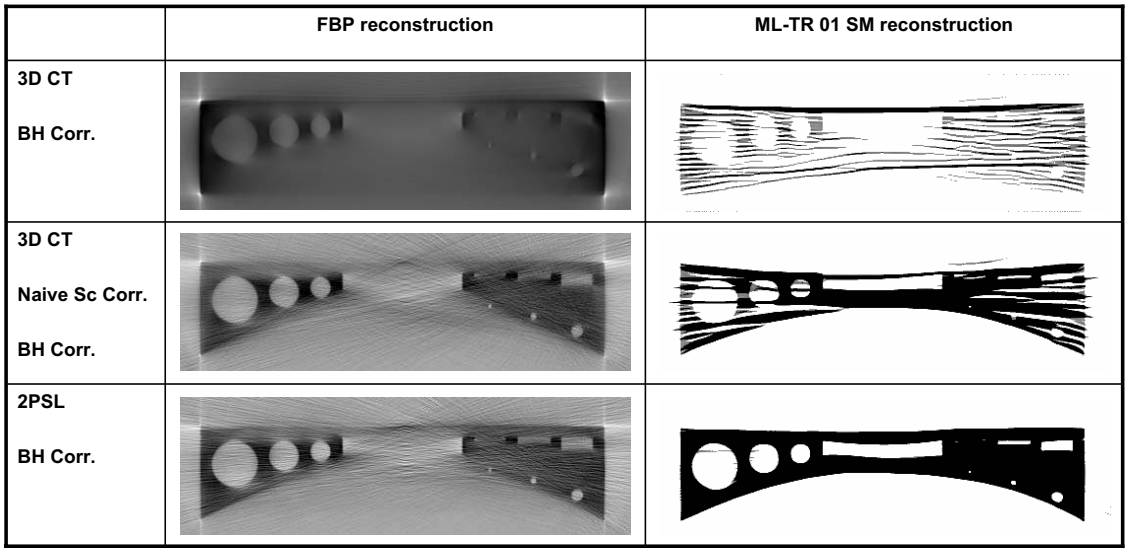

Figure 5.14: CT of Bat Phantom at 200 kV 0.5 mm Cu: FBP and ML-TR 01 SM reconstruction for 2 pixel-slit experiment (2PSL) compared to 3D CT.

The figure further shows the results for ML-TR 01 SM (01: single material prior knowledge, SM: smoothness prior). The reconstruction parameters were optimized as previously described for our simulations and we used the same settings here (review Tab. 4.5). As expected the reconstruction totally fails in 3D CT because of scattering. Further we see that the 'naive' scattering correction is not a solution to the problem. The only way to get really better is a beam confinement as it is demonstrated in the 2 pixel-slit experiment. But still the reconstructed object suffers from shape deformations and we assume that there are remaining distortions in this experiment. It is difficult to identify them here but we assume that it may be detector lag and some scattering which is left over. In addition to this the performance of the beam hardening correction is affected if lag or scattering occurs.

It should attract our attention that the FBP image for the 'naive' correction appears to be only a bit worse compared to the 2 pixel-slit experiment although the data quality is much worse as we conclude from the ML-TR 01 SM images. The effect of the 'naive' correction is that it removes a constant offset but the non-constant contribution of scattering remains. It is typical that FBP is so robust against non-linear distortions while the iterative reconstruction with single material prior information reacts very sensitively.

5.2.3 Discussion of remaining distortions

The actual scattering background in the projection data (sinogram) of the 3D CT can be obtained by subtracting the projection data of the 2 pixel-slit experiment. Necessarily the alignment of the Bat Phantom must be identical in both experiments and therefore the CT for the 2 pixel-slit experiment was performed at first, then the slit and collimator were removed without touching the sample and then the 3D CT was done. Fig. 5.15 a) shows two selected profiles of the resulting difference sinogram, one corresponds to the projections of the Bat Phantom in perpendicular position ('BP ⊥') and the other to the Bat Phantom in parallel position ('BP ∥') relative to the detector surface. Once more we see that the background strongly varies over the detector surface and that it depends on the phantom orientation and its shape. This explains why the 'naive' correction (subtraction of a constant) does not work. The overshoots at the edges correspond exactly to the long scale edge smearing which was observed with the lead edge.

a) b)

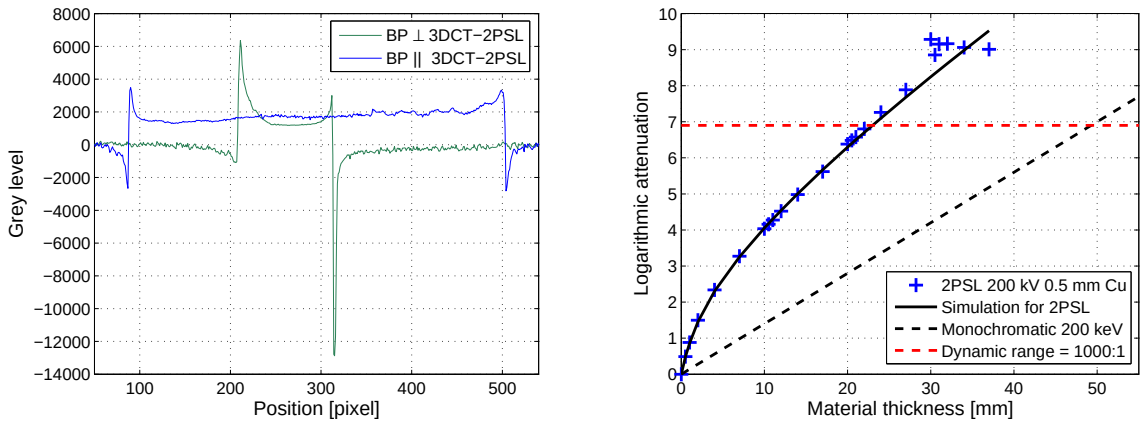

Figure 5.15: *a)* Scattering background in the projection data for 3D CT of the Bat Phantom: Two selected line profiles across the difference sinogram (set of projection data) of the 3D CT and the 2 pixel-slit (2PSL) configuration. *b)* Effect of polychromatic X-rays: Logarithmic attenuation measured with the step wedge for the 2 pixel-slit experiment compared to simulated data.

After we reduced scattering in the 2 pixel slit set-up we can measure the effect of the polychromatic X-rays by using the step wedge which was described in section 5.1.3. In Fig. 5.15 b) the measured logarithmic attenuation is plotted for the different step thicknesses and compared to simulated values. In both cases the same parameters were used, i.e. 200 kV with 0.5 mm beam hardening filter. The spectrum for the simulation was obtained from the PTB [Ank00] and may not be exactly identical to the experiment but actually the agreement of the computed and the measured attenuation values was quite good. It was therefore possible to use the simulated curve directly as a calibration curve for the beam hardening correction (review theory section 2.1.3). Only for larger step thicknesses deviations become significant and this is where the limit of the dynamic range is reached. Here the maximum useable logarithmic attenuation is about ln(1000)=6.91, i.e. the dynamic range is 1000:1 or 10 bit. By coincidence this value is the same as for the EMPA. It is important to mention that the step wedge measurement was performed with the same care to avoid lag as we did for the lead edge before (subsection 5.2.1).

a) b)

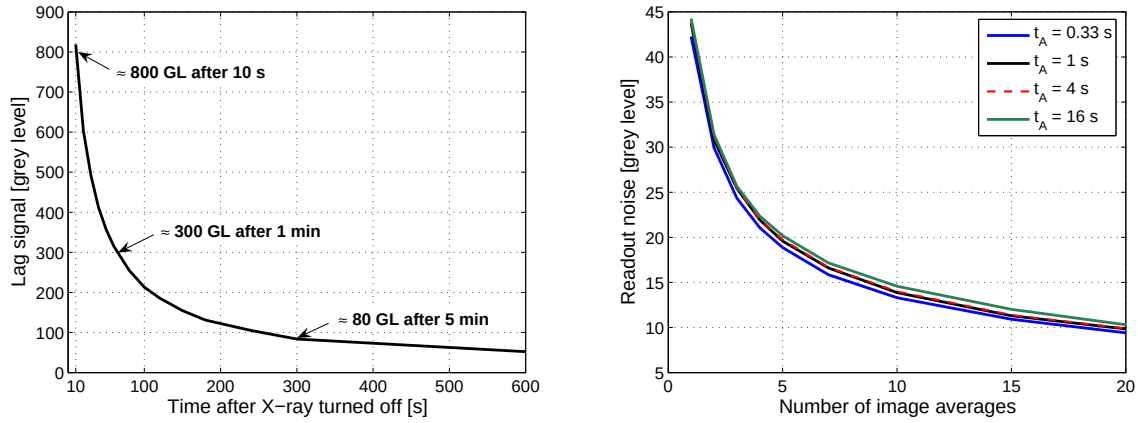

Figure 5.16: *a)* Detector lag: decay of detector signal vs. time after turning the X-ray beam off. *b)* Detector readout noise: measured in the dark image for individual pixels vs. number of averaged acquisitions for different integration times t_A.

Fig. 5.16 a) shows that detector lag is a serious problem for the considered Flat Panel Image detector in our set-up. The plot was obtained in the following way. First the detector was irradiated for 2 min with the X-ray beam on (200 kV, 0.5 mm Cu). Then the beam was turned off and the decay of the detected signal was recorded for an individual pixel (actually 4000 pixels were averaged). Finally offset values which were measured after 2h were subtracted. We see that the lag signal is still as high as 800 grey levels after 10 s. This appears very high but the effect on CT is smaller because the object is rotated quite slowly. In a 3D CT it is only hardly visible because it is usually dominated

by scattering. In the 2 pixel-slit experiment scattering is reduced and the lag is at least partly responsible for the failure of ML-TR 01 SM above.

If we consider the hypothetic case where all systematic distortions would be cured, then the ultimate limit for the dynamic range would be given by the readout noise of the detector. For a measurement a sequence of dark images was acquired and the standard deviation was calculated for an individual pixel. We additionally took the average of a certain number of acquired images before computing the standard deviation. The resulting readout noise is plotted in Fig. 5.16 b) for a variable number of averages. The measurement was performed at room temperature (20°) and the X-ray beam was turned off 24 hours before in order to avoid lag. We see that the noise properties of the detector are very good and as to be expected the noise can be drastically reduced by averaging, i.e. it declines from 45 grey levels without averaging to 10 grey levels for 20 averages. This is similar for different acquisition times which proves that the observed noise is indeed merely related to the readout process. Remark: for the lead plate measurement above (subsection 5.2.1) the noise level was a bit larger (12 grey levels for 40 averages at 0.5 s acquisition time) because in that case the standard deviation was calculated over space and therefore included calibration imperfections as well, while here we looked at the standard deviation which was calculated from a time series for an individual pixel (actually 10000 pixels were considered and the final results averaged). The dynamic range of our detector is specified in the data sheet with 80 dB, i.e. 10000:1 or 13 bit. This is equal to about 6 grey levels of noise which seems possible for very high averaging although this would be not practicable for CT experiments.

5.3 2D limited view angle tomography for EMPA data at 200 kV

In the previous section we showed that a beam confinement is crucial to avoid scattering which is a prerequisite for limited view angle tomography. We recall that the EMPA set-up realizes an almost 0D beam profile by a special tungsten collimator (review section 5.1) and therefore it was superior compared to other existing systems. At 200 kV we can assume that the collimator completely absorbs the unwanted scattering which comes from the object side and further that the scintillator cells fully absorb the incident radiation such that back scattering cannot occur. Further at 200 kV the amount of limited view angle artifacts in FBP reconstruction were comparable to our simulations and therefore this case is best suitable to demonstrate what can be achieved with limited view angle tomography today.

5.3.1 Pre-processing of the projection data

The required correction for polychromatic X-rays was performed similarly to the 2 pixel slit experiment (previous section) using the method which is described in theory section 2.1.3. The task was to fit a suitable simulated curve to the data which was measured with the step wedge and take it as a calibration curve for the correction. Fig. 5.17 a) shows the result for the measurement at 200 kV with a 5 mm copper beam hardening filter. To optimize the fit we considered a linear combination of a number of simulated curves for similar beam parameters. This is an advantage because the available spectra for the simulation do not necessarily agree with the real spectrum. Actually we found that for this fit method linear spectra can be sufficient. Such a spectrum is given by a simple linear function for the number of emitted quanta $N(E)=E_{max}-E$. With our simulation tool (review section 4.1) we then computed the attenuation in copper including an optional beam hardening filter and a $CdWO_4$ scintillator for detection. After some trial and error we obtained the best result for a linear combination of two curves, one at 200 kV with 1.5 mm copper beam hardening filter and the other with a 2.5 mm filter.

a) b)

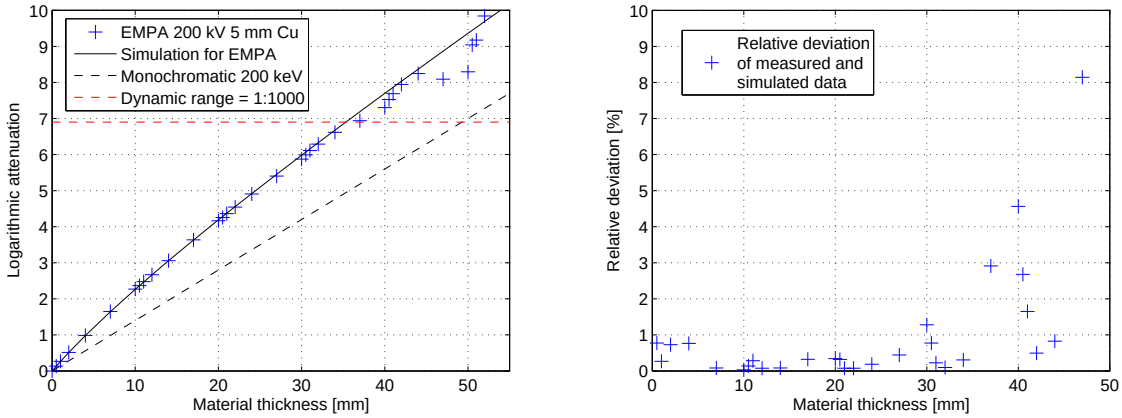

Figure 5.17: Step wedge measurement at EMPA (200kV, 5 mm Cu): *a)* Logarithmic attenuation vs. step thickness. *b)* Relative deviation of measurement and simulation.

The resulting deviations from the measured values are plotted in Fig. 5.17 b). We see that the accuracy was quite good, i.e. 1% before the detection limit was reached at about 35 mm. The corresponding dynamic range of 1000:1 (10 bit) agrees with the estimation from the line profiles across the steps (review section 5.1.3) and defines a minimum usable grey level (MinGL) of $\frac{1}{1000}$ relative to the direct beam intensity. Below MinGL the projection values in a CT experiment are not valid and we know from our simulations that they have to be skipped in the reconstruction for limited view angle tomography (review section 4.3). In addition to the detection limit itself which was considered in the

simulations we have additional effects in the experiment, e.g. a non-linear response close to the detection limit, the fact that not all pixels have the same dynamic range and that noise and especially photomultiplier fluctuation on small values correspond to a large virtual fluctuation of material thickness. In practice we included this into our estimation for the dynamic range, i.e. we estimated the value for MinGL a bit higher than we could have. Further we verified the reconstruction performance for different values of MinGL and confirmed that the originally selected value was a safe choice.

5.3.2 Reconstruction results for the Bat Phantom

Fig. 5.18 shows the reconstructions of the Bat Phantom (200 kV, 5 mm Cu) with the iterative algorithms which were optimized in our simulations (review section 4.3) and for comparison we also added the corresponding FBP result.

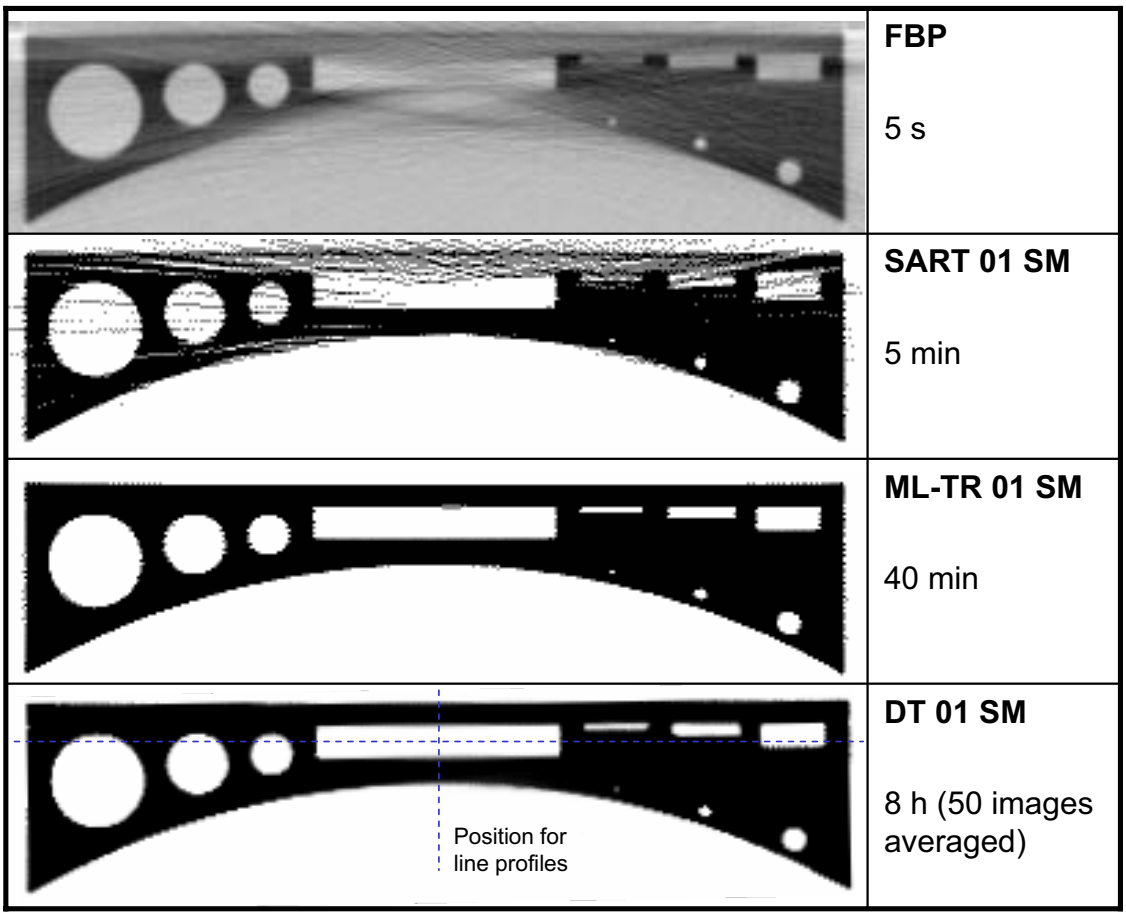

Figure 5.18: Reconstruction of Bat Phantom from EMPA data (200 kV, 5 mm Cu).

In all cases a beam hardening correction was performed and small projection values were skipped as described above. The scanning parameters were described in section 5.1.2 and the reconstruction options were set like in the simulation. We can directly compare the EMPA results to the ideal data in Fig. 4.8. If we do so we recognize that SART (with single material prior 01 and smoothness penalty term SM) failed in the experiment while it showed the best performance in the ideal case. In contrast to this ML-TR performs quite well which confirms what we have seen in simulations with distortions (review Fig. 4.9), i.e. SART seems to be most sensitive to noise and distortions on small projection values while ML-TR is more robust due to its special properties.

For DT we have a particular situation because the result significantly improved compared to the simulation. The shape deformations which were observed before did not appear here. There are three reasons for this. First aliasing is not as strong in the experiment as it was in the simulation because the projection image is smeared out by the focal spot before it is sampled. Secondly the annealing options were further optimized and a quite strong smoothness prior was used. Thirdly the reconstruction was repeated 50 times and averaged which explains the longer reconstruction time of 8 h compared to 10 min in the simulation. The averaging mostly improves the stability (recall that repeated DT reconstructions can vary because of the statistical nature of the algorithm) and a lower number would probably be sufficient as well.

a) b)

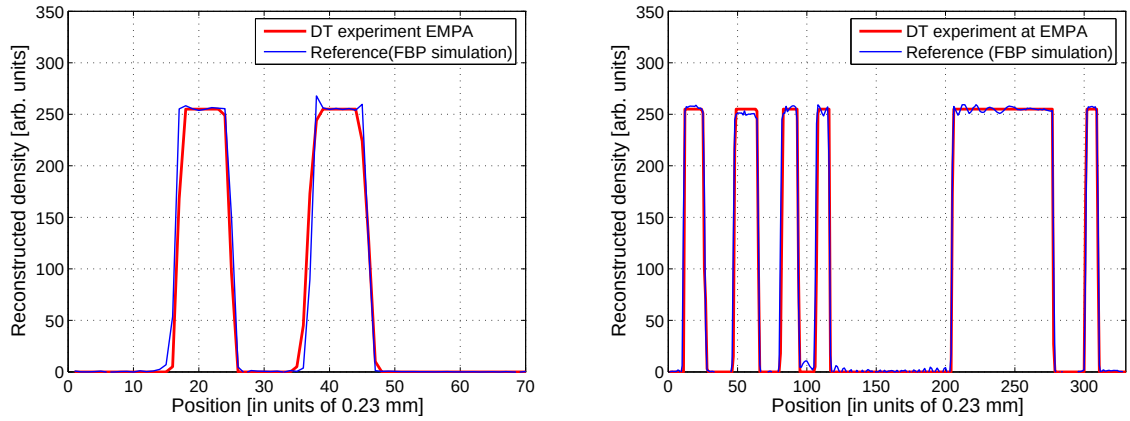

Figure 5.19: Line profiles for DT 01 SM reconstruction at EMPA: *a)* vertical and *b)* horizontal. Agreement within pixel resolution (0.23mm).

Our results prove that a realization for limited view angle tomography is principally possible. In this example (200 kV 5 mm Cu) the maximum possible material thickness for inspection was enhanced from 35 mm to 70 mm (for copper) which is an increase by 100%. However, a few errors are still present, e.g. the smallest drilling hole (Ø 0.5 mm) appears a bit two small in the DT image because of the strong smoothness prior and in

the ML-TR image there are some wrong pixels at the edges. The pixel resolution was 0.23 mm (review Tab. 5.2) and the line profiles for DT in Fig. 5.19 match the reference to a tolerance of one pixel which was similar for ML-TR (not shown). For the reference we have chosen the FBP reconstruction of simulated ideal projection data.

6 Conclusion

Aiming at non-destructive testing applications for limited view angle tomography we could deliver a prove of principle for the special case of the Bat Phantom using the particular 2D CT set-up at the EMPA (Fig. 5.18). But we point out that future developments are required for an industrial realization. At this stage the accuracy and stability of the considered algorithms were not persuading, the possible image sizes were too small and the reconstruction times too long. Although the EMPA set-up was the best we could find, it is still not good enough. A higher spatial resolution is a must for demanding inspection tasks and if we consider that SART reconstruction was excellent for ideal data but failed in the experiment we conclude that there is much more potential to enhance the data quality. When we introduced the Bat Phantom we formulated two types of inspection tasks (section 3.3). The easier one was the verification of the internal geometric structure with 100-200 μm accuracy. We expect that an application, e.g. for gas turbine blades, which fulfils these requirements and uses limited view angle tomography could be realized soon. The more advanced task of crack and void detection with a resolution of 10 to 100 μm would require 3D micro-focus CT but this is questionable in near future due to the poor data quality in such set-ups (Fig. 5.14) and due to the status quo for the reconstruction algorithms. Another aspect is that limited view angle tomography is only useful if the limit of the dynamic range is reached as it was the case for the Bat Phantom at 200 kV. If 450 kV was used at the EMPA the filtered back projection reconstruction showed almost no artifacts (review Fig. 5.1.2) and the inspection of the Bat Phantom or similar sized objects does not essentially require limited view angle tomography presuming that the dynamic range of the detector may be further increased. Nevertheless, the benefit of limited view angle tomography is obvious, i.e. to inspect objects which are larger in certain directions than the dynamic range allows or if the geometric access is restricted. In the considered example of the Bat Phantom at 200 kV the enhancement of object size was about 100%.

7 Summary

Non-destructive testing on the base of 3D micro-focus CT allows to zoom into objects with a high spatial resolution. Following the question how to inspect relatively large objects like turbine blades or other flat object with an oblong cross-section we investigated limited view angle tomography, i.e. the case that the X-ray signal is not available from some directions which are naturally required for filtered back projection (FBP) reconstruction. We had to look for new types of algorithms on the one hand and to achieve suitable experimental conditions for their application on the other hand. However, we found that a general solution for 3D micro-focus CT was not feasible at this stage and we focussed on a special problem for a prove of principle, i.e. 2D limited view angle tomography of oblong single material objects with moderate spatial resolution. For this purpose we designed the Bat Phantom which is made of copper and is representative for heavy absorbing objects like e.g. gas turbine blades. Its dimensions (70×16 mm) were selected to hit the limit of the dynamic range in typical CT systems such that the X-ray signal cannot be detected from a few view angles. If the corresponding projection values are skipped in the reconstruction this is equivalent to a partial circular scan whereas FBP requires a full circular scan for exact reconstruction.

From a theoretical point of view we distinguished two fundamental configurations for limited view angle tomography. One is the partial circular scan and the other is tomosynthesis where the rotation is completed but the projection rays are tilted. In both cases the sampling of the object is not sufficient which could be directly visualized by missing points in the Fourier space of the object. In chapter 3 we motivated our work by looking at potential applications which are of high industrial relevance: a small steel cylinder in the standard configuration for 3D micro-focus CT, a simulation model for a ball grid array using a partial circular scan or tomosynthesis, and the Bat Phantom which was described above. Using FBP reconstruction we observed characteristic rhombic shaped artifacts (limited view angle artifacts) in all cases. We pointed out that they were directly related to incomplete sampling and not caused by the specific reconstruction algorithm. This was illustrated with the discrete Fourier transform of an opaque box (masking of missing points).

A solution of the reconstruction problem requires a compensation of the missing information. For this purpose prior knowledge of the object has to be included into an iterative algorithm. For our work the most important type of prior information was the compo-

sition of a single material and additionally we considered smoothness and the exterior geometric shape of the object. We were first attracted by the simultaneous algebraic reconstruction technique (SART) which is the most developed iterative algorithm and as part of this work we implemented our own 2D version for a detailed analysis. With minor changes we could further extend it to maximum likelihood reconstruction for transmission tomography (ML-TR) which has distinct properties, i.e. using a correct noise model and paying less weight to small projection values. In both cases the single material prior knowledge was heuristically included by repeated segmentations (binary steering). More fundamental is the discrete tomography (DT) approach presented by A. Kuba from the university of Szeged, Hungary. For its evaluation we went into a cooperation which lead to a joint publication.

In chapter 4 we evaluated the principal possibilities for the reconstruction of the Bat Phantom with the help of simulated projection data. At first we looked at ideal monochromatic data with an infinite dynamic range such that limited view angles do not occur and FBP is superior in image quality and speed. We showed that SART (without prior information) can principally achieve the same image quality as FBP in a reasonable time while the convergence for ML-TR was quite poor which was related to its distinct properties. We pointed out that aliasing is critical in iterative reconstruction and that the optimization of the projection model is particularly important. In the next step we reduced the dynamic range and limited view angle artifacts appeared in FBP reconstruction. We proved representatively for SART that the single material prior information ('01') is essential for a solution and a very good performance was achieved in combination with a smoothness penalty term ('SM'). The corresponding results for ML-TR and DT were also quite good but showed a few errors. An important aspect is that the projection values at the detection limit are not correct and they had to be skipped in the reconstruction. In general systematic distortions are particularly critical due to the single material prior information. We showed that polychromatic X-rays cause severe shape deformations and we concluded that a correction (beam hardening correction) is obligatory for experimental data. Moderate noise, however, seemed to be tolerable. Overall SART was most sensitive to distortions while ML-TR and DT seemed to be more robust.

In any case the sensitivity of the algorithms to distortions is a fundamental problem for an experimental realization of limited view angle tomography and in chapter 5 we looked for suitable set-ups. First we presented the FBP results of the Bat Phantom from three very contrary experiments: 3D micro-focus X-ray CT at Siemens CT PS 9, 3D neutron CT at the TUM and 2D mini-focus X-ray CT at the EMPA. Especially the data quality in the 3D CT set-ups was strongly distorted which was confirmed with step wedge measurements. For 3D micro-focus CT we found that a strong non-constant scattering background is the major distortion (at 200 kV). With the help of a lead edge we showed that the X-ray tube, the beam hardening filter and the Flat Panel Image detector have a significant contribution. One consequence is that the positive effect of a thicker

beam hardening filter in a CT experiment (less beam hardening artifacts and larger maximum object size) is cancelled out by a higher scattering background. We should mention that this is a particular problem only for the inspection of strongly absorbing objects like the Bat Phantom. Considering limited view angle tomography we showed representatively for ML-TR that the reconstruction fails completely if the single material prior information is used. Further a 'naive' subtraction of a constant offset (minimum value in sinogram) did not improve much. With a lead slit (2 pixel slit experiment) we demonstrated that a significant reduction of scattering is only possible by confining the beam profile from 2D to at least 1D. Although, in this case, we could perform a proper beam hardening correction there were still some shape deformations in the ML-TR 01 SM (01: single material prior knowledge, SM: smoothness prior) reconstruction. Beside remaining scattering, we showed that strong detector lag is an additional problem for Flat Panel image detectors. In contrast to this the noise properties were very good. Finally a solution was only possible with the unique 2D CT set-up at the EMPA which realizes an almost 0D beam profile by collimation.

A Appendix

A.1 Dimensions of the Bat Phantom

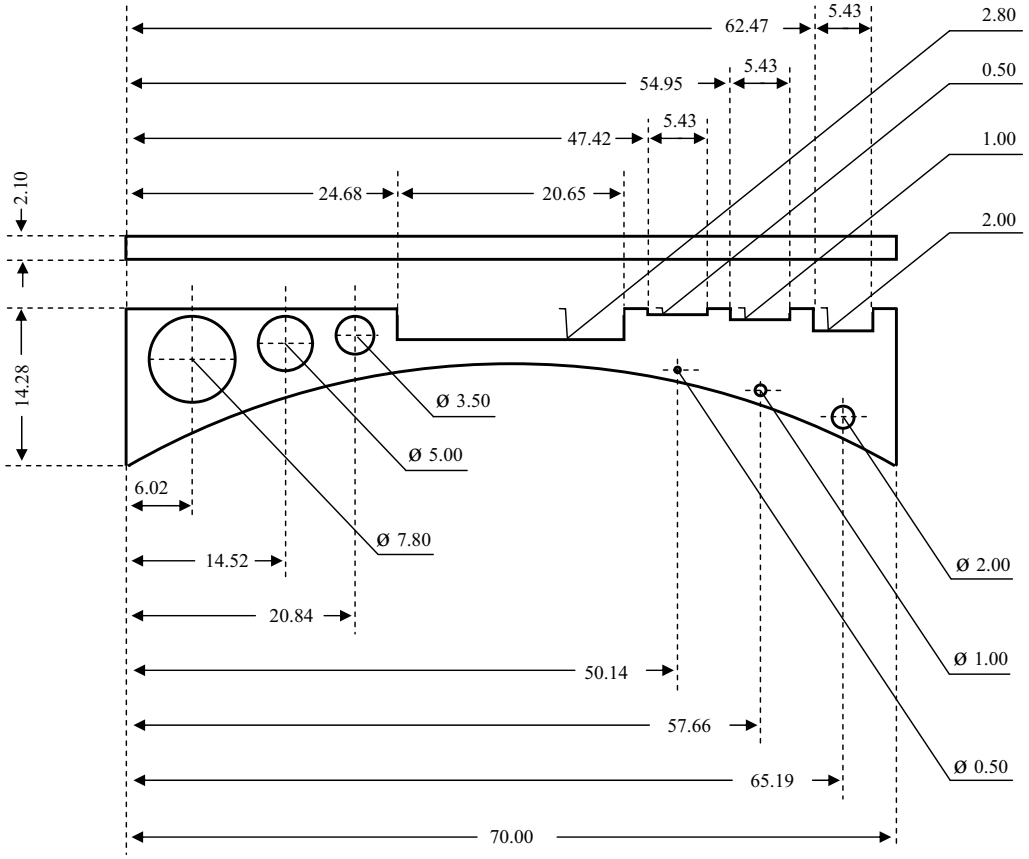

Figure A.1: Dimensions of Bat Phantom. The Phantom is composed of two parts which were glued together.

Bibliography

[AK84] Andersen, A. H., and A.C. Kak, *Simultaneous Algebraic Reconstruction Technique (SART): a superior implementation of the ART algorithm*, Ultrason. Img. Vol. 6 (1984), 81–94.

[Ank00] Ankerhold, U., *Catalogue of X-ray spectra and their characteristic data*, Physikalisch Technische Bundesanstalt, Braunschweig, 2000.

[Axe94] Axelsson, C., *Direct Fourier methods in 3D-reconstruction from cone-beam data*, Thesis, Linköping University, 1994.

[Bar95] Barlow, R. J., *Statistics: a guide to the use of statistical methods in the physical sciences*, John Wiley&Sons, West Sussex, 1995.

[BS81a] Barrett, H.H., and W. Swindell, *Radiological imaging, the theory of image formation, detection and processing*, Vol. 1, Academic Press, New York, 1981.

[BS81b] Barrett, H.H., and W. Swindell, *Radiological imaging, the theory of image formation, detection and processing*, Vol. 2, Academic Press, New York, 1981.

[Bec02] Beck, T., *3D-Rekonstruktion von Objekten mit beschränkter Geometrie mittels Algorithmen der Diskreten Tomographie*, Diploma thesis, Universität Erlangen-Nürnberg, 2002.

[Eps03] Epstein, C. L., *Mathematics of medical imaging*, Prentice Hall, Upper Saddle River, 2003.

[FDK84] Feldkamp, L., L. Davis, and J. Kress, *Practical cone-beam algorithm*, J. Opt. Soc. Am. Vol. 1 No. 6 (1984), 612–619.

[Gor70] Gordon, R., R. Bender, and G. T. Herman, *Algebraic reconstruction techniques (ART) for three-dimensional electron microscopy and X-ray photography*, J. Thoer. Biol. Vol. 29 (1970), 471–481.

[Hae99] Härer, W., G. Lauritsch, T. Mertelmaier, and K. Wiesent, *Rekonstruktive Röntgenbildgebung*, Physikalische Blätter Vol. 55 No. 3 (1999).

[Her79] Herman, G. T., *Correction for beam hardening in computed tomography*, Phys. Med. Biol. Vol. 24 No. 1 (1979), 81–106.

[HK99] Herman, G. T., and A. Kuba (Eds.), *Discrete Tomography: Foundations, Algorithms, and Applications*, Birkhäuser, Boston, 1999.

[Jaeh93] Jähne, B., *Digital image processing*, Springer Verlag, New York, 1993.

[Jaen93] Jänchen, L. U., *Schnelle Computertomographie für den industriellen Einsatz durch ein algebraisches, iteratives Rekonstruktionsverfahren*, Ph.D. thesis, Technische Universität Berlin, 1993.

[Jam95] James, J. F., *A student's guide to Fourier transforms*, Cambridge University Press, Cambridge, 1995.

[Kal00] Kalender, W. A., *Computertomographie*, Publicis MCD Verlag, Munich, 2000.

[Kas05] Kasperl, S., *Qualitätsverbesserungen durch referenzfreie Artefaktreduzierung und Oberflächennormierung in der industriellen 3D-Computertomographie*, Ph.D. thesis, Universität Erlangen-Nürnberg, 2005.

[Kat03] Katsevich, A., G. Lauritsch, H. Bruder, T. Flohr, and K. Stierstorfer, *Evaluation and empirical analysis of an exact FBP algorithm for spiral cone-beam CT*, Proc. SPIE Vol. 5032 (2003), 663–674.

[KGV83] Kirkpatrick S., C. D. Gelatt, and M. P. Vecchi, *Optimization by simulated annealing*, Science Vol. 220 (1983), 671–680.

[Kri04] Krimmel S., J. Stephan, and J. Baumann, *3D computed tomography using a microfocus X-ray source: Analysis of artifact formation in the reconstructed images using simulated as well as experimental projection data*, Nuclear Instr. and Methods in Physics Research A Vol. 542 (2005), 399–407.

[Kri05] Krimmel S., J. Baumann, Z. Kiss, A. Kuba, A. Nagy, and J. Stephan, *Discrete tomography for reconstruction from limited view angles in non-destructive testing*, ENDM Vol. 20 (2005), 455–474.

[KS87] Kak, A.C., and M. Slaney, *Principles of computerized tomographic imaging*, IEEE Press, New York, 1987.

[Kub02] Kuba A., L. Ruskó, L. Rodek, and Z. Kiss, *Preliminary studies of discrte tomography in neutron imaging*, IEEE Trans. on Nuclear Science Vol. 52 (2005), 380–385.

[Kun05] Kunze, H., K. Stierstorfer, and W. Härer, *Pre-processing of projections for iterative reconstruction*, Fully 3D Conference proceedings (2005), 84–87. To be published in IEEE TMI.

[Lew90] Lewitt, R. M., *Multidimensional digital image representations using generalized Kaiser-Bessel window functions*, J. Opt. Soc. Am. A Vol. 7 No. 10 (1990), 1834–1846.

[Man00] De Man, B., J. Nuyts, P. Dupont, G. Marchal, and P. Suetens, *Reduction of metal streak artifacts in X-ray computed tomography using a transmission maximum a posteriori algorithm*, IEEE Trans. Nucl. Sci. Vol. 47 No. 3 (2000), 977–981.

[Mor95] Morneburg, H., *Bildgebende Systeme für die medizinische Diagnostik*, Publicis MCD Verlag, Erlangen, 1995.

[Mue98] Mueller, K., *Fast and accurate three-dimensional reconstruction from cone-beam projection data using algebraic methods*, Ph.D. thesis, The Ohio State University, 1998.

[NIST99] NIST *X-ray Attenuation Database*, National Institute for Standards and Technology, 1999. With associated web site `http://www.physics.nist.gov/PhysRefData/Xcom/Text/XCOM.html`.

[Nuy97] Nuyts, J., P. Dupont, and L. Mortelmans, *Iterative reconstruction of transmission sinograms with low signal to noise ratio*, Proc. 2nd IEEE workshop CMP 1996, p. 237–248, printed by Birkhäuser, Prague, 1997.

[Pey94] Robert, N., F. Peyrin, and M. J. Yaffe, *Binary vascular reconstruction from a limited number of cone beam projections*, Med. Phys. Vol. 21 (1994), 1839–1851.

[Rad17] Radon, J.H., *Über die Bestimmung von Funktionen durch ihre Integralwerte längs gewisser Mannigfaltigkeiten.*, Berichte Sächsische Akademie der Wissenschaften, Math.-Phys. Kl. Vol. 69 (1917), 262–267.

[Sil99] Schillinger, B., *Neue Entwicklungen zu Radiographie und Tomographie mit thermischen Neutronen und zu deren routinemäßigem Einsatz*, Ph.D. thesis, Technische Universität München, 1998.

[Ste05] Steinbeiß, H. P., *Dimensionelles Messen mit Mikro-Computertomographie*, Ph.D. thesis, Technische Universiät München, 2005.

[Sue03] Schüle, T., *Medical 3D-Reconstruction with LP-based Discrete Tomography*, Diploma thesis, University of Mannheim, 2003.

[Sul05] Schulz, M., *Aufbau einer Röntgenanlage für Radiographie und Tomographie am Experiment ANTARES am FRM-II*, Diploma thesis, Technische Universität München, 2005.

[Tur01] Turbell, H., *Cone-beam reconstruction using filtered backprojection*, Ph.D. thesis, Linköping University, 2001.

[Tuy83] Tuy, H., *An inversion formula for cone-beam reconstruction*, SIAM J. Appl. Math. Vol. 43 (1983), 546–552.

[Zsc03] Zscherpel U., K. Osterloh, and U. Ewert, *Unschärfeprobleme beim Einsatz digitaler Detektoren in der Durchstrahlungsprüfung*, DGZfP Annual Meeting, 2003. With associated web site
`http://www.ndt.net/article/dgzfp03/papers/v22/v22.htm`.

Acknowledgements

Thanks to P. Böni and B. Schillinger who are my advisors at the Technische Universität München (TUM), Garching. Also I would like to thank K. Lorenz, M. Schulz, T. Bücherl and H. Erntl for their assistance with measurements at the TUM.

Special thanks to J. Baumann, P. Klofac and J. Stephan for supporting my work at Siemens, Corporate Technology PS 9, Munich; and to all other colleagues who helped when ever they could.

I want to thank very much our colleagues from Siemens Medical Solutions, Forchheim: G. Lauritsch, W. Haerer, H. Kunze for their valuable assistance in theoretical questions and K. Stierstorfer, M. Hoheisel, U. Taubenreuther for their help in experimental concerns.

Particulary I want to thank A. Kuba (University of Szeged, Hungary) for his commitment to our cooperation, A. Flisch for supporting our measurements at the EMPA (Dübendorf, Switzerland) and H. Steinbeiss (Technische Universität München, Garching) for valuable discussions in the ForμProd project.

Most of all: My friends.

Last page.